CYRIC

ANNUAL REPORT

2007

(January 2007 - December 2007)

CYCLOTRON AND RADIOISOTOPE CENTER
TOHOKU UNIVERSITY
http://www.cyric.tohoku.ac.jp/

PREFACE

In this twenty-eighth issue of the CYRIC Annual Report, we summarize the activities in research and development, and in training of radioisotope safe-treatment at the Cyclotron and Radioisotope Center (CYRIC) during the calendar year 2007.

Research at CYRIC was carried out in the fields of nuclear physics, nuclear chemistry, material sciences, nuclear medicine using PET (oncology, brain study, pharmacology), radiopharmaceutical chemistry, health physics, nuclear instrumentation, nuclear medical engineering (diagnosis and therapy technology), nuclear engineering and elemental analysis using PIXE.

Developments and improvements on nuclear instruments and techniques have progressed; one of the 2007 highlights is the success of observation of ~1mm size tumors implanted on a back of mouse with an ultra high spatial resolution semiconductor PET constructed at 2006.

Both the K=110MeV AVF cyclotron and K=12 MeV AVF cyclotron were steady operated in this year. A total of 2660 hours of beam-time of the K=110 MeV and HM12 cyclotrons were delivered for scheduled operation in research work. The high resolution beam has been realized at the 41 course to study the exotic nuclear exited states such as the alpha condensation in the nuclei, and this high quality beam was also used for the detector developments. The 32 course, where the high intensity neutron beam has been supplied for the study on the soft error of the semiconductors, was improved to be able to supply high intensity ion beam to investigate the radiation damage of the silicon detectors. In recent years, a research program on charged-particle radiotherapy has been planed at CYRIC. A horizontal beam-irradiation system has been developed for proton therapy experiments on small animals by using an 80-MeV proton. Beam tests of wobbled-beam and spot-beam scanning irradiations were successfully performed. Biological properties of the therapeutic proton beam provided from the irradiation system have been investigated based on not only the irradiation experiments on tumor cell lines but also on mice into which murine tumor cells were transplanted.

Routine productions of [^{18}F]FDG (38 preparations), [^{18}F]FRP-170 (8), [^{11}C]methionine (11), [^{11}C]doxepin (22), [^{11}C]raclopride (11), [^{11}C]donepezil (18), [^{11}C]BF-227 (30) and [^{15}O]water for clinical PET studies were carried out without any serious

trouble. A clean room for two laminar flow hot cells dedicated PET radiopharmaceutical preparation was constructed in the cyclotron hot laboratory in March. An automated miniature module for preparation of a new ^{18}F-labeled amyloid imaging agent (later, it was named [^{18}F]FACT) was developed and installed in the clean hot cell. At the same time a new Nb target system for [^{18}F]fluoride production was also introduced to the HM-12 cyclotron and they were jointly examined for reliable and reproducible preparation of [^{18}F]FACT. Several preclinical preparations were successfully completed.

"Molecular Imaging Program", supported by a JST grant for "research and education in molecular imaging", has been so fruitful and CYRIC has been always playing an important role as the site for basic and clinical experiments. Clinical studies on [^{18}F]FACT have been actively conducted. First results of translational research regarding β-amyloid imaging with [^{11}C]BF-227 was published in Journal of Nuclear Medicine and later awarded. Other routine tracers have been supplied to PET studies as before. [^{18}F]FDG study is still active, expanding the research topic to the examination of shoulder joint muscles and rehabilitation medicine. Using [^{18}F]FDG PET, CYRIC has been making an important contribution also to the multicenter study project on diagnosis of early Alzheimer's disease (SEAD-J). Clinical application of [^{11}C]doxepin and [^{11}C]donepezil to pathophysiological evaluation of various stress disorders is ongoing. [^{15}O]Water resulted in various excellent papers regarding cognition and memory.

The research program on PIXE analysis has been carried out by using electrostatic accelerator (4.5MV Dynamitron) at the Fast Neutron Laboratory, Graduate School of Engineering, Tohoku University, under the scientific tip up between CYRIC and FNL. This year, the terminal equipment, the control system and the acceleration tube of the Dynamitron accelerator were upgraded. During the period of this upgrading, micro-beam formation system has been re-developed and now it is applicable to a simultaneous measurement of in-air/in-vacuum PIXE analysis, RBS, SEM, STIM and 3D _ -CT. A total of 352 hours of beam-time was served to this program, which became shorter due to this upgrading. The life time of the new ion source and the voltage stability of the accelerator were improved by this upgrading. Research studies using Micro-PIXE analysis, STIM analysis, and Micron-CT are routinely carried out.

The training for radioisotope safe-treatment was carried out as usual. In 2007, a total of 988 staffs and students of Tohoku University took three courses: 1) Radioisotopes and radiation generators (499 trainees), 2) X-ray machines and electron microscope (395), and 3) Synchrotron Radiation (94). The number of trainees in this year increased by about ten percents compared with the previous year (907). The English classes for each course were practiced for 65 foreign students and scientists.

EDITORS:

Keizo	*ISHII*
Mamoru	*BABA*
Ren	*IWATA*
Hiromichi	*YAMZAKI*
Tsutomu	*SHINOZUKA*
Manabu	*TASHIRO*

WORD PROCESSED BY

Yu-ko YAMASHITA

We are most grateful to Tohoku University and to the Ministry of Education, Sports, Culture, Science and Technology for continuous support.

January 2008

Keizo ISHII
Director
Cyclotron and Radioisotope Center, Tohoku University

CONTENTS

2007

VIII. NUCLEAR MEDICINE

IX. RADIATION PROTECTION AND TRAINING OF SAFETY HANDLING

I. NUCLEAR PHYSICS

in a several % enrichment. In the present study, high resolution measurements have been carried out with the low-background condition. A sample of the gamma ray spectrum is illustrated in Fig. 7, showing, in deed, the resolved two peaks at E_g= 121.7825 and 123.08 keV. The yield ratio of these two components is:

y(121.7825keV)/y(123.08keV)=0.837/0.163.

The total counts of these composite peaks is 115,963 counts, yielding e.g. for the 123.08-keV g-ray, 115,963 × 0.163=18,902 counts.

Summary

By peak analysis, for the prominent peaks as listed in Table2, thermal-neutron capture cross-section ratio has been determined to be $\sigma(^{154}Eu)/\sigma(^{152}Eu)$= 55,923/721567=0.075. Further analyses of activated data for other nuclide listed in table 1 may yield more precise neutron flux, by which we are able to deduce the absolute Cross-sections $\sigma(^{154}Eu)$ and $\sigma(^{152}Eu)$, separately.

References

1) JENDLE-3.2, Japan Atomic Energy Research Institute, Nuclear Data Center.
2) L. L. Riedinger and Noah R. Johnson , Phys. Rev. **C2**, 2358 (1970).
3) W. MICHAELIS, Nucl. Phys. **A155**, 21 (1970).
4) R. A. Meyer, Phys. Rev. **170**, 1089 (1968).

Table 1. Irradiated samples in the present experiment.

Table 1. Irradiated samples in the present experiment.			
Element	Nuclide	Half-life	Amount
Sc	^{46}Sc	83.79d	1.0g
Co	^{60}Co	5.271y	1.0g
Au	^{198}Au	2.696d	0.21g
Eu	^{152}Eu	13.542y	1.0g
	^{154}Eu	8.593y	
^{151}Eu	^{152}Eu	13.542y	0.33g
^{153}Eu	^{154}Eu	8.593y	0.33g

Table 2. Results of peak analysis, for the prominent peaks.

E_γ(keV)		$^{151}Eu(n,\gamma)^{152}Eu$		$^{153}Eu(n,\gamma)^{154}Eu$	
		counts	$1/\varepsilon^{\#}$	counts	$1/\varepsilon$
~122	121.782	97,061	287,162		
	123.08			18,902	55,923
344.3		53,097	331,856		
1085.8		7,240	102,549		
total		721,567		55,923	

$^{\#}$energy dependent detection efficien

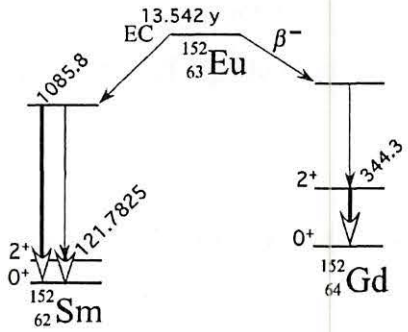

Figure 1. Decay scheme of A=152 nuclides

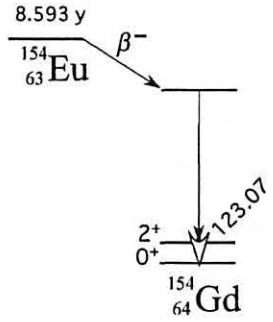

Figure 2. Decay scheme of ^{154}Eu.

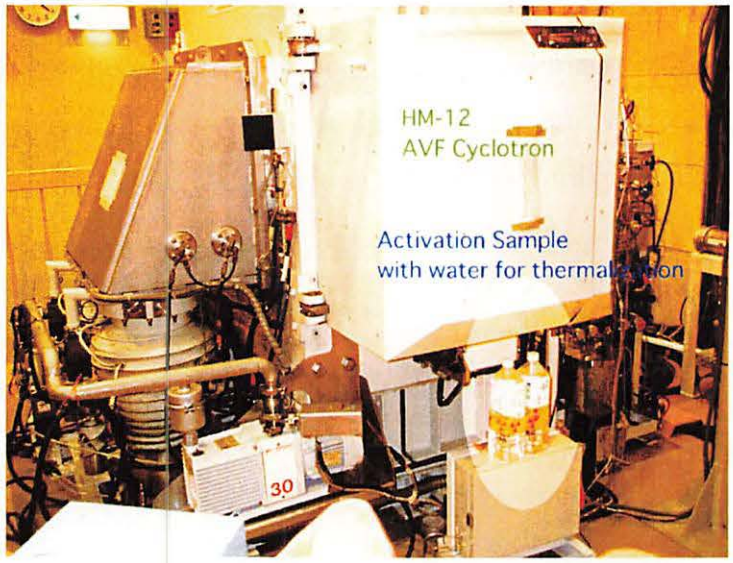

Figure 3. Irradiation by thermal neutrons from K=12 MeV -AVF cyclotron. Samples are mounted between two bottles filled with water located at the right under the RI-production target.

Figure 4. Gamma detector is mounted inside the pure iron shield-box.

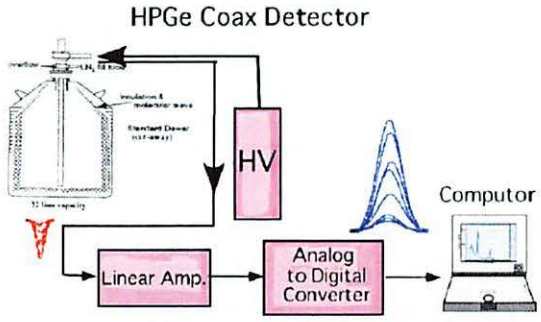

Figure 5. Electric diagram for the gamma ray analyzing system.

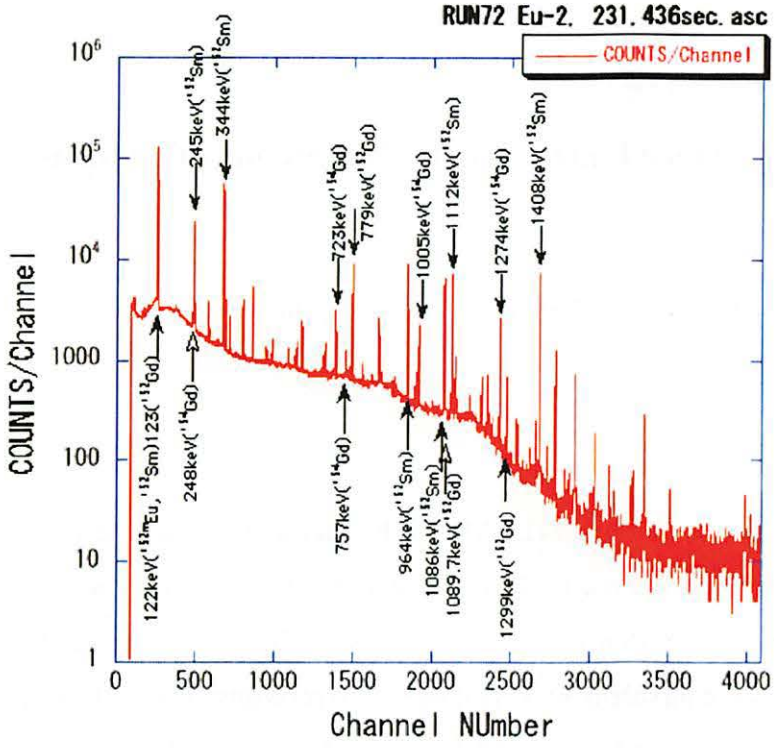

Figure 6. Typical gamma ray spectrum from the Eu sample after two weeks irradiation

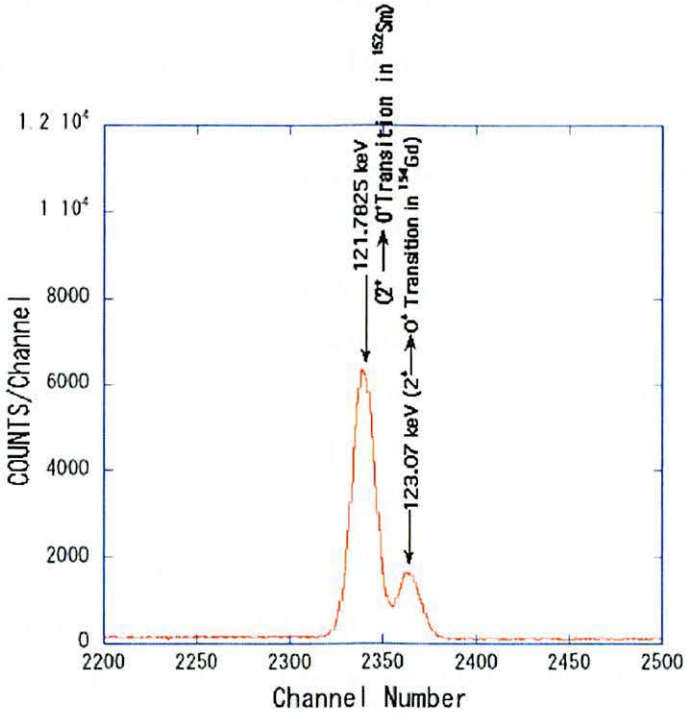

Figure 7. Typical gamma ray spectrum by high resolution measurement for the Eu sample of natural abundance.

I. 2. Development of the Surface Ionizer for the Production of Francium

Sakemi Y., Nagano T., Itoh M., Yoshida P.H., and Sugimoto N.

Cyclotron and Radioisotope Center, Tohoku University

Existence of an Electric Dipole Moment (EDM) of the elementary particle would imply that time-reversal (T) invariance and parity (P) are violated. Searches for the EDM of the electron are motivated by the existence of charge-parity (CP) violation in neutral kaon decay, which is known to be equivalent to T violation. According to the standard model, the electron EDM is far too small to be detected, but a number of models beyond the standard model predict values for the electron EDM large enough to be observed in practical experiments. In paramagnetic atoms an electron EDM results in an atomic EDM enhanced by the factor ~ $Z^3 \alpha^2$ [1]. The element which has largest enhancement factor is a heaviest alkali element francium (Fr). The Fr has no stable isotopes, and we can not make a concentrated sample due to a short life time. We proposed to take the Fr atoms from heavy-ion fusion reaction products and inject them into a laser trap apparatus, where we obtain a cold dense cloud of neutral Fr atoms. The key point to achieve the high precision search of the EDM is a production yield of Fr atoms. The goal of this project is to establish the experimental technique to produce and collect the Fr atoms, transport to the trapping chamber with high transmission efficiency, and to get more than10^7 Fr atoms/s which is the highest production rate in the world.

Fr is produced in a heavy-ion fusion reaction between an oxygen beam and a gold target ($^{18}O+^{197}Au \rightarrow {}^{210}Fr$ +5n etc.) with the primary beam energy (E_{18O}~100 MeV) just above the coulomb barrier. The target consists of a lump of gold melted and flattened onto the end of a nickel rod with a thickness of 50 μm (97 mg/cm^2). A cartridge heater is configured inside the nickel rod for heating the gold target to diffuse Fr ions produced in fusion reaction with surface lionization. The embedded Fr from fusion reaction diffuses rapidly to the surface and evaporates. The francium desorbs from the target surface as atoms and ions according to the Langmuir-Saha equation:

$$\frac{n_+}{n_0} = \frac{\omega_+}{\omega_0} \exp\left(\frac{E_{WF} - E_{IP}}{k_T}\right),$$

where n_+/n_0 is the ratio of ions to atoms desorbed, w_+/w_0 is the ratio of the statistical weights and equals 1/2 for alkali atoms, E_{WF} is the work function of the surface, and E_{IP} is the ionization potential of the desorbed atom. Since for gold E_{WF} is 5.1 eV and 4.08 eV for E_{IP}, we have $E_{WF}>E_{IP}$, and consequently the target emits primarily Fr ions. While Fr isotopes can be produces in other fusion reaction, we choose to use gold as a target since it is a noble metal, naturally monoisotopic, and provides an ionizing surface for alkali atoms.

The target is surrounded by the high temperature oven to collect all the Fr ions in the limited space. The ions, which stick to the oven wall, are released again as ions because the temperature of the oven wall is high enough to the surface ionization. The oven is heated by the 4 cartridge heaters embedded in it. The Fr ions are extracted from the extraction electrode placed in the side face of the oven. To prevent ions from escaping from oven We can achieve the small emittance Fr ion beam thanks to the small sized extraction hole with a radius 1 mm. The structure of the surface ionizer is shown in the Fig.1. The small emittance beam is quite important to transport the Fr ions with high transmission efficiency to the laser trap equipment. We have performed the 3 dimensional electric field simulation and estimated the beam emittance with ~15π mm mrad. The fabrication of the surface ionizer is almost completed as shown in the Fig.2, and the high temperature operation test is now in progress.

The experiment to check the Fr production with the fusion reaction was also done at the beam line 41 course. The gold target with the thickness 2.5 mm and the ^{18}O beam with 100 MeV are used to produce the Fr. The Fr was measured by SSD detector by detecting the decaying α particle with the energy 6.5 MeV for the ^{210}Fr isotope. The measured spectrum is shown in the Fig. 3, and the further analysis to extract the fusion reaction cross section is in progress now.

Reference

1) Sandars P.G.H., Phys. Lett. **14** (1965) 194.

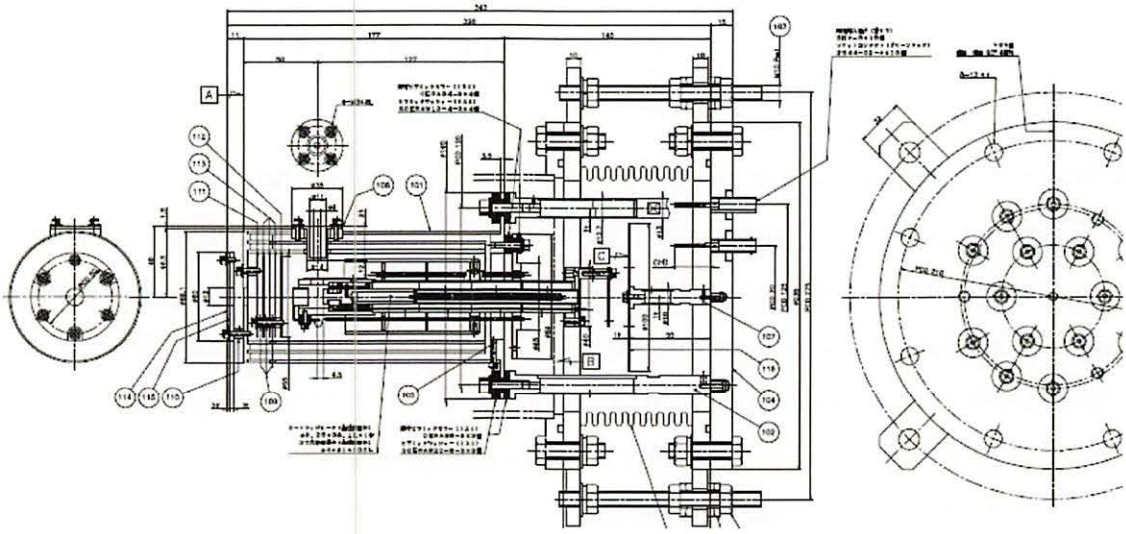

Figure 1. The structure of the surface ionizer. The target is surrounded by the high temperature oven.

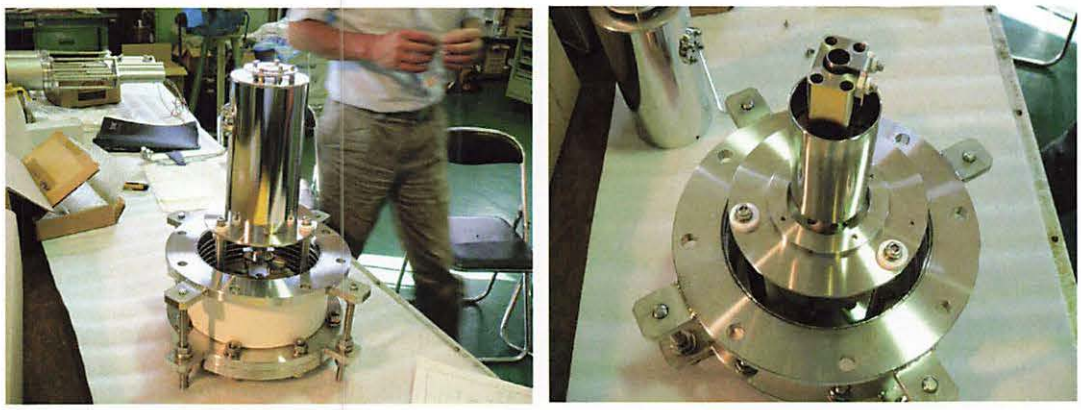

Figure 2. The fabricated surface ionizer (left picture). The right picture shows inside the ionizer. The oven which has 4 cartridge heaters can be seen clearly.

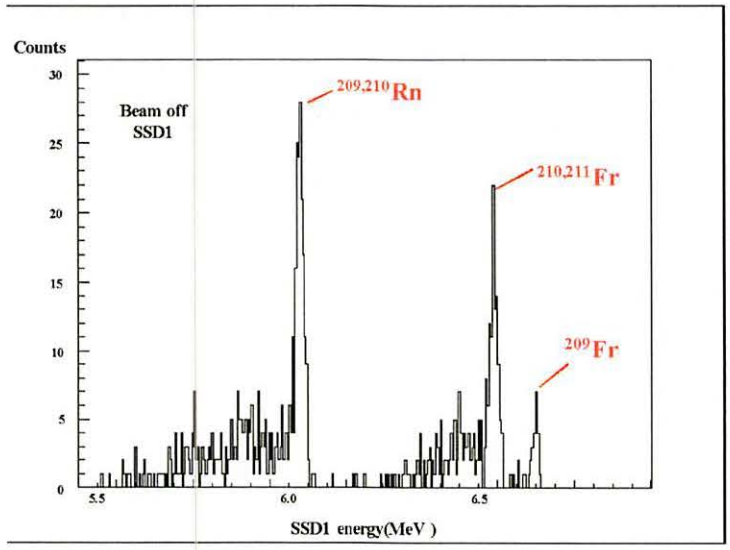

Figure 3. The α decay energy spectrum from fusion reaction with ^{18}O and ^{197}Au.

II. NUCLEAR INSTRUMENTATION

II. 1. Construction of Proton Polarizing System for New Technique to Polarize Unstable Nuclei

Tateoka M.[1], Wakui T.[2], Hoshino S.[1], Ishida T.[2], Shimada K.[2], Miyashita Y.[1], Sato N.[1], Nagano T.[1], Ouchi H.[1], and Shinozuka T.[2]

[1]*Department of Physics, Tohoku University*
[2]*Cyclotron and Radioisotope Center, Tohoku University*

We propose a new technique to polarize unstable nuclei by means of a cross polarization. The aim of this study is to find a possibility to produce a high polarization of unstable nuclei with better than 10%. The highly polarized unstable nuclei would be useful in the study of nuclear structure.

We use a crystal of aromatic molecules as a stopper material for low energy radioactive isotope (RI) beams supplied from the radio-frequency ion guide isotope separator on-line (RFIGISOL) at CYRIC[1,2]. A polarization of unstable nuclei is produced by using the following steps: optical excitation to produce a population difference in the photo-excited triplet state of pentacene molecule in the crystal[3,4], polarization transfer from electrons to protons by means of a cross-polarization[5,6], implantation of unstable nuclei in the crystal, polarization transfer from protons to implanted unstable nuclei.

As the first step of the project, we have constructed a proton polarizing system, schematically shown in Fig. 1. The system consists of a C-type magnet that produces an external magnetic field, a Nd:YAG laser for the optical excitation, a microwave system for the polarization transfer, and an NMR system that measures proton polarization.

The C-type magnet has a pole-face length of 100 mm and width of 30 mm. The gap between the poles is 51.5 mm. The magnet produces a magnetic field of 75 mT with a current of 6 A. A field non-uniformity measured with a hole probe at 60 mT is 4×10^{-2} over a crystal volume of 7 mm diameter. The non-uniformity of the external field is sufficiently smaller than the internal field of the crystal.

A crystal is mounted in a polarizing box placed in the center of the magnet. Figure 2 shows the picture of the polarizing box, inside of which a microwave resonator, an

aluminum shield for the resonator, an NMR coil, and a pair of coils for magnetic field sweep are installed. The size of the polarizing box is 179×89.5×50 mm.

A Copper-film loop-gap resonator[5] is used to produce an oscillating field for the polarization transfer. Figure 3 shows a schematic view of the LGR which is made of 25-μm thick Teflon sheet coated on both sides with 4.4-μm thick copper metal. The copper is etched to create capacitive gaps in the overlapping regions of strips. The etched sheet is formed into a cylindrical loop which acts as an inductive element. The radius of the LGR is 8 mm and the axial length is 10 mm. The LGR and a microwave circuit are inductively coupled by a coupling coil. An aluminum shield wound around the LGR is used to cut unwanted resonances which reduce Q-value of the resonator. The resonance frequency of the LGR is 2.6 GHz, which is the ESR frequency in the magnetic field of 60 mT. Figure 4 shows a measured reflection coefficient and a smith chart for the LGR.

The pair of coils is used for magnetic field sweep during the polarization transfer from electrons to protons. The coils have 68 mm diameter and their distance is 34 mm. It generates a magnetic field of 10 mT by applying a current of 30 A.

The NMR coil is wound around a support tube for the crystal. The resonance frequency of the coil is tuned to 2.6 MHz, which corresponds to the resonance frequency of protons in a magnetic field of 60 mT. The tuning of the coil to match 50 Ω is carried out by using a series capacitor of 160 pF and a parallel capacitor of 570 pF. The typical Q-value of the coil is 36.

An experiment to produce proton polarization will be carried out after an RF amplifier for the NMR measurement is installed.

References

1) Sonoda T., Fujita M., Yamazaki A., Endo T., Shinozuka T., Miyashita Y., Sato N., Goto A., Tanaka E., Suzuki T., Miyake T., Tanigaki M., and Wada M., Nucl. Instr. and Meth. **B254** (2007) 295.
2) Miyashita Y., Wakui T., Sato N., Yamazaki A., Endo T., Fujita M., Goto A., Kinoshita S., Koike T., Ma Y., Miura Y., Miyake T., Nagano T., Ohguma M., Sonoda T., Suzuki T., Tamura H., Tanaka E., Tateoka M., Yamashita W., Ukai M., Shinozuka T., Nucl. Instr. Meth., to be published.
3) S. S. Kim, and S. I. Weissman, Rev. Chem. Intermed. **3** (1979) 107.
4) D. J. Sloop, H.-L. Yu, T.-S. Lin, and S. I. Weissman, J. Chem. Phys. **75** (1981) 3746.
5) A. Henstra, T.-S. Lin, J. Schmidt, and W. Th. Wenckebach, Chem. Phys. Lett. **165** (1990) 6.
6) A. Henstra, P. Dirksen, and W. Th. Wenckebach, Phys. Lett. **A 134** (1988) 134.
7) B. T. Ghim, G. A. Rinard, R. W. Quine, S. S. Eaton, and G. R. Eaton, J. Magn. Reson. **A120** (1996) 72.

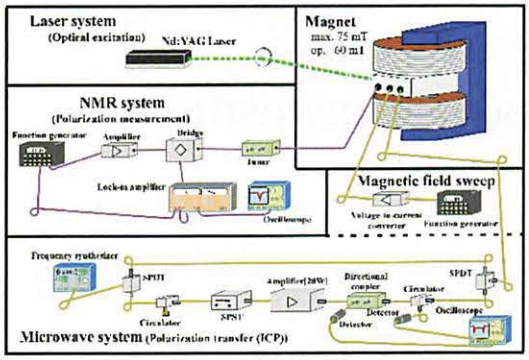

Figure 1. A schematic view of the proton polarizing system. The system consists of a magnet, a laser for optical excitation, a microwave system for polarization transfer and an NMR system of polarization measurements.

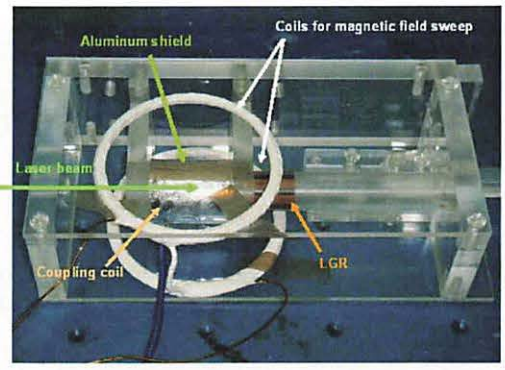

Figure 2. A picture of the proton polarizing box, which is mounted in the center of a magnet. A loop-gap resonator, a coupling coil, an aluminum shield and a pair of coils are placed inside the box.

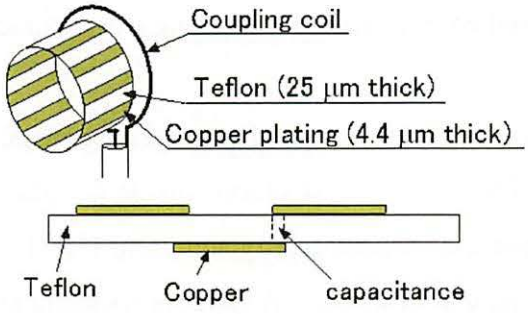

Figure 3. A schematic view of a copper-film loop-gap resonator. The resonator is used to generate oscillating magnetic field.

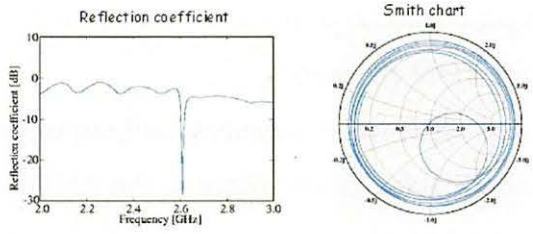

Figure 4. Measured reflection coefficient and smith chart. The resonance frequency is 2.6 GHz.

II. 2. Laser Ablation Ion Source for RFIGISOL

Hoshino S.[1], Wakui T.[2], Tateoka M.[1], Miyashita Y.[1], Shimada K.[2], Ishida T.[2], Sato N.[1], Nagano T.[1], Ouchi H.[1], and Shinozuka T.[2]

[1]*Department of Physics, Tohoku University*
[2]*Cyclotron and Radioisotope Center, Tohoku University*

The radio-frequency ion guide isotope separator on-line (RFIGISOL) has been developed for the studies of nuclear properties such as masses, lifetimes and nuclear moments of neutron rich nuclei in the medium mass region[1,2]. The RFIGISOL has a large volume gas cell and DC and RF electric fields which bring an efficient extraction of unstable nuclei of interest. In particular, it should be powerful in extracting and separating refractory elements.

For test experiments without beams from the accelerator (off-line), we have installed a laser ablation ion source in the RFIGISOL. The ion source is placed inside the gas cell instead of a Uranium target for on-line experiments, as schematically shown in Fig. 1. A metallic target of a refractory element is put at one end of a rod. A lens for focusing laser light on the target is also mounted on the rod. The lens is usually placed at the outside of the gas cell. By changing the lens position along the rod, we can focus the laser light on the target. By moving the rod along the rod axis, on the other hand, we can change the target position without changing the distance between the lens and the target. A Faraday cup (FC) is used for monitoring ion currents produced by laser ablation. The FC is mounted on the end of another rod in the gas cell. The position of the FC can also be changed by moving the rod along the rod axis.

Figure 2 shows a picture of a vacuum flange through which the rods are inserted. The flange has three glass windows for laser light, for observing a laser spot on the target, and for monitoring a FC position in the gas cell.

A Nd:YAG laser is used as a light source for the laser ablation. The laser is a pulse laser having a power of 100 mJ/pulse, 5 ns-pulse width and the repetition rate of 20 Hz. By using the laser, we can measure the time profile of the extracted ions. Figure 2 shows a

measured time profile of Mo ions which are extracted from the gas cell and accelerated to 30 kV. The measurements are carried out for different gas pressure in the gas cell. The extraction time is increased with increasing the gas pressure.

It clearly demonstrates that the ion source is useful for producing ions of refractory elements. The ion source will be used for studying the ion extraction time and efficiency, for confirming the effect of electric fields, and for optimization of the RFIGISOL system before on-line experiments.

For on-line experiments, we are planning to measure nuclear moments of the isomers by means of the time-differential perturbed angular correlation (TDPAC). A new detector system including BaF_2 has being installed and tested for the TDPAC measurements. The first on-line TDPAC measurement will be carried out in 2008.

References

1) Sonoda T., Fujita M., Yamazaki A., Endo T., Shinozuka T., Miyashita Y., Sato N., Goto A., Tanaka E., Suzuki T., Miyake T., Tanigaki M., Wada M., Nucl. Instr. and Meth. **B254** (2007) 295.
2) Miyashita Y., Wakui T., Sato N., Yamazaki A., Endo T., Fujita M., Goto A., Kinoshita S., Koike T., Ma Y., Miura Y., Miyake T., Nagano T., Ohguma M., Sonoda T., Suzuki T., Tamura H., Tanaka E., Tateoka M., Yamashita W., Ukai M., Shinozuka T., Nucl. Instr. Meth. **B266** (2008) 4498.

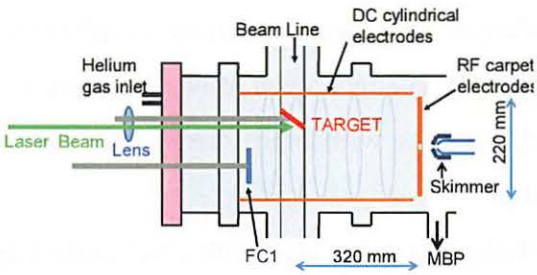

Figure 1. A schematic view of the laser ablation ion source. A metallic target of refractory element is placed on top of a rod. A lens for focusing laser light is mounted on the same rod. A faraday cup for measuring ion currents is attached on top of another rod. Both the target and the FC is movable inside the gas cell.

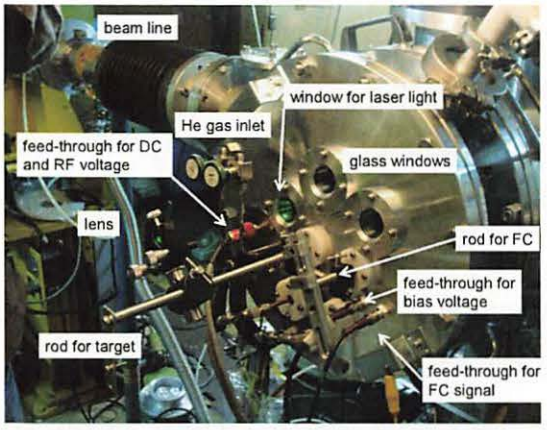

Figure 2. A picture of the flange used as a "lid" for the gas cell. The rods are inserted into the gas cell through the flange.

II. 3. Test of Radiation Hardness for GaN Diode

Narita S.[1], Yamaguchi Y.[1], Chiba Y.[1], Sakemi Y.[2], Itoh M.[2], Yoshida H.[2], and Kasagi J.[3]

[1]*Department of Electrical and Electronic Engineering, Iwate University*
[2]*Cyclotron and Radioisotope Center, Tohoku University*
[3]*LNS Tohoku University*

The wide-gap nitride semiconductor such as GaN has excellent properties in thermal, mechanical and chemical stability, and it has been recently applied to various devices (e.g. light emitting device, UV sensor, and so on)[1,2]. In addition to these superior properties, the GaN is expected to be a material for the device used in harsh radiation environments. Especially in high-energy collider experiments, the beam luminosity has been increasing, and a semiconductor detector with radiation hardness is strongly desired. Several semiconductor materials have been considered and tested for new particle detectors[3-5]. We have been developing the GaN based particle detector and successfully fabricated the GaN Schottky diode which has high quality in electrical and optical characteristics. For the GaN diode, we have performed the test of radiation tolerance, irradiating a high energy electron beam. The performance was not significantly changed even after irradiating 10^{16} /cm^2 electrons[6]. In this study, we irradiated the diodes with high energy protons and evaluated the radiation hardness of the GaN material

The Schottky barrier diode used in this study was fabricated with GaN epitaxially grown on n-type SiC substrate. The chip size of the diode was 0.5×0.5 mm^2, and the thickness of the GaN layer was ~1800 nm. The Schottky Ni/Au electrode was put onto the GaN layer and the Ti/Au Ohmic contact was deposited on the SiC. The diode structure is shown in Fig. 1. The diode chip was mounted on the TO-5 stem. The current-voltage (I-V) characteristics of the diode were measured by the ultra high resistance meter (ADVANTEST R8340). The leakage current was well suppressed (~10 nA/cm^2) and the breakdown voltage was typically above ~ 40V. In optical properties, a high responsibility for UV light was exhibited, and clear cutoff wavelength, which corresponds to the band gap of GaN, was observed in the photocurrent spectra. For evaluating the

effect of incident protons, we prepared several diodes and irradiated them with protons with various fluences, then, the I-V characteristics were measured before and after irradiation. During the irradiation, the target diodes were not applied voltage, and the output currents from the diode were not monitored.

Beam irradiation was carried out at CYRIC, using a 70 MeV proton beam. The beam current was 1.0 μA in this experiment. The degradation of the semiconductor detector, in principle, depends on the energy loss of the particles irradiated in both ionizing (forming electron-hole pair) and non-ionizing processes in the material. Especially, the non-ionizing energy loss possibly makes the atomic displacement in the crystal and it is considered to cause degradation of the device performance which includes increase of noise, lowering charge collection efficiency, and worse signal charge resolution. The non-ionizing energy loss of a 70 MeV proton is estimated to be 4 keVcm^2/g[7].

The beam profile was measured by the radioactivity of aluminum foil irradiated with the proton beam. After irradiating the foil, the activity was measured by the imaging plate. We assumed that the beam condition was stable during the irradiation, then, the profile measurement was employed just once in prior to the irradiation to the samples. The profiles along X and Y axes are shown in Fig. 2. The proton fluences on the diode were obtained considering the beam current and these profiles.

Fig. 3 shows the I-V curves before and after proton beam irradiation. For the reference, one of the typical curves for the sample before irradiation was plotted in the figure. The proton fluences of each sample were 2.7×10^{13}/cm^2 for sample #1, 2.6×10^{14} /cm^2 for sample #2, and 2.5×10^{16}/cm^2 for sample #3, respectively. We have known that the output currents of the diode can be certainly fluctuated depending on the temperature and/or humidity of the environment. Actually, these were not controlled in our measurement system. Therefore, the currents could vary in every measurement. That might be the reason why the currents measured after irradiation for sample #1 and #2 were somewhat smaller than that of the reference sample. No significant increase in the leakage current for sample #1 and #2 was found, anyway. For sample #3 with proton fluences above 10^{16}/cm^2, the increase of the leakage currents were seen, but it was not considerably large. The break down voltage did not change clearly. Thus, it was supposed that the degradation of the diode was not so serious. These results indicated that the GaN is a promising candidate for the material of future particle detectors.

The damage effects in the performance of the semiconductor devices depend on

various parameters, such as device structure, type and energy of particles irradiated, with/without applying the voltage to the device, and so on. Therefore, we should repeat the irradiation test with changing the experimental conditions and ensure the advantages of the GaN material.

References

1) Ruterana P., Albrecht M., Neugebauer J., "Nitride Semiconductors" WILEY-VCH, (2003).
2) Adachi S., "Properties of Group-IV, III-V and II-VI semiconductors" John Wiley and Sons Ltd., (2005).
3) Moll M., Nucl. Instrum. Methods A **511** (2003) 97.
4) Grant J., et al., Nucl. Instrum. Methods A **546** (2005) 213.
5) Moscatelli F., Nucl. Instrum. Methods A **583** (2007) 157.
6) Narita S., et al., Research Report of LNS **40** (2007) 31.
7) Holmes-Siedle A., Adams L., "Handbook of Radiation Effects" Oxford University Press, (2001).

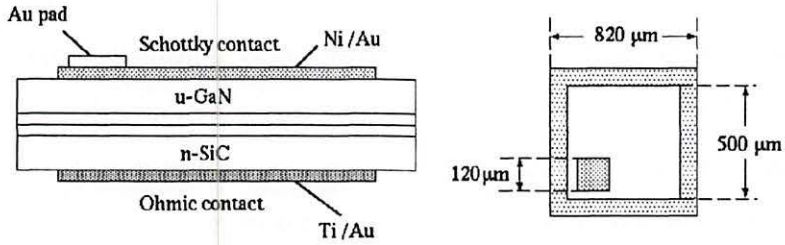

Figure 1. GaN Schottky diode.

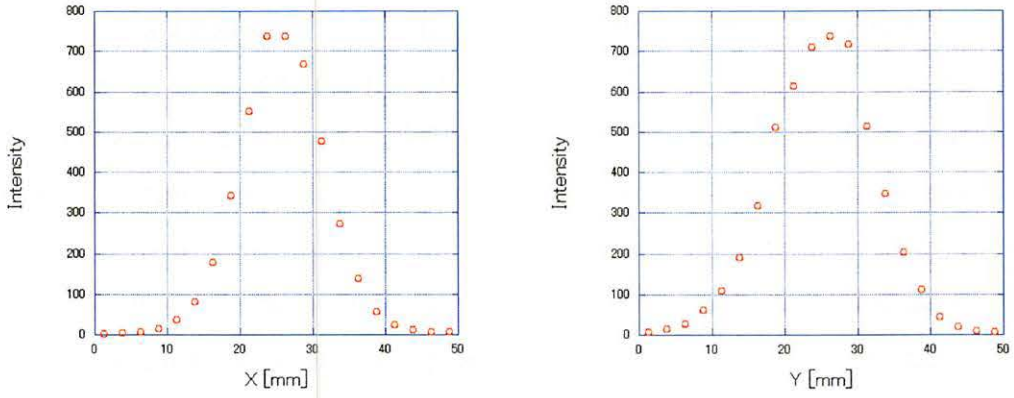

Figure 2. Beam profile. (left:X, right:Y).

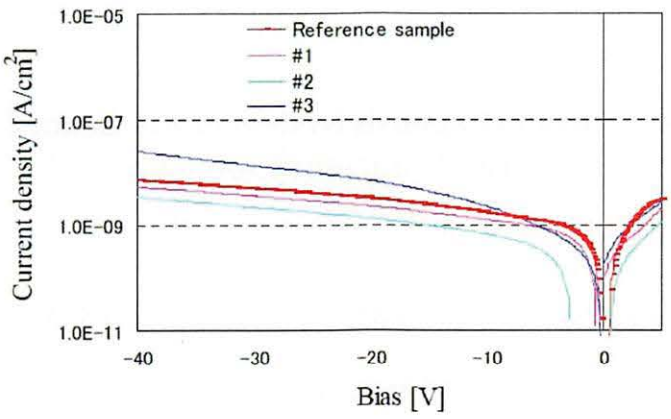

Figure 3. I-V Characteristics for the irradiated samples comparing with reference sample.

II. 4. Beam Diagnosis System of the Beam Line for the Francium Production

Sakemi Y., Nagano T., Itoh M., Yoshida P.H., and Sugimoto N.

Cyclotron and Radioisotope Center, Tohoku University

The preparation of the experiment on the search for an Electric Dipole Moment (EDM) of the francium (Fr) atom is now in progress at CIRIC. The key point of the successful experiment is to construct a high intensity Fr source (surface ionizer) with a production rate more than 10^6 particles/s to realize the high accuracy measurement. The Fr is produced by the nuclear fusion reaction of $^{18}O+^{197}Au \rightarrow {}^{210}Fr+5n$, and the beam transport of the primary beam ^{18}O with high transmission efficiency is quite important to utilize the full beam for the Fr production. Also we need to measure the beam energy spread and beam profile on the target to estimate the Fr extraction efficiency at the surface ionizer. The 34 course at the target room 3 is now upgraded for the EDM experimental project.

To fulfill the requirements mentioned above, two kinds of beam optics are designed as follows. The ion optics calculations have been done by the computer code TRANSPORT.

1. Achromatic mode: In this mode, the beam is doubly focused at the focal plane, where the target of the surface ionizer is installed. The beam size should be less than 5 mm, which is the effective hole size of the high temperature oven of which the target is located in the middle. The beam size also has to be adjusted by the small elements of the quadrupole magnets in the beam line. The ion optics is shown in the Fig. 1.

2. Dispersive mode: The beam energy spread is measured with this mode. To monitor the energy resolution of the extracted beam, this beam line is utilized as a high resolution monochrometer with a maximum dispersion of 1100 mm and the horizontal and vertical magnification of about 1 at the focal plane. The beam viewer with ZnS is placed there and the beam profile is measured with the combination of the CCD camera and frame grabber

module described below. The ion optics is shown in the Fig. 2. Not only the focal plane at the target position, but also the point in the beam line shown as ALM-J becomes the focal plane with the dispersion of about 600 mm. The ion optics can be checked with the measurement of the horizontal length of the beam profile at the ALM-J and the target position.

In these two modes, we do not have to change the polarity of all the quadrupole magnets located in the beam line. The Fr fusion reaction produces many neutrons at about 5 MeV in the target area. At these energies, neutrons pose a significant radiation hazard, and can be quite severe to the detector. In order to realize the neutron free environment, we should move the Fr from target area as an ion and transport it to the trapping room, located away behind a thick concrete wall in the next stage. The beam profiles for the achromatic and the dispersive modes are shown in the Fig. 3. The requested beam optics is achieved based on the ion optics calculation described above. The energy spread was estimated about 0.5 % from the beam profile size in the dispersive mode.

The beam profile monitor using the CCD camera and frame grabber module is prepared for the accurate beam intensity and profile measurement. The beam intensity is measured by the CCD camera with the brightness of the ZnS viewer. The output signal of the CCD camera is transferred to the frame grabber module installed into the PCI bus at the windows computer. The image data has the 512×512 pixel data with 8 bit depth showing the image intensity. These image data is analyzed in real time to extract the horizontal and vertical beam distribution. To reduce the noise in the obtained image, the background image, which means the image taken at the beam 'off' period, is subtracted from the image at the beam 'on' period with the first image processing, so that only the beam profile is extracted for the further detailed analysis. The typical image data is shown in the Fig. 4. The length of the horizontal beam profile corresponds to the beam energy spread in the dispersive transport mode. The linearity of the beam intensity to the light output measured with this detector system should be studied in more detail and now in progress with the comparison to measurement by the imaging plate.

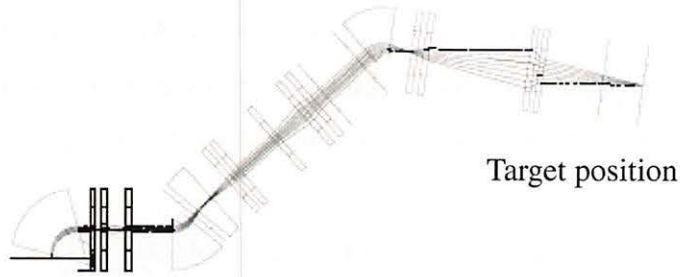

Figure 1. The achromatic mode. The beam is doubly focused at the target position.

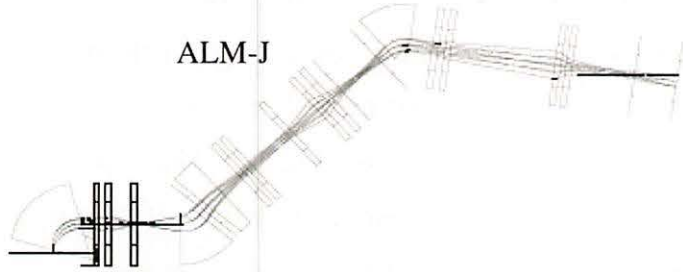

Figure 2. The dispersive mode. The beam is focused at the target position and also ALM-J.

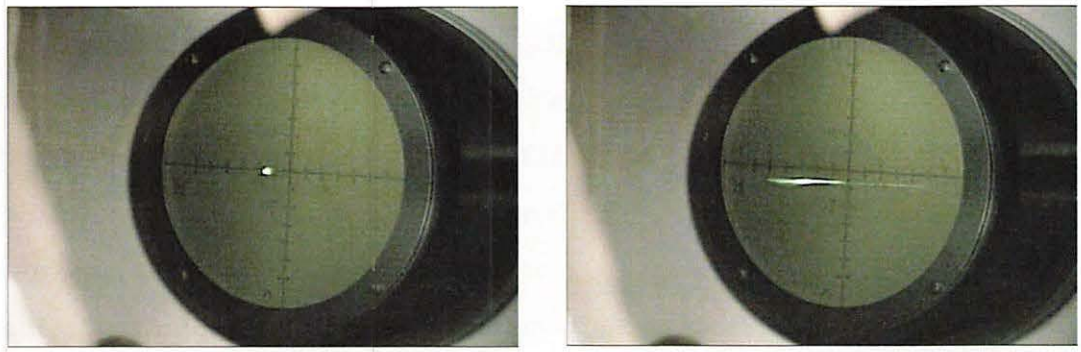

Figure 3. The beam profile at the target position. The left is for the achromatic mode, and the right dispersive.

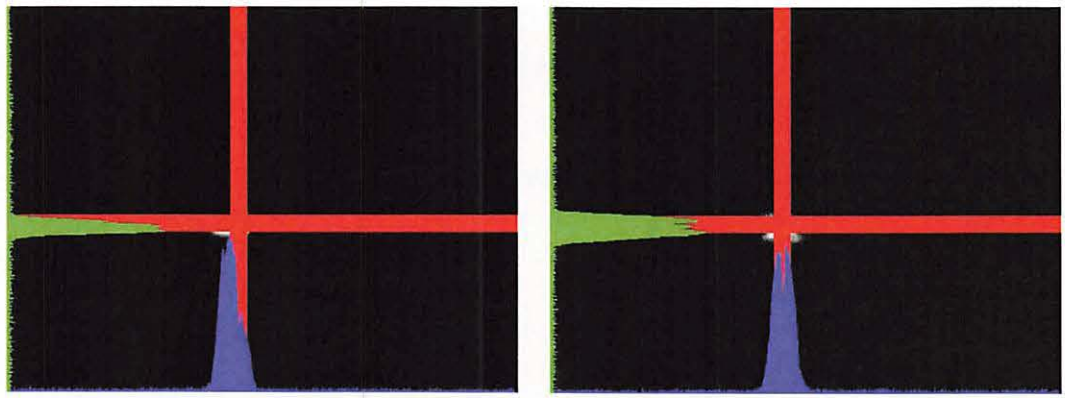

Figure 4. The horizontal and vertical projection image of the beam profile. The left plot shows the focusing beam and the right is the defocusing beam. The beam structure can be seen clearly.

III. NUCLEAR ENGINEERING

III. 1. Effect of Helium on Mechanical Properties of High Chromium ODS Ferritic/Martensitic Steels for Fusion Applications

Hasegawa A.[1], Kakinuma N.[1], Nogami S.[1], Satou M.[1], Abe K.[1], Kasada R.[2], Kimura A.[2], and Jitsukawa S.[3]

[1]Department of Quantum Science and Energy Engineering, Tohoku University
[2]Institute of Advanced Energy, Kyoto University
[3]Japan Atomic Energy Agency

Introduction

The reduced activation ferritic/martensitic (RAFM) steels are one of the candidate structural materials for fusion reactor[1]. In the fusion reactor environment, 14 MeV neutron irradiation might produce displacement damage and transmutant helium (He) atoms in structural materials. For instance, the displacement damage will be 100 dpa and He concentration will be 1000 appm in RAFM steel after 10 MW/m^2 neutron wall loading. The displacement damage might cause an irradiation hardening at temperature below 400°C and the irradiation hardening might reduce facture toughness, which includes a ductile brittle transient temperature (DBTT) shift to higher temperatures[1]. It is well known that He might stabilize a point defect cluster and cause the additional hardening at lower temperature region and the increase of swelling at higher temperature region. He atoms in material might diffuse to form He bubbles at the preexisting grain boundary during higher temperature irradiation and tend to change the fracture mode from the transgranular fracture to the intergranular fracture. The previous study[2] in our group showed the excellent resistance of the ODS (oxide dispersion strengthened) RAFM steel against He accumulation at higher temperature. Almost no change of the DBTT and non-intergranular fracture of the 9Cr (9% Chromium)-ODS steel were observed after He implantation up to 1000 appm at 550°C using the Cyclotron accelerator of CYRIC.

Higher Cr content in the ODS steel than 9% is considered to be effective to suppress corrosion in fusion reactor coolant[3]. The objective of this study is to investigate the effect of He at high temperature on mechanical properties of the high-Cr ODS steel using high energy α-particle irradiation by the Cyclotron accelerator.

Experimental

The material used in this study was the 14Cr-ODS ferritic/martensitic steel, which was fabricated by a mechanical alloying (MA) process. The chemical composition of this material is shown in Table 1. This material includes high density ultra fine oxides, which were produced from original Y_2O_3 powders during the MA process and the following heat treatment (1050°C × 1 h for tempering). Miniaturized Charpy V notch (CVN) specimen for the Charpy impact test was machined with the dimension of 1.5 mm×1.5 mm×20 mm and the notch geometry of 0.3 mm in notch depth, 0.08 mm in notch root radius and 30° in notch angle. Figure 1 shows the CVN specimen shape and geometry.

He-ion implantation was performed using 50 MeV α-particles from the AVF cyclotron of CYRIC of Tohoku University. The projected range of 50 MeV He-ions in a Fe-9Cr steel was calculated to be about 400 μm by TRIM code[4]. The tandem type energy degrader system consisting of 2 rotating wheels was used to obtain the uniform depth distribution of He atoms in specimens[5]. The calculated depth distribution of He concentration and displacement damage is shown in Fig. 2. The nominal He concentration was about 1000 appm. The displacement damage was about 0.37 dpa at the specimen surface and 0.28dpa in average. The implantation temperature was 550°C +/–10°C, which was measured using thermocouples during the implantation test.

The Charpy impact property evaluation and the fracture surface analysis after the impact test were carried out after He implantation. The Charpy impact test was carried out using an instrumented Charpy impact testing equipment at the Hot Laboratory of International Research Center for Nuclear Materials Science of Tohoku University. The test temperature ranged from –146°C to room temperature. The fracture surface of the CVN specimens after the impact test was observed using a scanning electron microscope (SEM) at the same laboratory.

Results and discussion

The Charpy impact data of the 14Cr-ODS steel is shown in Fig. 3. Almost no increment of the DBTT after He implantation at 550°C was observed. The DBTT of the 14Cr-ODS steel before/after He implantation was about –110°C, which was about 60°C lower than that of the 9Cr-ODS steel before/after He implantation. Almost no change of the upper shelf of the absorbed energy after He implantation was also observed. The upper shelf of the absorbed energy of the 14Cr-ODS steel was about 0.7 J before/after He

implantation, which was about 0.2 J higher than that of the 9Cr-ODS steel before/after He implantation. The typical fracture surfaces for the He-implanted Charpy impact specimen of the 14Cr-ODS steel tested at −146°C is shown in Fig. 4. Fracture mode for the He-implanted region was the same as the He-unimplanted region, which was cleavage fracture.

The Charpy impact properties (DBTT, upper shelf of the absorbed energy) of the 14Cr-ODS steel were relatively good in comparison with that of the 9Cr-ODS steel. Since the 14Cr-ODS steel also showed higher resistance against the corrosion than the 9Cr-ODS steel as mentioned above, the 14Cr-ODS steel might be more adequate as the structural material for fusion reactor based on these experimental results.

Acknowledgement

The authors are grateful to the staffs of CYRIC of Tohoku University relating to the accelerator operation and the irradiation experiments. This work was partly supported by the JUPITER-II (Japan-USA Program of Irradiation Testing for Fusion Research II) program.

References

1) Baluc N., Gelles D.S., Jitsukawa S., Kimura A., Klueh R.L., Odette G.R., van der Schaaf B., Yu Jinnan., J. Nucl. Mater. **367-370** (2007) 33.
2) Hasegawa A., Ejiri M., Nogami S., Satou M., Abe K., Kimura A., Jitsukawa S., CYRIC Annual Report (2006) 19.
3) Cho H.S., Kimura A., J. Nucl. Mater. **367-370** (2007) 1180.
4) Biersack J.P., Ziegler J.F., TRIM85 Program, IBM Corp., Yorktown, NY, 1985.
5) Hasegawa A., Wakabayashi E., Tanaka K., Abe K., Jitsukawa S., CYRIC Annual Report (2002) 34.

Table 1. The chemical composition of the 14Cr-ODS ferritic steel (unit: wt.%).

C	Si	Mn	Cr	W	N	Ti	Al	Y_2O_3	Fe
0.04	0.033	0.06	13.64	1.95	0.009	0.28	4.12	0.381	Bal.

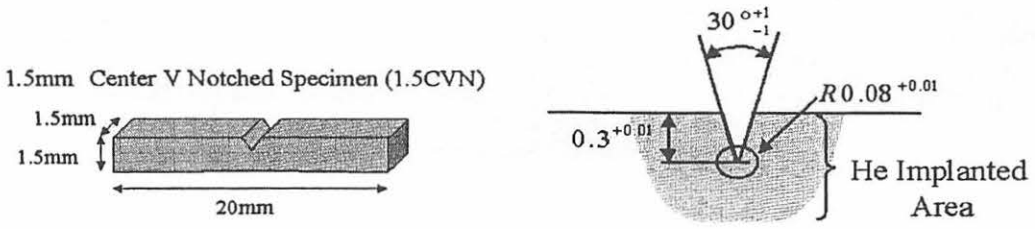

Figure 1. The shape and geometry of the miniaturized Charpy V notch (CVN) specimen.

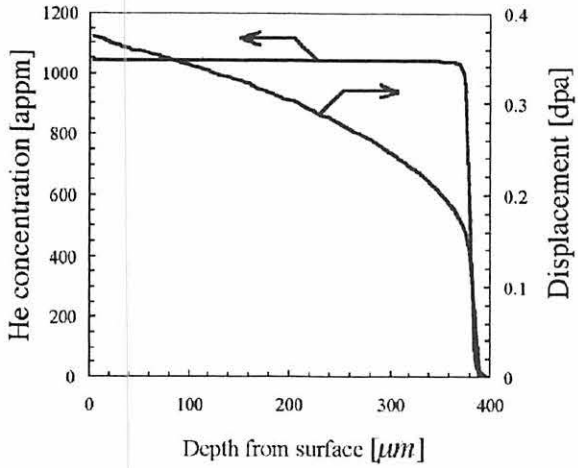

Figure 2. The calculated depth distribution of He concentration and displacement damage in the 14Cr-ODS steel..

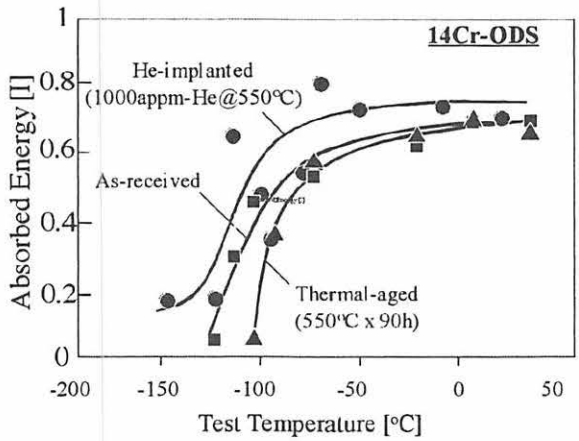

Figure 3. The Charpy impact data for the 14Cr-ODS steel..

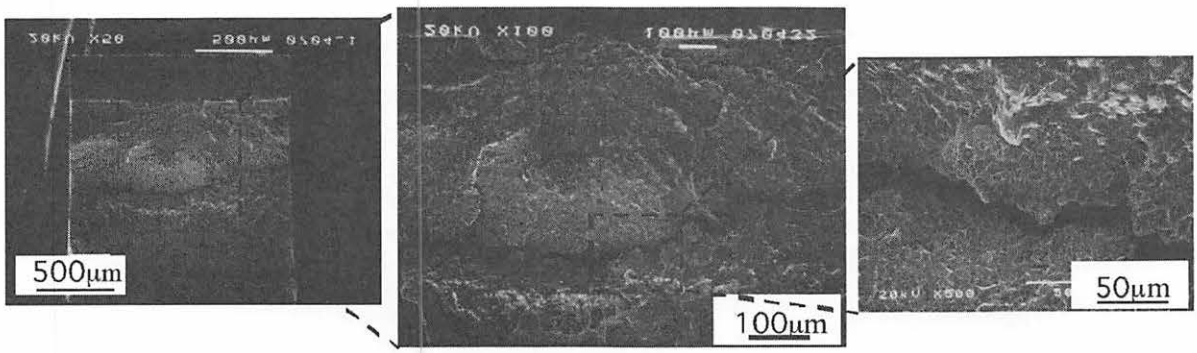

Figure 4. The typical fracture surfaces for the He-implanted Charpy impact specimen of the 14Cr-ODS steel tested at −146°C.

III. 2. Evaluation of Helium Effect on Candidate Structural Materials for Next Generation Long-life Nuclear Plant

Hasegawa A.[1], Nogami S.[1], Satou M.[1], Wakai E.[1], and Aoto K.[2]

[1]Department of Quantum Science and Energy Engineering, Tohoku University
[2]Japan Atomic Energy Agency

Introduction

For development of the next generation long-life nuclear plant, precise prediction of the irradiation damage to reactor vessel and in-core component during operation is necessary. This study focuses on the developing the index for evaluation of the irradiation damage for the candidate structural materials of the next generation long-life nuclear plant such as SUS304 steel, SUS316FR steel and 12Cr steel (HCM12A), which can be applied to reactor design method considering irradiation environment effect. This study also focuses on the developing the non-destructive inspection technique for precise understanding of irradiation damage progress during operation based on the index.

The amount of generated helium (He) is recognized as one of the promising index in this study. The database of mechanical property change for those materials due to He implantation should be established in order to verify whether He generation amount is adequate as the index for evaluation of the irradiation damage. Therefore, short time mechanical properties such as the tensile property (tensile strength and yield stress) and the hardness were evaluated in order to clarify the relation between He and their changes. Microstructure observation was also performed for analysis of the microstructure change due to He implantation.

Experimental

(1) He Implantation using Cyclotron

Material in this study is the 316FR steel, which is the candidate structural material for next generation nuclear plants. The chemical composition of these materials is shown in Table 1. The specimen shape was a miniaturized tensile specimen and a rectangular

specimen with geometry of 5 mm×16 mm×0.3 mm. The specimen surface was mechanically and electrically polished into mirror state.

The He implantation test was carried out using the AVF Cyclotron accelerator of Cyclotron and Radioisotope Center of Tohoku University. The implanted particle, implantation temperature and He concentration were 50 MeV He^{2+} ion, about 550°C and about 10 appm (implantation rate: about 0.3 appm/h), respectively. Helium was uniformly implanted from the specimen surface to about 400 μm in thickness by using a rotating energy degrader consisting of Al foils. Figure 1 shows the depth distribution of He concentration and displacement damage in the specimen calculated by SRIM code. The displacement damage in an iron produced by 50 MeV He^{2+} ion was about 2×10^{-4} dpa per 1 appm-He. The implantation temperature was measured using a thermocouple during implantation test, which was spot-welded to one of the implanted specimens.

(2) Tensile Test

Tensile test for the He implanted tensile specimen was performed using an Instron-type multi-purpose testing machine (INTESCO Co., Ltd.) at Radio Isotope Laboratory of Tohoku University. The test temperature, test environment and strain rate were about 550°C, vacuum below 1×10^{-3} Pa and about 6.7×10^{-4} s^{-1}, respectively.

(3) Hardness Measurement

The Vickers hardness measurement was performed using a Vickers hardness tester (Shimadzu Corp., Micro Hardness Tester type M) at Radio Isotope Laboratory of Tohoku University. The number of the test was 10 for each specimen. The test temperature, indentation load and dwell time was room temperature, 200 gf and 15 sec, respectively.

(4) Microstructure Observation by TEM

Microstructural observation for the He implanted specimen was performed using a transmission electron microscope (TEM, JEOL Ltd., JEM-2000FX) at International Research Center for Nuclear Materials Science of Tohoku University. Thin foil preparation for TEM observation was performed by electro-polishing using electrolyte solution with acetic acid and perchloric acid.

Results and Discussion

(1) Tensile Test

Figure 2 and Table 2 show the stress-strain curves for the miniaturized tensile specimen He-implanted up to about 10 appm (about 0.3 appm/h and about 1.7 appm/h[1)]) and the summary of the yield stress, tensile strength, uniform elongation, total elongation and reduction in area, respectively. Almost no effect of implantation rate on the tensile strength was observed. While, clear effect on the yield stress, uniform elongation, total elongation and reduction in area was observed. About 37% increment of the yield stress, about 25% reduction of the uniform elongation, about 33% reduction of the total elongation, and about 11% reduction of the reduction in area occurred by reducing the implantation rate from about 1.7 appm/h to about 0.3 appm/h.

(2) Hardness Measurement

Table 3 shows the summary of the Vickers hardness for the He-implanted specimen up to about 10 appm (about 0.3 appm/h and about 1.7 appm/h[1)]). Almost no effect of implantation rate on the Vickers hardness was observed. The results also showed that the hardness change due to He implantation was very small for both implantation rates.

(3) Microstructure Observation by TEM

Figure 3 shows the typical microstructure for the He-implanted specimen up to about 10 appm (about 0.3 appm/h and about 1.7 appm/h[1)]). Almost no effect of implantation rate on the Vickers hardness was observed. No He bubbles were observed both in the matrix and in the grain boundary.

Summary

Evaluation of the short time mechanical properties such as the tensile property and the hardness and observation of microstructure for He implanted 316FR by using Cyclotron was carried out in order to clarify the relation between He and their changes due to He implantation. The database of these properties was established for the He implanted specimen up to about 10 appm at about 0.3 appm/h and about 1.7 appm/h under the implantation temperature of 550°C.

Acknowledgement

Present study is the result of R&D Project on Irradiation Damage Management Technology for Structural Materials of Long-life Nuclear Plant entrusted to Japan Atomic Energy Agency (JAEA) by the Ministry of Education, Culture, Sports, Science and Technology of Japan (MEXT). The authors are grateful to the staffs of CYRIC of Tohoku University relating to the accelerator operation and our irradiation experiments.

References

1) Hasegawa A., Nogami S., Satou M., Wakai E., Aoto K., CYRIC Annual Report (2006) 25.

Table 1. The chemical composition of the 316FR steel (mass%).

	Fe	C	Si	Mn	P	S	Cu	Ni	W	Cr	Mo	V	Nb	N
316FR	Bal.	0.01	0.59	0.84	0.026	0.003	0.26	11.19	-	16.87	2.23	0.08	-	0.08

Table 2. The summary of the yield stress, tensile strength, uniform elongation, total elongation and reduction in area.

Material	He Concentration [appm]	He Implantation rate [appm/h]	Yield Stress [MPa]	Tensile Strength [MPa]	Uniform Elongation [%]	Total Elongation [%]	Reduction in area [%]	Ref.
316FR	0	—	139.8	368.0	31.6	34.8	99.5	1)
	10	1.7	91.8	354.7	40.8	46.1	95.3	1)
	10	0.3	125.5	345.7	30.7	31.0	85.0	—

Table 3. The summary of the Vickers hardness.

Material	He Concentration [appm]	He Implantation rate [appm/h]	Vickers hardness Hv		Ref.
			Average	Std. Dev.	
316FR	0	—	172.7	16.3	1)
	10	1.7	169.0	17.2	1)
	10	0.3	175.1	4.5	—

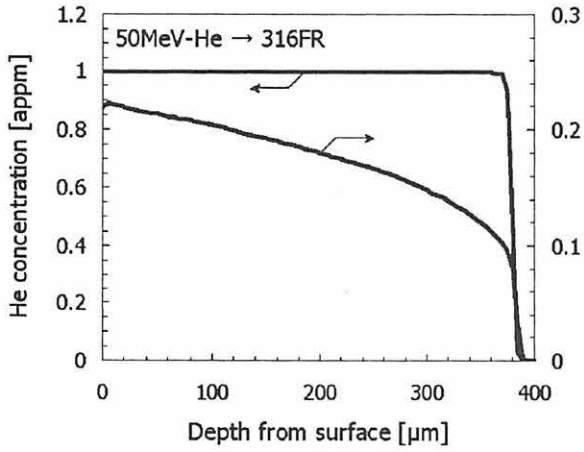

Figure 1. The depth distribution of He concentration and displacement damage. calculated by SRIM code.

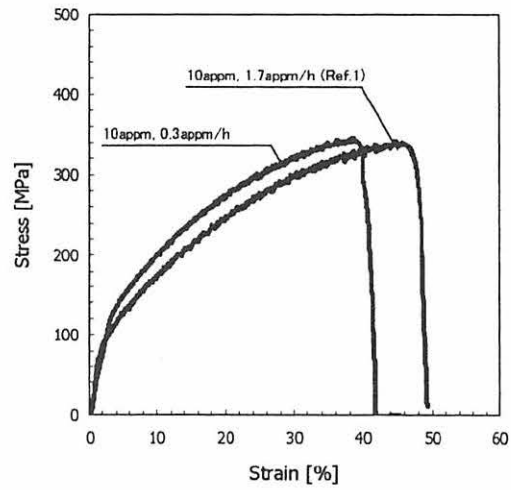

Figure 2. The stress-strain curves for the He implanted miniaturized tensile specimen.

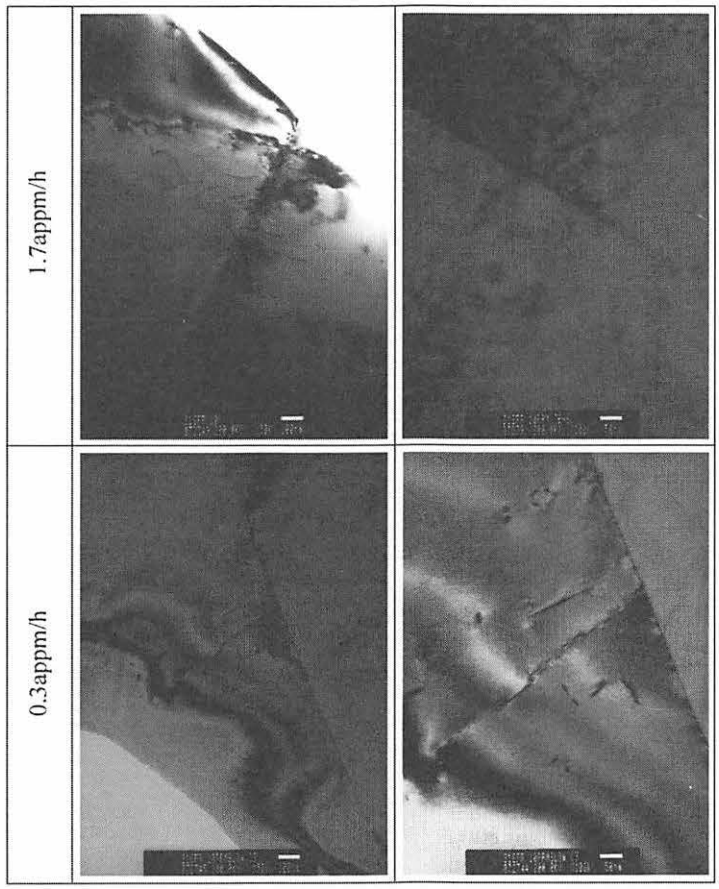

Figure 3. The microstructure of the He implanted 316FR steel up to about 10 appm.

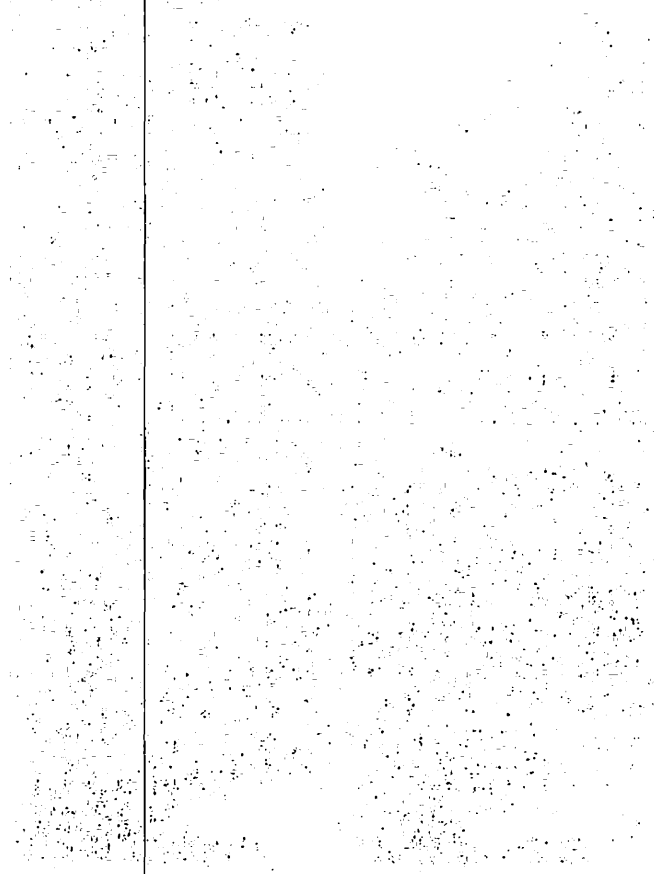

IV. NUCLEAR MEDICAL ENGINEERING

IV. 1. Study on Respiration-synchronous Irradiation in the Spot-beam Scanning Technique

Terakawa A.[1], Ishii K.[1], Yamazaki H.[2], Matsuyama S.[1], Miyashita T.[1], Chiba T.[1], Yamamoto T.[1], Arikawa J.[1], Togashi T.[1], Yamashita W.[1], Akiyama H.[1], Koyata H.[1], Itoh N.[3], Sano T.[3], Wada S.[3], and Orihara H.[4]

[1]Department of Quantum Science and Energy Engineering, Tohoku University
[2]Cyclotron and Radioisotope Center, Tohoku University
[3]School of Veterinary Medicine and Animal Sciences, Kitasato University
[4]Department of Intelligent Electronics, Tohoku Institute of Technology

The spot-beam scanning irradiation in charged-particle therapy provides a three-dimensional dose distribution which agrees with the tumor shape without high level dose in the surrounding normal tissue. The scanning technique has currently been limited in treatment for cancers having no respiration movement because the beam control is highly sensitive to the target movement.

We have developed respiration-synchronous operation system in the spot-beam scanning technique by using the horizontal beam irradiation facility[1)] for proton therapy experiments. The respiration-synchronous irradiation needs the measurement of displacement of the cancer position due to the respiration. If a relationship in the respiration movements between the body surface and an organ is obtained, it would be possible to monitor the displacement of the cancer position in the organ from that of the body surface.

We performed the experimental study on the respiration-synchronous beam-scanning method with a moving target. In order to evaluate the relationship between the surface and the organ movements, the motions of the surface and liver of a dog were measured[2)] from X-ray transmission images with gold markers at Veterinary Teaching Hospital, Kitasato University as shown in Fig. 1. The results show no significant difference in phase between their periodical movements.

The experiments were performed using an 80-MeV proton as an incident spot beam and a moving target which simulates the movement of the body surface in the lateral

directions as shown in Fig. 2, whereas two laser rangers were used for measuring the displacement of the target position in the horizontal and vertical directions. The irradiation was allowed at the end of breathing because there were little changes in the positions of both the surface and the organ.

In Fig. 3, the experimental results for the lateral intensity distributions by the spot-beam scanning technique with the synchronous irradiation are shown and compared with those without the synchronous operation. The dose distribution was measured with an Imaging Plate[3] attached to the moving target. We confirmed that the irradiation fields were successfully generated in the case of the synchronous operation, whereas the non-synchronous irradiation provided unnecessary dose outside the target region. The depth-dose distribution by the scanning technique is also in good agreement with the simulation as shown in Fig. 4.

References

1) Terakawa A., et al., CYRIC Annual Report (2006) 41.
2) Houdatsu T., a graduation thesis (2007), School of Veterinary Medicine and Animal Sciences, Kitasato University
3) Fuji Photo Film Co., Ltd.

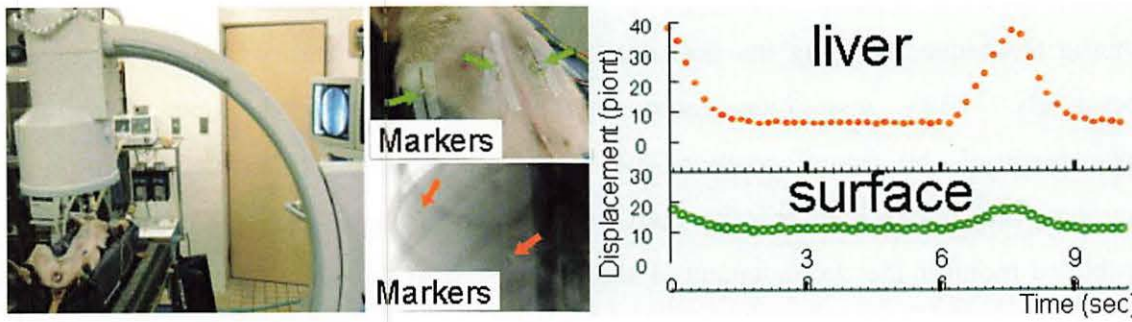

Figure 1. Respiration motion measurements[2] for the body surface and the organ of a dog.

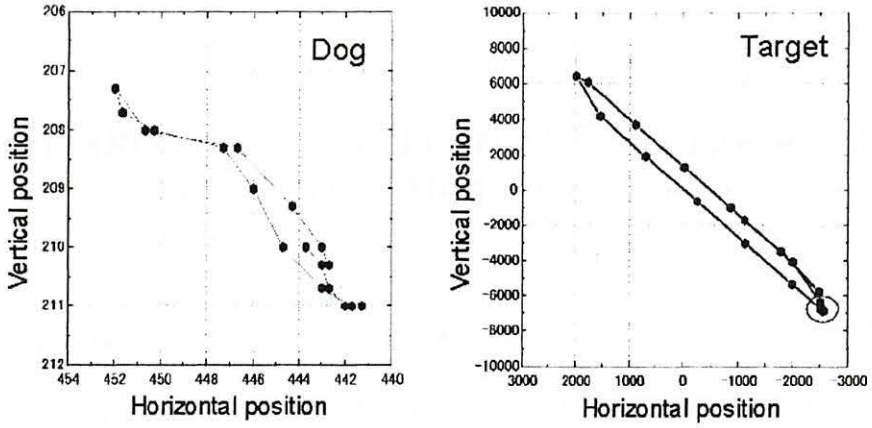

Figure 2. Respiration movements of the body surface of a dog and the simulated movement of the target. The frequency of dog's respiration controlled by anesthesia is 8 s^{-1}. The circle in the graph for the target indicates the area in which the irradiation is allowed.

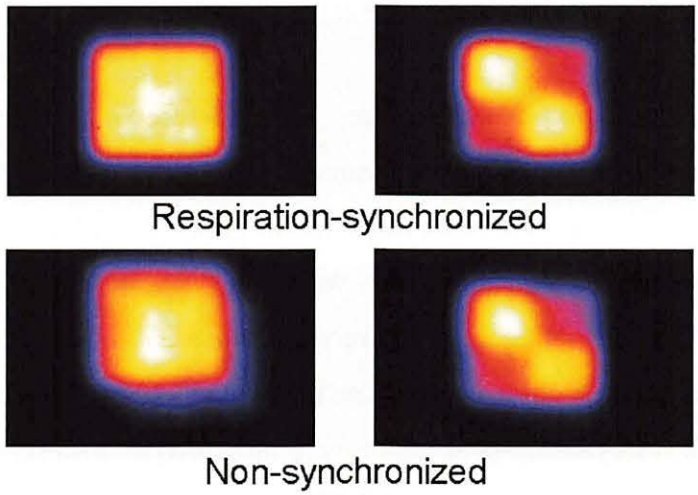

Figure 3. Lateral irradiation fields for the moving target with and without the respiration-synchronous operation.

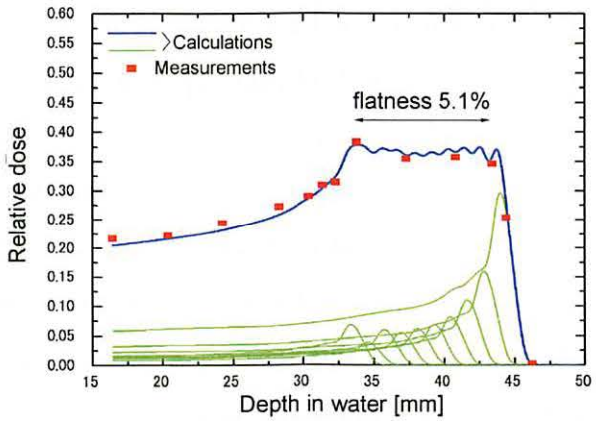

Figure 4. Depth-dose distribution (spread-out Bragg peak) provided by the spot-beam scanning technique with the range-shifter.

IV. 2. Biological Assessment of Proton Beams SOBP of CYRIC for Small Animal Cancer Therapy.

Itoh N.[1], Wada S.[1], Sano T.[1], Arakawa M.[1], Terakawa A.[2], and Ishii K.[2],

[1]School of Veterinary Medicine and Animal Sciences, Kitasato University
[2]Department of Quantum Science and Energy Engineering, Tohoku University

Recently, cancer is increasing in small animal diseases and radiotherapy is applied. So, ion beam radiotherapy is being watched with interest to cancer therapy to acquire high therapeutic effects.

To assess the biologic effects of proton beams before small animal cancer therapy, cultured cells from canine squamous cell carcinoma (S cells) were irradiated at 5 points along 80 MeV per nucleon proton beams with mono-peak and with Bragg peaks modulated to 2 cm widths (SOBP). A gamma ray was used as a reference. Relative biologic effectiveness (RBE) values at each point were calculated from survival curves and were calculated from cell survival curves at the dose that would reduce cell survival to 10%.

Surviving curves by mono-peak beam were measured at 10 mm, 43.5 mm, 44.5 mm and 45.5 mm depth in water (Fig. 1), and LET values were 1.03 keV/μm, 4.88 keV/μm, 5.03 keV/μm and 0.95 keV/μm, respectively. RBE values at 10 mm, 43.5 mm, 44.5 mm and 45.5 mm depth in water were 1.07, 1.44, 1.49 and 1.08, respectively (Fig. 2). This result indicates that RBE values increase LET values. Surviving curves by SOBP were measured at 10 mm, 25 mm, 34 mm and 42 mm depth in water (Fig. 3), and SOBP was produced from 25 mm to 42 mm. RBE values at 10 mm, 25 mm, 34 mm and 42 mm depth in water were 1.01, 1.07, 1.07 and 1.13, respectively. Biologic doses that include physical effect and biological effect were calculated at each depth and represented 72%, 103%, 104% and 109%, respectively (Fig. 4). Coefficient of variation of biologic doses in SOBP (three points) represented within 3%. This result indicates that uniform biological effect and high cell lethal effect were acquired in SOBP of CYRIC.

In this study, it was considered that more effective cancer therapy for small animals was achieved by using proton beam SOBP developed at CYRIC.

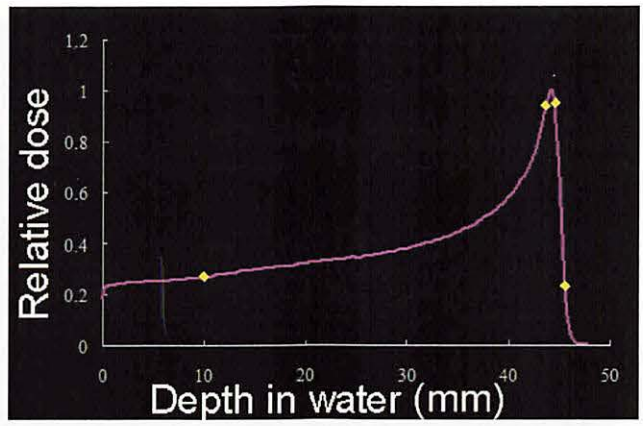

Figure 1. Depth dose distribution of an 80-MeV proton beam.

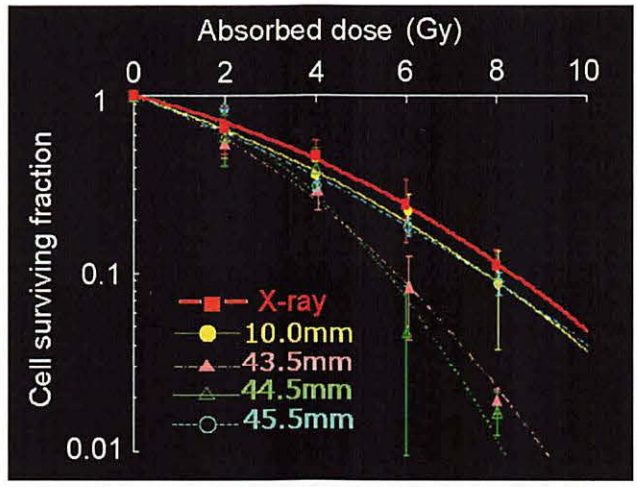

Figure 2. Cell surviving fractions measured at different depths for the 80-MeV proton.

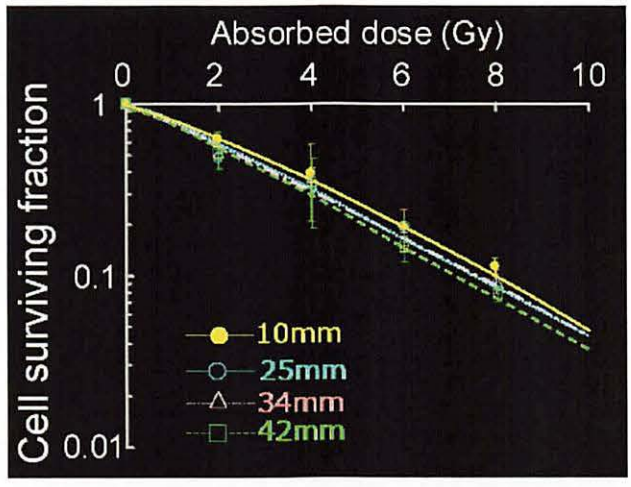

Figure 3. Cell surviving fractions measured at different depths for the proton beam with the 20mm-SOBP width.

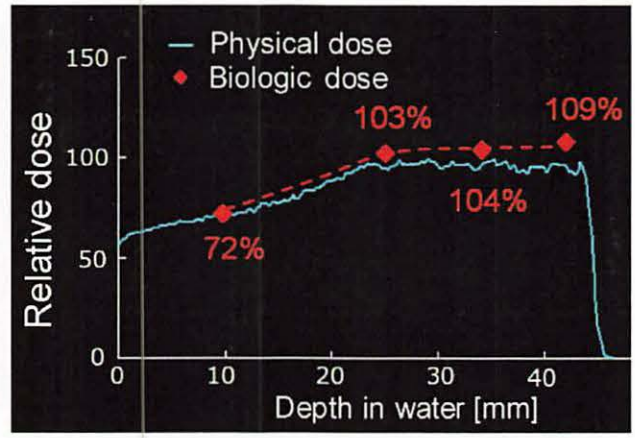

Figure 4. Biologic depth-dose distribution of the SOBP beam.

IV. 3. High Sensitivity Radiochromic Film Dosimetry Using an Optical Common-mode Rejection and a Reflective-mode Flatbed Color Scanner

Ohuchi H.

Graduate School of Pharmaceutical Sciences, Tohoku University

Introduction

Radiochromic film (RCF) is a thin, plastic, 2D planar dosimeter offering ease of handling and broadly applied in dosimetry[1-3]. However, its low sensitivity precludes their application to measuring lower doses accurately. Assuming macroscopic and microscopic non-uniformities of film layers, including the thickness variations in the film's active radiochromic layer and coating, were the main causes of light disturbance (noise) against the lights (signal), resulting in a lowering of actual film sensitivities, we developed an optical common-mode rejection (CMR) that can improve the dosimetric sensitivity limit of radiochromic films by using a spectrophotometer[4]. The R component is highly sensitive to radiation exposure as two absorption peaks are located at wavelengths of 675 and 617 nm[5], while the G component is less sensitive than R component is, owing to the absence of a clear absorption peak in the green waveband. The two light components suffer a common fate, with the exception of wavelength-dependent events, having passed together along common attenuation paths. The ratio of the two components (R:G) is analogous to the 'common-mode rejection' in electronics, where the factors common to both numerator and denominator cancel out. This result indicated that the CMR can compensate the variation in the film's active radiochromic layer by using red and green components.

In this paper, the optical CMR scheme was applied to the R and G component outputs from a flatbed color scanner in reflection mode used to scan a Gafchromic XR type R dosimetry film after irradiation with X-rays. Two types of dose-response curves obtained by the optical CMR scheme using ratios of red/green and the conventional analysis method using red component were produced. With a linear fit in the range from 3.7 mGy to 0.81 Gy, the agreements in both curves between measured and fitted data were

compared.

Materials and methods

The radiochromic film model GafChromic XR type R, produced by ISP (International Specialty Products), was used. The active layer of 15 μm thick is sandwiched between the two substrates of 97 μm polyester, one of which is transparent and the other is opaque (white). XR type R film pieces (2×2 cm square) were exposed to X-ray beams of 100 kV with a 1.0-mm Al filter from an MBR-1520R unit (Hitachi Medico Co.) in the range from 3.7 mGy to 8.1 Gy. The amount of radiation was monitored with a thimble ionization chamber installed inside the unit. It is traceable to the Japanese national standard maintained by the Japan Quality Assurance Organization. The films were scanned before and twenty-four hours after exposure with an Epson ES-10000G flatbed color image scanner (SEIKO EPSON Corporation) with 1200 dpi resolution and 16 bits per color of the digital resolution dpi. The scans were performed in reflection mode using a white lid with no color correction factors or filters. A 2×2 cm square area with uniform response was identified by performing blank scans with the same condition described above and delimitated in order to use only this area for digitalization.

For each film, scanning was repeated five consecutive times and acquired images were averaged. The obtained digital data were evaluated using self-written routines in MATLAB 7.3 software (The Mathworks). The digital data before exposure was subtracted pixel-by-pixel from the post-exposure image for each film. The serial images obtained by scanning each film before and after exposure were aligned using fiducial marks. After mathematical operations, the averages and standard deviations of the results were taken for 1×1 cm square (approximately 472×472 pixels) at the center of each film.

The reflectance is obtained as digitalized output of the R, G, B component, when films are scanned by a color scanner in reflection mode. The relationship between reflectance (Rf) and optical density (OD) used in film dosimetry can be expressed as follows,

$$OD = \log_{10}(2^{16}/Rf),$$

$$\text{net } OD = OD - OD_0 = \log_{10} Rf_0 - \log_{10} Rf = \log_{10} (Rf_0/Rf) \qquad (1)$$

where subscripts denote unirradiated background quantities and 'net' stands for the quantities after removing the background.

The conventional analysis way uses only red component, at which net OD - Rd is

defined as,

$$\text{net OD\_Rd} = \log_{10} (Rd_0/Rd) \quad (2)$$

In the optical CMR scheme, in which red and green components are used, Rf should be replaced by Rd/Gr, where Rd and Gr are each amount of reflectance lights. Thus, net reduced OD (net ROD_Rd_Gr) in the optical CMR scheme is written as,

$$\text{ROD\_Rd\_Gr} = \log_{10} (Rd/Gr),$$

$$\text{net ROD\_Rd\_Gr} = \log_{10} ((Rd_0/Gr_0)/(Rd/Gr)) \quad (3)$$

Results and discussion

Figure 1 shows the absorption spectra, obtained using a GretagMacbeth SpectroEye reflection spectrometer, for GafChromic XR type R film unirradiated and exposed to 8.1 Gy of X-ray over the range of 380 - 730 nm in 10 nm steps and an example of filter functions for red, green, and blue wavebands on CCD. The results show the absorption spectra produce two pronounced peaks located around at 670 nm and 610 nm, which are lying in the red region of the light spectra and both responsible for the same R output from the color scanner. It also shows that the G output is less sensitive than the R output due to the absence of a clear absorption peak in the green waveband.

The two dose-response curves as a function of delivered dose ranging from 3.7 mGy to 8.1 Gy for 100 kV X-ray beams and from films scanned 24 hrs after exposure are plotted in Fig. 2. Closed triangles represent the net optical density obtained by using red component in Eq. (2) and open circles show the net reduced OD calculated by Rd and Gr components in Eq. (3), respectively. Error bars are shown in the figure as one standard deviation for data of approximately 472×472 pixels. Since these figures indicate that the type R film response is nonlinear, second-order polynomial fits were applied to each of the two curves exhibited. In order to evaluate the validity of the fit, the errors of fitting equations for two types of indices, OD_Rd and ROD_Rd_Gr were analyzed by obtaining residuals defined by Eq. (4).

$$OD_{residuals} = OD_{meas.} - OD_{calc.} \quad (4)$$

where $OD_{esiduals}$, $OD_{meas.}$, and $OD_{calc.}$ are the residuals, the experimental results (ODs), and the calculated ODs, respectively.

Figure 3 shows the quotients obtained by dividing each residual at measured dose by the standard deviation (error), σ of all residuals on each index. For an index of ROD_Rd_Gr, the quotients consistently increase up to 0.81 Gy. The similar tendency is

observed in an index of OD_Rd, though deviation among samples is apparently exhibited. This consistent tendency indicates that second-order polynominal fits are not appropriate below 0.81 Gy. Then, linear fits were applied to the measured values of both indices in the dose-response ranging from 3.7 mGy to 0.81 Gy. Figure 4 shows the net optical densities of OD - Rd (closed triangles) and ROD_Rd_Gr (open circles), demonstrating each regression line and equation without y-intercept. Figures 5(a) and 5(b) show the expanded figures for two indices of OD_Rd and ROD_Rd_Gr. respectively, in the low range less than 0.1 Gy in Fig. 4. Figure 5(a), representing the measured values obtained with a conventional analysis using the red component, exhibits a large discrepancy in measured optical densities among samples and does not show a consistency with a linear fit under 81 mGy. This is consistent to product specification; describing the dose of 0.1 Gy is the lowest detectable dose. However, in Fig. 5(b), the measured optical densities of the same samples obtained with the optical CMR scheme show a good consistency among each other and all values show an improved consistency with a linear fit within one standard deviation of each measured optical densities. These results indicate that the CMR scheme makes it possible to reproduce the measured optical densities and measure the dose in the lower range.

Comprehensive results of this study by using the XR type R films and a reflective-mode flatbed color scanner demonstrated that the optical CMR is a novel method to greatly improve the sensitivity limit by mitigating the effects of RCF film nonuniform response and lowering noises. It can be applied to any type of radiochromic films and RGB color scanners in transmission mode as well.

References

1) Cheung J. Y. C., Yu K. N., Ho R. T. K., Yu C. P., Med. Phys. **26** (1999) 1252.
2) Fiandra C., Ricardi U., Ragona R., Anglesio S., Giglioli F. R., Calamia E., Lucio F., Med. Phys. **33** (2006) 4314.
3) Morris K. N., Weil M. D., Malzbender R., Phys. Med. Biol. **51** (2006) 5915.
4) Ohuchi H. and Abe K., Nucl. Instrum. Methods Phys. Res.**A 558** (2006) 576.
5) Butson M. J., Yu P. K. N., Cheung T., Metcalfe P., Mater. Sci. Eng. **R. 41** (2003) 61.

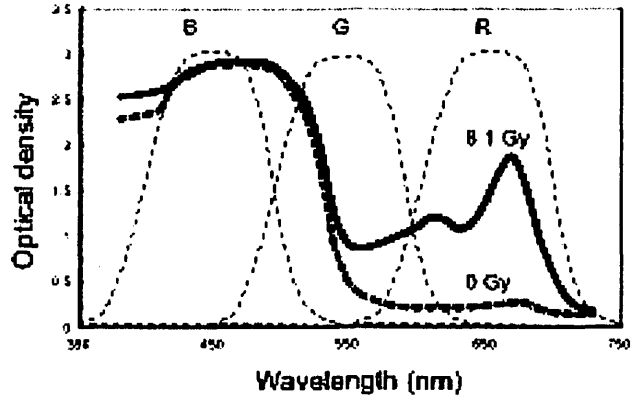

Figure 1. Absorption spectra for GafChromic XR type R film unirradiated and exposed to 8.1 Gy of X-ray over the range of 380 - 730 nm in 10 nm steps and an example of filter functions for red, green, and blue wavebands on CCD.

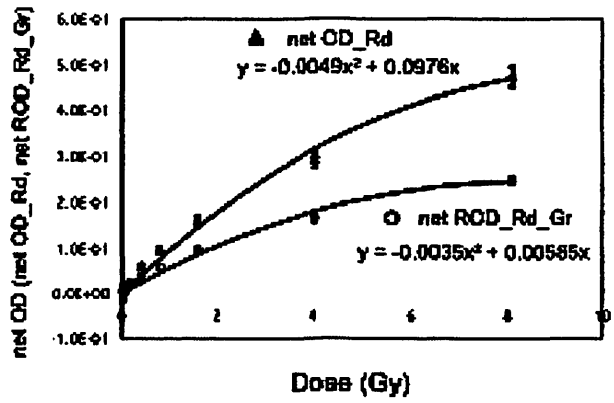

Figure 2. Dose-response curves as a function of delivered dose ranging from 3.7 mGy to 8.1 Gy for 100kV X-ray beam and from films scanned 24 hrs after exposure.

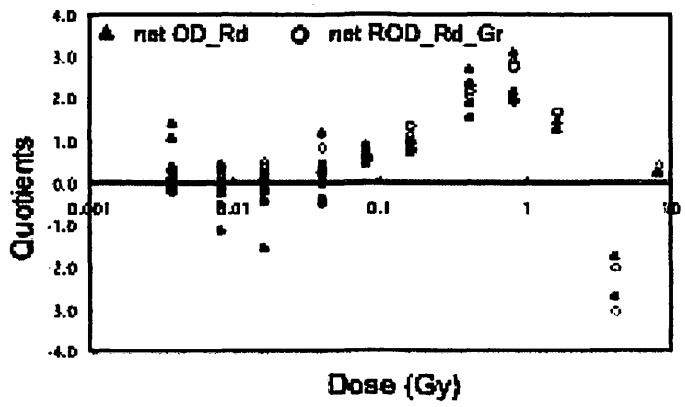

Figure 3. Quotients obtained by dividing each residual at measured dose by the standard deviation (error), σ of all residuals on each index. For both indices of OD_Rd and ROD_Rd_Gr, the quotients consistently increase up to 0.81 Gy.

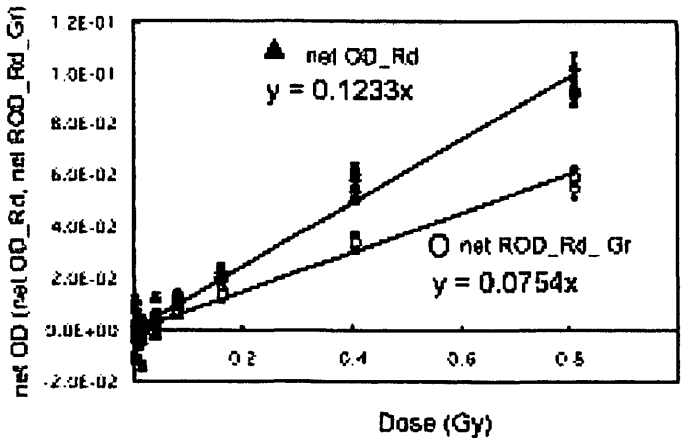

Figure 4. Net optical densities of OD_Rd (closed triangles) and ROD_Rd_Gr (open circles) demonstrate each regression line of linear fits and equation without y-intercept.

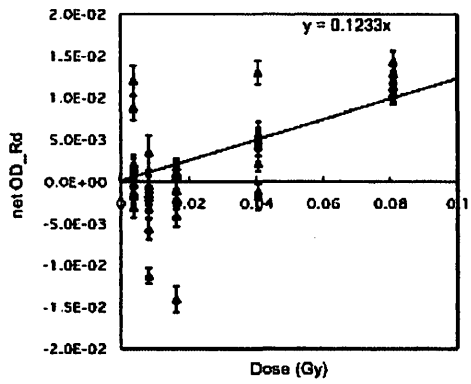

Fig. 5 (a)

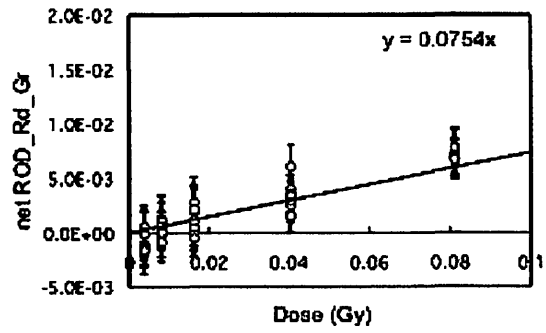

Fig. 5 (b)

Figure 5. Expanded figures in the low range less than 0.1 Gy in Fig. 4. Figure 5(a) represents the measured values for an index of OD_Rd and exhibits a large discrepancy in measured optical densities among eight samples and does not show a consistency with a linear fit under 81 mGy. Figure 5(b), representing the measured optical densities of eight samples obtained with the optical CMR scheme, shows a good consistency each other and an improved consistency with a linear fit within one standard deviation of each measured optical densities.

IV. 4. Development of a New Positron Emission Mammograph (PEM)

Miyake M.[1], Yamamoto S.[3], Itoh M.[1,4], Kumagai K.[1], Sasaki T.[1], Targino Rodrigues dos Santos[1,5], Tashiro M.[1], and Baba M.[2]

[1]*Divisions of Cyclotron Nuclear Medicine*
[2]*Radiation Protection and Safety Control, Tohoku University Cyclotron and Radioisotope Center, Tohoku University*
[3]*Department of Electrical Engineering, Kobe City College of Technology*
[4]*Sendai Medical Imaging Clinic*
[5]*CMI, Inc.*

Introduction

Breast cancer is one of the leading causes of death among Japanese women. This malignancy can be treated relatively easily when detected early. The highest incidence of breast cancer is observed among those in their thirties and forties. The high incidence among these age groups considerably affects our society because women in these generations usually play important roles in their families and working places.

Recently, imaging modalities such as X-ray mammography and/or ultrasonic echography have proven useful for the detection of breast cancer. However, these modalities provide only morphological information. On the other hand, younger women or women without a history of breastfeeding tend to develop mammary gland tumor. In some cases of X-ray mammography, a developing mammary gland produces shadows on mammography images, making detection of breast cancer difficult.

Positron emission tomography (PET) for whole-body diagnosis can provide functional information on cancerous tissues including the degree of malignancy, as reflected by the level of accumulation of a tracer, [^{18}F]fluoro-deoxyglucose. However, various problems still remain such as limited spatial resolution and motion artifacts due to respiration movement, as well as high costs for device installment and maintenance. In measuring events of the coincidences of positrons, a larger distance between detectors, as seen with PET scanners, for whole-body imaging limits spatial resolution. To compensate these weak points, we have started to develop a positron emission mammography (PEM) scanner dedicated for the local diagnosis of breast cancer.

The name of our project is "development of high resolution PEM equipment that shows the next generation breast cancer diagnosis", granted by the regional research and development resources utilization program from Japan science and technology agency (JST).

Basic concept and scintillator

The basic concept of PEM development consists of the compact radiation detectors, high-speed electronic circuit, and lower cost of equipment. Finally, the PEM scanner is expected to achieve a high spatial resolution of about 1 mm, which is a quarter of the resolution of conventional PET scanners. Regarding the radiological dose to be needed for examination would be low as much as 20 MBq, approximately one tenth of the dose of conventional PET scanners. Cost performance is also an important issue, and PEM can be developed with the costs of one fifth of the conventional PET scanner.

In our new scanner, a new crystal of praseodymium doped "lutetium aluminum garnet" (LuAG)[1] is used as a novel scintillator in this project. Table 1 shows the summary of comparison of performances of different scintillators. This new scintillator has some advantages such as a short fluorescence lifetime, a low manufacturing cost and a high light output.

Image mapping system

The image mapping system is used for diagnosis of the crystal. The system consists of a personal computer, the core with amplifiers, analog-to-digital converters and the dark box for the scintillation measurement (Fig. 1). The system is set up in a personal computer rack. A flat panel photomultiplier tube (PMT), H8500, made by Hamamatsu photonics, is used for the scintillation mapping. The mapping method is based on the center of gravity calculation. The system has the gain correction function for the variety of the multi anode outputs from a flat panel PMT. The system can measure the energy spectrum of the scintillation.

PEM simulator

Presently, we are still in the process of developing a PEM scanner, and we will also fabricate a prototype PEM scanner for commercial use. This scanner will be used for detecting smaller tumors, and it will be cheaper and smaller than the conventional PET

scanner. We are aiming for a spatial resolution of <1-2 mm, and the price will be 20% lower than that of the conventional PET scanner.

The PEM simulator is set up in a personal computer rack and a worktable and used for the diagnosis of the crystals and the PMTs. Last year, we developed several test devices and a PEM simulator. One of these devices is a block detector device. This device is constructed from a flat-panel photomultiplier tube (FP-PMT), an inorganic scintillator crystal array, an aluminum case and a signal processing circuit. The FP-PMT is a multianode PMT with 16×16 anodes and has positional sensitivity. The PEM simulator is a testing and an evaluating system of the PEM scanner. The simulator has four block detector devices, high voltage supply units for PMTs and signal processing units. The latter consists of an analog amplifier, an analog to digital converter, Field Programmable Gate Array (FPGA) devices and communication interface for PC (Fig. 2).

In summary, this project is now in progress steadily for developing the prototype PEM scanner. As the PEM simulator was developed with other scintillator, we are trying to optimize the performance after being equipped with the new LuAG scintillator. We will assemble and test larger size LuAG scintillator crystal block arrays. We will also develop additional softwares for image reconstruction, gantry control, patient registration and so on. Finally when this project is finished, we hope that a new possibility will be opened to the breast cancer diagnosis.

References

1) Ogino H., Yoshikawa A., Nikl M., et al., J. Crystal Growth **292** (2006) 239.

Table 1. The performance comparison of the scintillators. Pr:LuAG scintillator is better than another scintillators in a shorter fluorescence lifetime, a lower manufacturing cost and a higher light output.

	Pr:LuAG	BGO	GSO	LSO
Scintillation w.l. (nm)	310~370	480	440	420
Light Yield (ratio BGO)	320	100	200	400~500
Scintillation decay time (ns)	20	300	56	41
Manufacturing cost (yen / cm^3)	2,500	2,000	4,000	5,000
Density (g / cm^3)	6.7	7.13	6.8	7.4
Melt point (deg)	1,970	1,050	1,950	2,150
Advantages	high yield, short FLT	low cost	proven to be better than BGO	high yield, high density
Disadvantages	short wave length, segregation	low yield, long FLT	cleavage (crack and processing difficulty)	segregation, manufacturing difficulty

*abbreviations: FLT= fluorescence lifetime

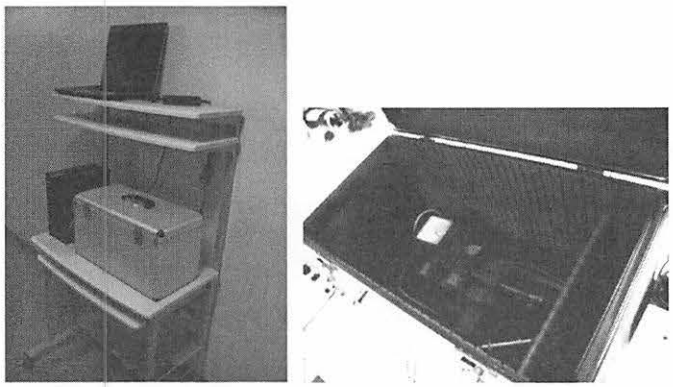

Figure 1. Left is the image mapping system consists of a personal compulter, the core with amplifires, analog to digtal converts and so on, and the dark box for the scintillation measurement. Right is inside the dark box.

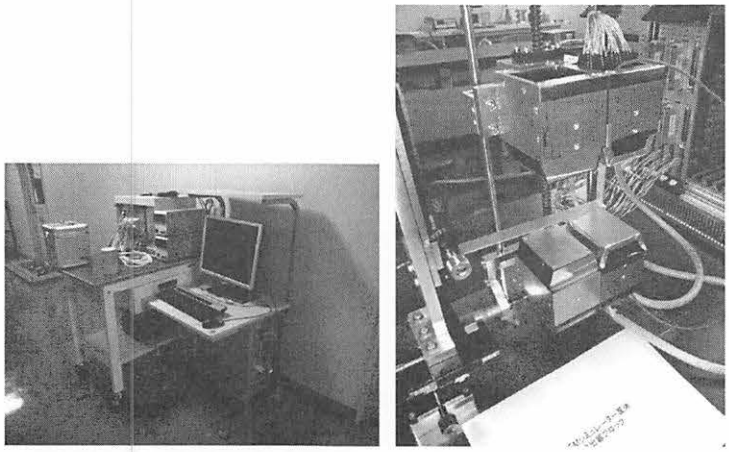

Figure 2. Left is the PEM simulator. The PEM simulator is a subset of the PEM scanner and used for the diagnosis of the crystals and the PMTs. Right is a close up of the detector units.

IV. 5. The Use of Nuclear Medicine Systems for Veterinary Care and its Future Prospects

Miyake M.[2], Tashiro M.[2], Itoh M.[2], Sugawara A.[2], Kikuchi Y.[1], Yamazaki H.[2], and Ishii K.[1,2]

[1]Graduate School of Engineering, Tohoku University
[2]Cyclotron and Radioisotope Center, Tohoku University

Nuclear medicine as a veterinary medicine in the United States

In the United States, the federal (Nuclear Regulatory Commission, NRC), state and local governments have been authorizing the medical use of radiation in veterinary care. In the 1980s, nuclear medicine was introduced to the field of veterinary care and was established as a specialized filed in the 1990s. However, it seems that the use of radioisotopes for the veterinary care has been permitted as a part of "medical" use since there has been no provision specified for veterinary care. Thus, the permission seems to cover basically "human use" but also be applicable to domestic animals including pets and non-meat animals.

Currently in the United States, clinical investigations using radioisotopes have been commonly done for diagnosis of fractures among race horses. Fractures among race horses may affect not only the horses' ability for racing but also their lives. In addition, the fracture shall make the horse-riders exposed to the risk of severe injury due to falling-off, so the prevention of fracture has been a very important issue in the clinical race-horse medicine. A radioactive tracer, the ^{99m}Tc-MDP, which has high affinity to the bone tissue, is used for the diagnosis of fracture in race horses. This tracer highly accumulates in a part of the bone tissue where bone-remodeling is activated, and can be used for diagnoses of "stress fracture" before resulting in complete fracture as well as "periostitis" that cannot be detected by X-ray.

Recent application of nuclear medicine for animals in Japan

In Japan, nuclear medicine examinations have been exclusively conducted for basic

research using experimental animals such as rats and mice, while few examinations have been done as clinical routines on pet animals. To date, there is no regulatory laws specifically applying to nuclear medicine examinations used in veterinary care, and the "Law Concerning Prevention of Radiation Hazards due to Radioisotopes, etc." is directly applied. Therefore, animals treated with radioisotopes, in principle, should be sacrificed and kept in a radiation controlled area and finally should be disposed as nuclear wastes.

Current state of nuclear medicine examinations for veterinary care

Currently, X-ray photograph is taken very often in the field of veterinary medicine in Japan, but nuclear medicine examination is seldom done. An important reason for the current situation would be the fact that the legislation for conducting nuclear medicine examination is not ready yet, and the Law Concerning Prevention of Radiation Hazards due to Radioisotopes, etc. is limiting the use of radiopharmaceuticals to pet animals.

However, the current attitude of pet animal owners has been changing because of aging and variation of diseases among pet animals. The growing demand for advanced medical technology also for veterinary care has been encouraging the inclusion of nuclear medicine technique as a field of veterinary medicine. As already proven to be useful in the United States, the nuclear medicine is effective to prevent the injuries such as stress fractures among the race horses and therefore to reduce the risks of horse-riders' falling-off in the race. The nuclear medicine such as PET and SPECT may be also useful for diagnosis in pet animals such as dogs and cats. SPECT imaging has already been applied to evaluation of the regional brain activity in dogs with anxiety disorder in Europe[3].

Future veterinary nuclear medicine

In order to meet the growing demand for improved veterinary care, a "working group on technical standards for radiation protection in veterinary nuclear medicine" was formed in the "Radiation Council" of the Ministry of Education, Culture, Sports, Science and Technology, Japan. This working group has discussed over an improvement of the legislation. For a moment, the following 3 types of the target contents and animals are under consideration,

use of ^{99m}Tc bone scintigraphy to a horse,

use of variety of ^{99m}Tc scintigraphy to a dog and cat, and

use of ^{18}F-FDG PET to a dog and cat.

Regarding the practical legislation, new standards (laws) comparable to the Law Concerning Prevention of Radiation Hazards due to Radioisotopes, etc. and the "Medical Service Law". Such a new standard is now considered for the radiation control of the facilities and the equipments radiation management of facilities and equipment for these tests.

Nuclear medicine equipments for animal in CYRIC

Currently at CYRIC, Tohoku University, there are three PET systems and a gamma camera system as nuclear medicine equipments for animals (Figs. 1 and 2). Table 1 shows the specification of these nuclear medicine systems at CYRIC. The ultra-high resolution semiconductors PET system (fine PET) is available for small animals such as rats and mice[1,2]. The PET systems, the PT-931-04 and the HEADTOME-IV are available for investigations of medium-sized animals. ZLC-7500 gamma camera is also available for medium-sized animals by using a parallel collimator and for small-sized animals by using a pinhole collimator.

Future prospects

We are going to continue basic experiments with radioisotopes as it has been. We hope the further advancement of basic research including drug development by using the ultra-high resolution semiconductors, PET-the-art system. In order to initiate clinical veterinary care at the CYRIC, we may have many things to do. We may need a renovation of the facility for veterinary care, recruitment of veterinary doctors and staffs to take care of radioisotope-treated animals. It is also important to examine the conditions regarding when and how the radioisotope-treated animals can be released from the controlled area.

References

1) Ishii K., Kikuchi Y., Matsuyama S., et al., Nucl. Instrum. Meth. **A 576** (2007) 435.
2) Kikuchi Y., Ishii K., Yamazaki H., et al., Nucl. Instrum. Meth. **B 241** (2005) 727.
3) Vermeire S., Audenaert K., Dobbeleir A., et al., Eur. J. Nucl. Med. Mol. Imaging. **35** Suppl.2 (2008) S150.

Table 1. Specification of nuclear medicine systems for animal in CYRIC.

	Ultra-high resolution semiconductors PET system	PT-931-04 PET system	HEADTOME-IV PET system	ZLC-7500 gamma camera
Crystal	CdTe	BGO	BGO	NaI(Tl)
Num of crystals	5120	2048	3072	1
Num of slices	16	7	7	N.A.
Field of view	6.4 cm (diameter) x 2.4 cm (axial)	65 cm (diameter) x 4.7 cm (axial)	51.2 cm (diameter) x 8.8 cm (axial)	387 mm (crystal diameter) x 9.5 mm (crystal thickness)
Spatial resolution	under 1 mm	5.0 mm ~ (diameter) x 6.7 mm ~ (axial)	4.5 mm ~ (diameter) x 11.0 mm (axial)	3.9 mm (intrinsic)
etc				energy resolution : 10.1 % (^{99m}Te) nuclide : ^{99m}Te, ^{201}Tl, ^{123}I, ^{131}I, ^{67}Ga, ^{111}In etc collimator : high resolution parallel, middle energy parallel, pinhole etc

Figure 1. Nuclear medicine systems for animals. Left figure shows PET systems. From the left, ultra-high resolution semicondoctors PET system, PT-931-04 PET system, HEADTOME-IV PET system. Right figure shows ZLC-7500 gamma camera.

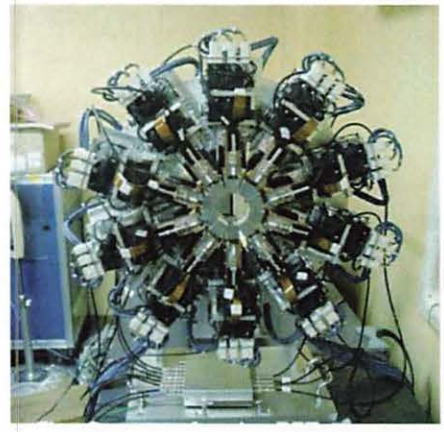

Figure 2. Ultra-high resolution semiconductos PET system.

V. PIXE AND ENVIRONMENTAL ANALYSIS

V. 1. Chemical State Analysis of Fe Compounds Using Heavy Ion PIXE

Matusyma S.[1], Ishii K.[1], Yamazaki H.[2], Kikuchi Y.[1], Kawamura Y.[1], Yamanaka K.[1], Tsuboi K.[1], and Watanabe M.[1]

[1]Department of Quantum Science and Energy Engineering, Tohoku University,
[2]Cyclotron and Radioisotope Center, Tohoku University

INTRODUCTION

Particle induced x-ray emission (PIXE) is a powerful means for quantitative analysis[1]. Proton beams with an energy around 3 MeV are usually used in PIXE. However, high sensitive measurement with chemical state is impossible by proton bombardment, because chemical shift is very small and difficult to measured with conventional Si(Li) detector. Since chemical change due to chemical state of the elements will be expanded due to multiple ionization, it may be measured with a conventional Si(Li) detector. In the last report, the three parameters, the relative change of an intensity ratio of k_β and k_α (intensity ratio), a ratio of k_β and k_α line width (line width ratio) and an energy difference between k_β and k_α line (relative energy shift) for iron, were measured using 70 MeV carbon ions and 78 MeV Ar ions. Changes in those parameters were corresponds to their chemical state of iron. It shows that PIXE with heavy ions will lead to chemical state analysis with high-sensitivity. In this study, we applied the method to the chemical state analysis of realistic iron samples. The chemical state of iron in steel will lead to the prediction of stress corrosion cracking.

EXPERIMENTAL

Experiment was carried out at Cyclotron Radioisotope Center. Samples are FeO, FeOOH, Fe_2O_3, Fe_3O_4 and these mixture. The targets were placed at an angle of 45° with respect to the beam direction to reduce X-ray absorption in the sample. X-rays emitted from the target were measured at an angle of 90° with respect to the beam direction, by a Si(Li) detector. 1 mm Mylar film was placed in front of the Si(Li) detector to reduce pile-

up events. The energy calibration was obtained with characteristic x-rays from a ^{241}Am source.

RESULTS

Typical relative change of an intensity ratio of k_β and k_α (Intensity Ratio), a ratio of k_β and k_α line width (line width ratio) and an energy difference between k_β and k_α line (relative energy shift) are shown in Fig. 1. As reported previously, the changes in intensity ratio are corresponding to the chemical states of the elements, while the other parameters are difficult to specify chemical state. The values of mixed sample of Fe_3O_4 and FeO are within the triangles of Fe_3O_4 and FeO as estimated. Since these measurements were carried out within a few minute, PIXE with heavy ions will lead to chemical state analysis with high-sensitivity.

ACKNOWLEDGEMENTS

The authors thank the working group of the Cyclotron Radioisotope Center, Tohoku University for the operation and maintenance of the accelerator.

References

1) Johansson S.A.E., Campbell J.L., PIXE A Novel Technique for Elemental Analysis, John Wiley & Sons Ltd. (1988) 32.
2) Ishii K., Orihara H,, Iwata Y., Bessho K., Int. J. PIXE 4 (1994) 1.
3) Amartaibvan Ts., Ishii K., Yamazaki H., Matsuyama S., Suzuki A., Yamaguchi T., Abe S., Inomata K., Watanabe Y., 823.1~3, http//pixe2004.ijs.si/, Proceedings of 10th international conference on PIXE and its applications, Portoroz, Slovenia, June 4-8, 2004.

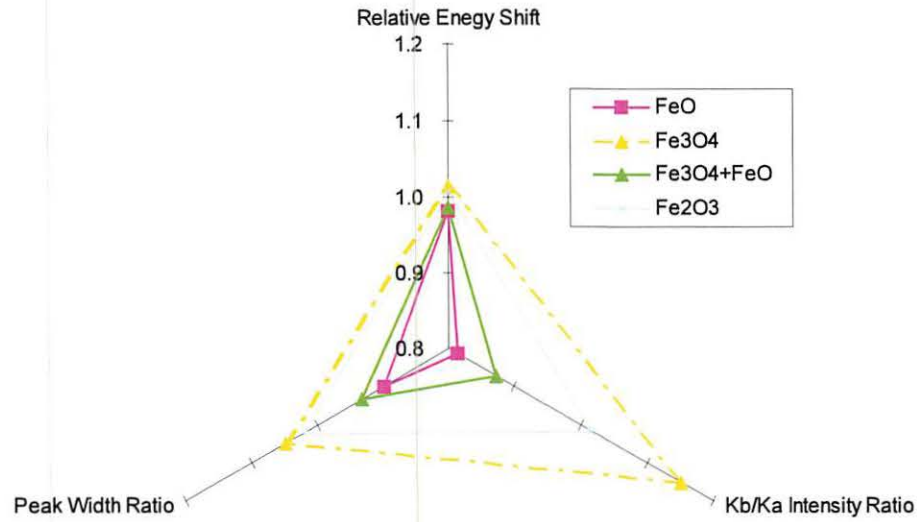

Figure 1. The relative change of an intensity ratio of k_β and k_α (Intensity Ratio), a ratio of k_β and k_α line width (line width ratio) and an energy difference between k_β and k_α line (relative energy shift) for FeO, Fe_3O_4, Fe_2O_3 and mixture of Fe_3O_4 and FeO.

V. 2. Analysis of Lacquerware Using In-air Submilli-PIXE Camera

Matsuyama S.[1], Ishii K.[1], Yamazaki H.[2], Kikuchi Y.[1], Oyama R.[1], Kawamura Y.[1], Ishizaki A.[1], Momose G.[1], Fujisawa A.[3], and Kyono K.[3]

[1]Department of Quantum Science and Energy Engineering, Tohoku University
[2]Cyclotron and Radioisotope Center, Tohoku University
[3]The Archeological Research Center on the Campus of Tohoku University

Introduction

Because lacquerware, pottery, and hardware excavated from historical places provide information related to the culture of that period, many studies have been carried out to investigate their shape and coloration using visual inspection. Recently, scientific studies of the materials of which the archeological objects are composed using various analytical techniques make it necessary to know their provenance, process, and period. Such analyses should be non-destructive, sensitive, and multi-elemental. Particle-induced X-ray emission (PIXE) fulfills these requirements and is suitable for this purpose[1)]. We developed an in-air submilli-PIXE camera which can measure spatial distribution images of element in the region of several square centimeters with submillimeter resolution. In a usual PIXE analysis, a beam spot size of a few millimeters is used. In this case, elements must be uniformly distributed in quantitative analysis. Therefore, samples are necessarily destroyed and prepared uniformly in quantitative analysis if elements are not distributed uniformly. The submilli-PIXE camera enables quantitative analysis without sample preparation. Furthermore, its high-speed beam scanning and in-air analysis enabled us to measure elemental images without degrading the feasible sample. We applied the submilli-PIXE camera to pigment analyses of lacquerware pieces excavated from the Edo-period stratum at the southern part of Kawauchi campus of Tohoku University. That area is located at the former secondary citadel area of Sendai's Aoba Castle. Elemental images of the decoration of lacquerware will be useful for elucidation of classical lacquer-working techniques.

Sample

The samples are lacquerware pieces excavated from the Edo-period stratum at the southern part Kawauchi campus of Tohoku University[1]. The campus is located at the former secondary citadel area of Sendai's Aoba Castle. The castle was constructed by Date Masamune (1567–1636), who governed the Tohoku district in northeastern Japan. The secondary citadel area was a residential area of his chief retainers. A large building was constructed there in the 17th century. The building was demolished and later reconstructed[2]. The obtained samples were wooden bowls and trays decorated with lacquer resin; they were excavated from two areas with four different strata (early 17th century, late 17th century, late 18th century and early 19th century). Lacquerware pieces analyzed in this study had been colored with black lacquer resin and decorated with red lacquer resin. They were kept in water after excavation.

Analysis

Analysis was carried out using an in-air submilli-PIXE camera. Technical details are described in previous papers[3,4]. Submilli-beams are formed using two slits with 1.5 m spacing and are extracted to the air through an exit window of 12.5 μm Kapton foil. A sample was set immediately in front of the exit window. X-rays from a sample are detected using a Si(Li) detector set at 135 deg with respect to the beam axis. The samples were kept in water to prevent their destruction by drying of the wooden part. In a previous study, lacquerware was analyzed without deterioration[4]. Therefore, prevention of drying during analysis is extremely important. Immediately after removing the sample from the water, the sample surface was wiped and analyzed. The Si(Li) detector with 80 cm^2 active area is used in this study to reduce the irradiation time. The samples were fixed directly to a target frame. Irradiation was carried out with 3 MeV proton beams: beam currents of 4–40 nA, total accumulated charges of 6–40 μC, with scanning area of 11 × 14 mm^2. Polypropylene of 10 μm thickness and Mylar of 100 μm thickness were set in front of the detector to reduce spectrum deformation by recoil protons. Generally, lacquerware is decorated with several lacquer layers, each of which is several tens to several hundreds of micrometers' thickness. Because the range of the 3 MeV protons in the lacquer resin is estimated as 100 μm, proton beams are stopped in the layer. For that reason, the change in the X-ray production cross section and X-ray attenuation in the sample must be considered in quantitative analyses. Quantitative PIXE analyses considering these effects were performed

using GeoPIXEII software[5]. In the calculation, the major composition and density of the layer must be set. The lacquer layer is presumed to be Urushiol ($C_{21}H_{32}O_2$) of 100 μm thickness, with a density of 1.25 g/cm^3 [6].

Results

Typical elemental images and photographs for NM5W070, NM9W001, NM9W002, NM9W053, and NM9W059 are shown in Figs. 1–5. The numerical value in the color bar shows the maximum weight percentage of a selected element. Sample NM5W070 was excavated from the late-17th century stratum. In NM5W070 (Fig. 1), the mercury distribution corresponds to the decoration painted in red color. In contrast, iron and calcium show a similar distribution and correspond to the black lacquer. It is estimated that the red decoration was painted using pigment of cinnabar (HgS). Samples NM9W001 through NM9W059 were excavated from a different place where NM5W070 was excavated. Both NM9W001 (Fig. 2) and NM9W002 (Fig. 3) were excavated from the early-17th century stratum. In both samples, mercury is distributed in the red decoration, although the iron distribution does not correspond to the decoration. These samples are also decorated with cinnabar pigment. Iron might have adhered to the sample during its burial in the soil. Although calcium shows an inverse distribution to mercury in NM9W001, calcium is distributed uniformly throughout NM9W002. Because the mercury concentration in NM9W001 is almost 10 times higher than that of NM9W002, the red painted layer in NM9W002 is thinner than that of NM9W001, or a clear lacquer resin is painted on the surface. Samples NM9W053 (Fig. 4) to NM9W059 (Fig. 5) were excavated from the late-18th century stratum. Iron and calcium are distributed inversely in the samples. The iron distribution corresponds to the region painted in red. It is apparent that the red pigment contained red iron oxide: Bengala. In NM9W059, the lacquer resin had been partly peeled off. Because the calcium concentration is lower than that of the lacquer resin, calcium is inferred to be contained in the lacquer resin. Elemental analysis using images is effective to discriminate contaminant elements through comparison with the decoration. Elemental concentrations of red lacquer resin obtained from the images are depicted in Figs. 6–8 with those of other samples (NM9W172 and NM9W177), which are not shown in Figs. 1–5. Calcium and iron concentrations are low in the area painted in cinnabar, except in NM9W002. The iron concentration in NM9W002 is almost the same as that painted in Bengala. Because the mercury concentration of NM9W002 is lower than that painted in

cinnabar, red pigment is estimated as a mixture of the pigments of cinnabar and Bengala. However, image analysis revealed that iron is merely a contaminant element. The calcium concentration of black lacquer resin is shown in Fig. 9. Because the NM5W044 sample was decorated only in silver, the elemental concentration is not presented in Figs. 6–8. Elemental concentrations of NM9W001 and NM9W002 are lower than those of the other samples. Two methods were typically used to make black lacquer resin. Classically, black lacquer was made by mixing charcoal into the lacquer. Later, it was made by mixing iron with lacquer during the purification process. The present results might reflect the black lacquer resin production process.

Conclusions

Lacquerware pieces excavated from the Edo-period stratum at the southern part of Kawauchi campus of Tohoku University were analyzed using the submilli-PIXE camera at Tohoku University. Feasible lacquerware pieces were analyzed without sample degradation and without sample preparation. Pigments used in the lacquer resin were determined easily. This analytical method, which uses images, was effective to discriminate contaminant elements through comparison with the decoration. PIXE analysis using the in-air submilli-PIXE camera is an effective tool for use in archeological studies.

Acknowledgements

The authors gratefully acknowledge the assistance of Mr. R. Sakamoto and M. Fujisawa for maintenance and operation of the Dynamitron accelerator. The authors also thank Mr. K. Komatsu, T. Nagaya, and C. Akama for assistance in constructing the submilli-PIXE camera.

References

1) Johansson S.A.E., Campbell J.L., PIXE: A Novel Technique for Elemental Analysis, JohnWiley and Sons, (1988).
2) Fujisawa A., "The History of Secondary Citadel Area of Sendai's Aoba Castle from the Viewpoint of Archeological Study", Annual Report of The Archeological Research Center on the Campus of Tohoku University, The Archeological Research Center on the Campus of Tohoku University **9** (1998) 93 (in Japanese).
3) Matsuyama S., Gotoh K., Ishii K., Yamazaki H., Satoh T., Yamamoto K., Sugimoto A., Tokai Y., Endoh H., Orihara H., "Development of a Submilli-PIXE Camera", Int. J. of PIXE, **8** (1998) 209.
4) Matsuyama S., Ishii K., Yamazaki H., Endoh H, Gotoh K., Satoh T., Yamamoto K., Sugimoto A., Tokai Y., Orihara H., Yokota S., Fujisawa A., Sekine T., Nara Y., Chiba N., Sutoh T., "No Deterioration Elemental Analysis with In-Air Submilli-PIXE Camara", Int. J. PIXE, **9** (1999) 57.

5) Ryan C.G., Van Achterbergh E., Yeats C.J., Drieberg S.L., Mark G., McInnes B.M., Win T.T., Cripps G., Suter G.F., "Quantitative, high sensivity, high resolution, nuclear microprobe imaging of fluids, melts and minerals", Nucl. Instr. and Meth. **B188** (2002) 18.
6) Nagase K., Book of Urushi, Kenkyu-Sya (1986) (in Japanese).

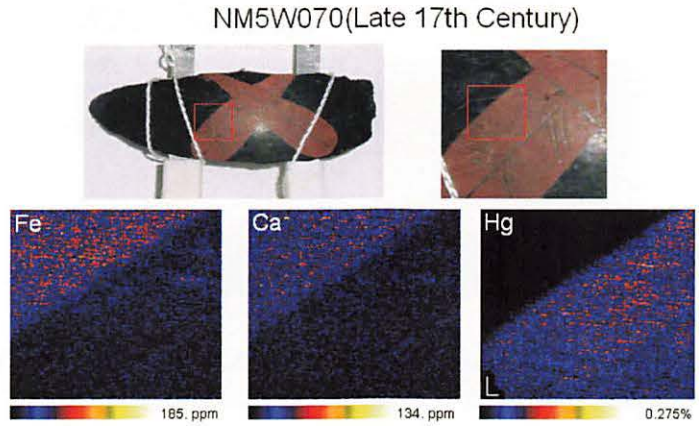

Figure 1. Elemental Images and Photographs for NM5W070 (Late 17th Century).

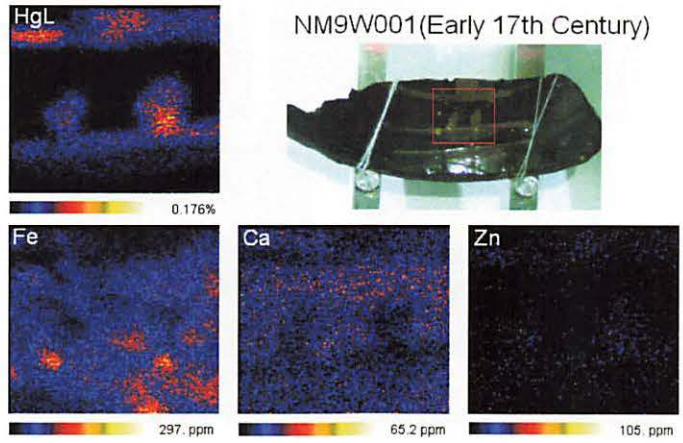

Figure 2. Elemental Images and Photographs for NM9W001 (Early 17th Century).

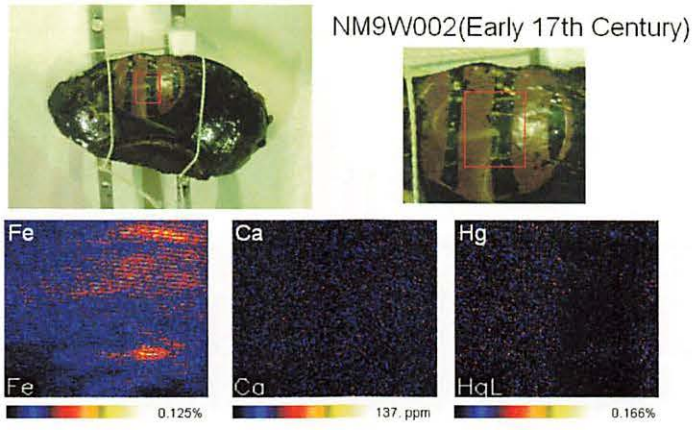

Figure 3. Elemental Images and Photographs for NM9W002 (Early 17th Century).

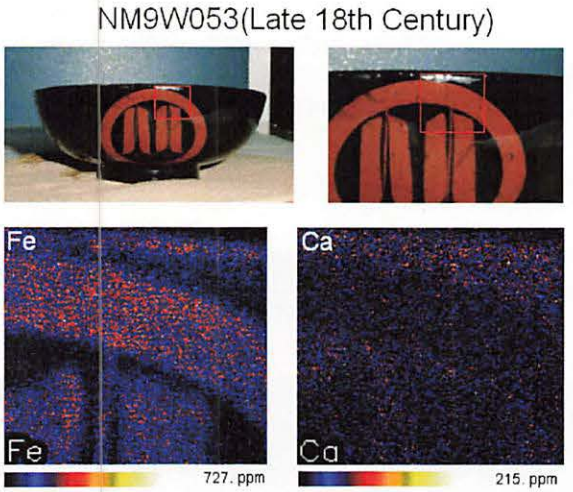

Figure 4. Elemental Images and Photographs for NM9W053 (Late 18th Century).

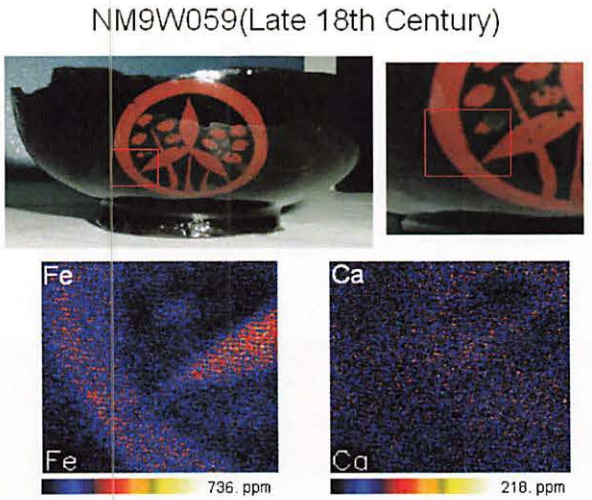

Figure 5. Elemental Images and Photographs for NM9W059 (Late 18th Century).

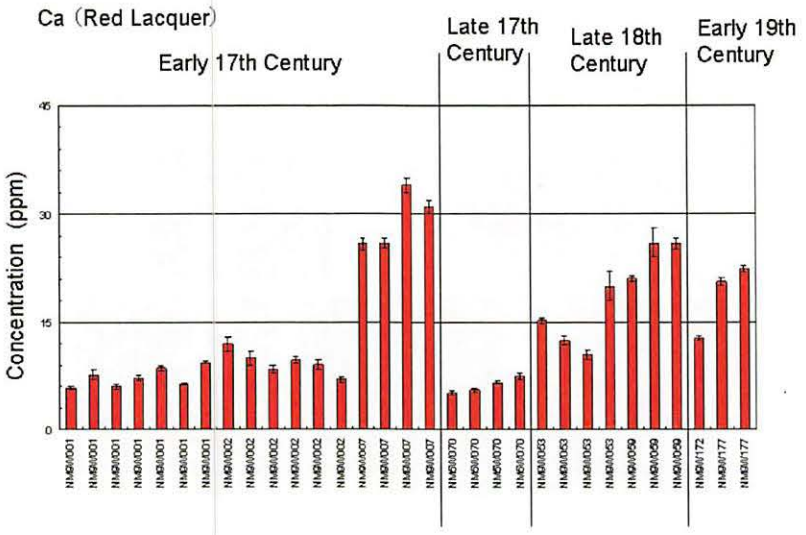

Figure 6. Elemental Concentrations of Red Lacquer Resin (Ca).

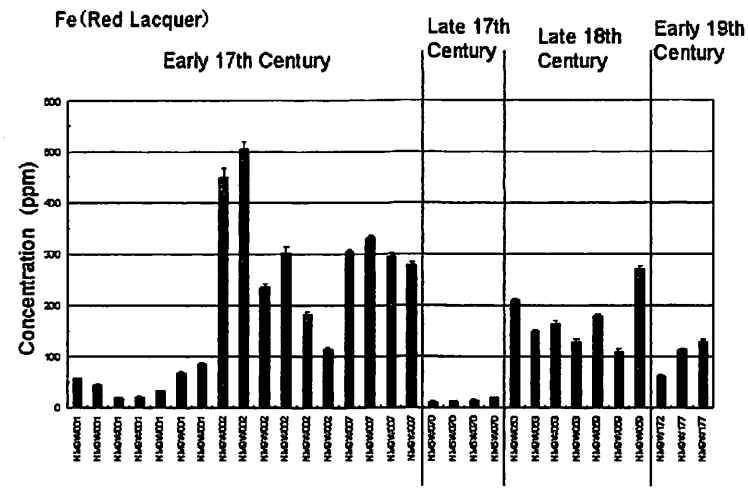

Figure 7. Elemental Concentrations of Red Lacquer Resin (Fe).

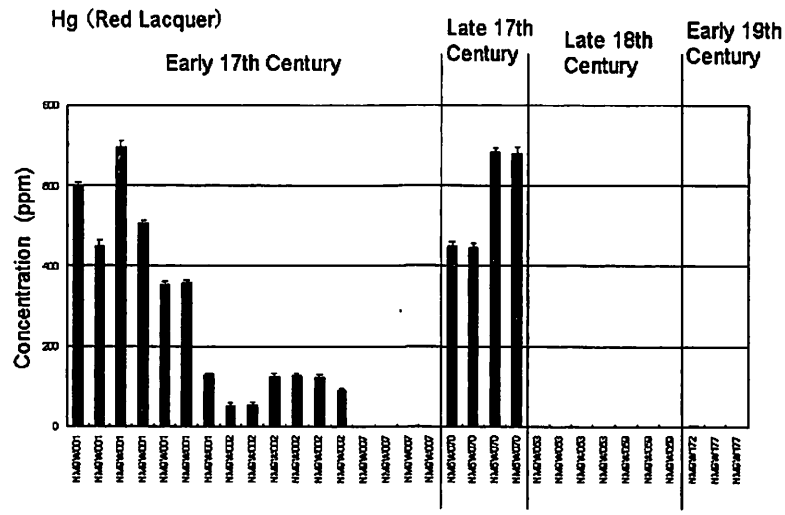

Figure 8. Elemental Concentrations of Red Lacquer Resin (Hg).

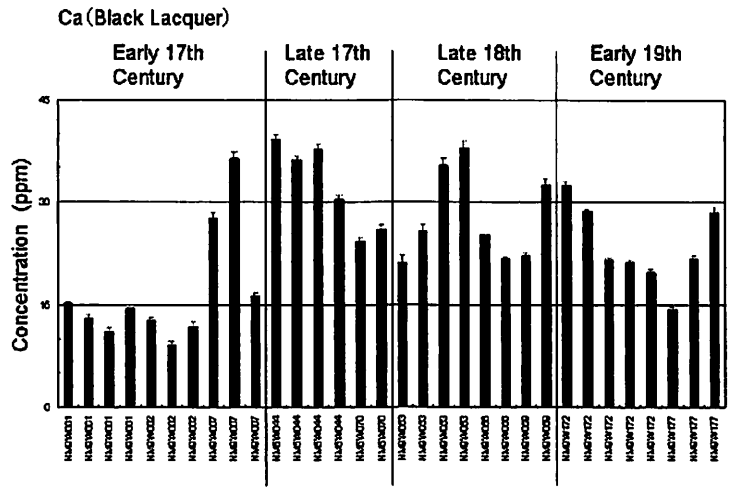

Figure 9. Elemental Concentrations of Black Lacquer Resin (Ca).

V. 3. Development of Microbeam Scanning System

Oyama R.[1], Matsuyama S.[1], Ishii K.[1], Yamazaki H.[2], Kikuchi Y.[1], Inomata K.[1], Watanabe Y.[1], Ishizaki A.[1], Kawamura Y.[1], Yamaguchi.[1], and Momose G.[1]

[1]Department of Quantum Science and Energy Engineering, Tohoku University,
[2]Cyclotron and Radioisotope Center, Tohoku University

Introduction

High-energy ion microbeams are powerful analytical tools when used in combination with various ion beam analysis techniques; they are also attractive as a direct micro fabrication technique[1-3]. We have developed a microbeam scanning system that is suitable for these purposes. In microbeam analysis systems, microbeams are scanned over a square region of sample. However, analysis samples, such as cultured single cells or collected aerosol particles are not always distributed all over. In such cases, irradiation on areas where specimens are not distributed merely prolongs the analysis time. In micro fabrication, such as proton beam writing (PBW), the situation is rather essential. Microbeams are scanned on the sample and are kicked away where irradiation is not needed. Irradiation time would be shortened if microbeams were scanned with a pattern corresponding to the sample area or processing pattern. As described herein, we developed a microbeam scanning system that is suitable for efficient analysis and for micro fabrication such as PBW.

Beam scanning system

The microbeam system was designed and then developed to achieve sub-micrometer beam sizes[4-7]. The microbeam system comprises a quadrupole doublet and three slit systems. The scanner is located ca. 8 cm downstream of the quadrupole doublet. The scanning system comprises a set of electrostatic deflectors, high-voltage (HV) amplifiers, buffer amplifiers, and a function generator. A schematic diagram of the scanning system and data acquisition system is shown in Fig. 1. The data acquisition system of multimodal analysis was described precisely in previous papers[1].

The electrostatic deflector was 25 mm long and 16 mm wide, with 3 mm spacing. Both ends of the deflector plate along the longitudinal direction, the beam direction, have steps of 0.5 mm to reduce the fringing field effect. Each deflector was driven by an independent HV amplifier to obtain a uniform and symmetric electrostatic field. In total four HV amplifiers were used in the system for horizontal and vertical scanning. In the original design, the deflector was 25 mm long and 16 mm wide, with 5 mm spacing and without steps at both ends. One of the deflector plates was driven by an HV amplifier and the other deflector plate was grounded. Two amplifiers were used for horizontal and vertical scanning, respectively.

Figure 2 shows elemental images of Cu mesh (100 lines/inch) for a scanning area of 350×450 μm^2 measured with the two HV amplifier system (left) and with the four HV amplifier system (right). Both images were obtained in the same beam condition with the same deflectors of 25 mm long and 16 mm wide, with 5 mm spacing. The mesh image obtained by using the two amplifier system is not clearly seen in the upper left and the lower right regions. On the other hand, using the four amplifier system, the image is clearly seen over the scanning area. Thus, the four HV amplifier system is indispensable to obtain the same beam spot size at any scanning position.

Figure 3 shows the mesh images obtained with the no step deflectors (left) and with the stepped deflectors (right), respectively. These deflectors were driven by the four HV amplifiers. The images were compared for elemental images of Au and Ni mesh (2000 lines/inch), respectively, with five scanning areas of 30×30 μm^2 at the center position, and at the four corners of the 600×600 μm square. Beam conditions are almost same in both measurements. The images obtained using the no step deflectors are deformed at the corners of the 600×600 μm square, especially at the upper left and the lower right areas. On the other hand, the images measured with the stepped deflectors show the same quality with no deformation at any position. Therefore, the four HV amplifier system and deflector shape which reduces the fringing field effect are indispensable to keep the beam spot size at any scanning position.

The HV amplifier (HOPS1.5B2; Matsusada Precision Inc.) is a fast response HV bipolar amplifier with a slew rate of 12 V/μs. The maximum voltage is 1.5 kV. Therefore, the obtained electrostatic field of 1 kV/mm is sufficient to shift the 3 MeV proton beam to more than 0.5 mm on the target position. The amplifier amplifies a -10 to 10 V signal into a -1.5 to +1.5 kV signal. A four-channel function generator of a PC-based measurement

instrument (WE-7282; Yokogawa Electric Corp.) is used for X-Y beam scanning and for elemental imaging. Two channels out of four were used as scanning signals to drive the HV amplifiers for the scanners. Other two are used as X-Y position signals corresponding to the beam scanning. Each beam scanning signal is divided into two signals and is introduced into the buffer amplifier. One is inverted; the other is not inverted. While raster scanning is utilized in the conventional analysis, the beam can be scanned according to an arbitrary pattern. Varying the irradiation time alters the irradiation dose. The function generator can output 10^6 points of DC voltage sequentially even in the minimum time scale of 10 μs/point, so as to generate complicated voltage patterns in a short period. Thus the microbeams can be just scanned with a corresponding pattern of the analyzing sample area or of the fabrication form. Between the patterns, the beams are moved with the fastest responsive scan speed. We call the process as the pattern-to-pattern spacing procedure.

The scanning speed is also an important factor. The beam scanning speed must be high to keep correct irradiation dose on the pattern and to reduce the irradiation dose between pattern-to-pattern spacing. Measurements of the beam scanning speed versus the beam spot size were carried out by scanning the beam one-dimensionally on the Ni mesh (2000 lines/inch). The beam was scanned on a line of 150 μm length with the scanning speeds ranging from 0.3 to 60 mm/s. The X-ray yield profile was fitted using symmetric double-Gaussian convolution and the beam spot size was obtained. The yield profiles at scanning speeds of less than 9 mm/s show a similar shape, although they are deformed and finally split into two peaks at the speed of 60 mm/s, especially on both sides. This is due to deformation of the output of the HV amplifier at the tops and bottoms of the triangular waveform, that is, the HV amplifier is unresponsive to sudden changes of voltage and thus, waveform was deformed. Therefore, the maximum scanning speed can be estimated at 9 mm/s to keep correct irradiation dose on the irradiation pattern.

Application to the microbeam analyses

Microbeam analysis samples, such as cultured single cells or collected aerosol particles are not always distributed all over. Figure 4 shows a microphotograph of cells cultured on the polycarbonate film. In this case, cells occupy only half of the scanning area. The analysis time is reduced greatly if the beams are scanned only on the cells. In order to define the regions of the cells, scanning transmission ion microscopy (STIM)

mapping was used. This is very useful to achieve structural and density imaging for the scanning area in a short period, because in STIM, transmitted ions are detected with almost 100 % efficiency[1]. Figure 5 shows a STIM map of the cells according to the area shown in Fig. 4. Cells are clearly apparent in the map and correspond to the microphotograph. While application of optical images obtained using a microscope is also applicable for this system, position calibration is not easy. In case of STIM imaging, position calibration is not needed. The scanning pattern, which corresponded to the areas of the cells, was translated from the STIM map. Transmitted ion energies vary corresponding to the cell thickness. Therefore, appropriate transmitted ion energy range has to be selected to define the areas of the cells properly. To cover all the cell areas, transmitted ion energy range was selected widely considering the energy resolution of the charged particle detector. Using the STIM-based scanning pattern, microbeams can be made to irradiate only the cells. In order to check the scanning pattern and the dose in the irradiation area, before cell analysis using the STIM-based scanning pattern, titanium foil of 0.2 μm thick was irradiated with this pattern and an X-ray yield map was obtained. The X-ray map is shown in Fig. 6 along with the irradiation pattern obtained from the STIM map and with the relative X-ray yield per square micrometer in the indicated areas. Total irradiation points were 263,168 points; 263 s are required for one scan. The scan was repeated until an X-ray yield reached a predetermined yield. The beams were scanned with the settled pattern as shown in fig 6. The X-ray yield is constant, as shown in Fig. 6. Fluctuation of the beam current was averaged by repeated beam scanning.

Then the cells were analyzed using the STIM-based scanning and with the conventional raster scanning. Figure 7 shows elemental concentration maps of cells with the STIM-based scanning and the conventional scanning. The total accumulated charges were around 170 nC for both measurements. X-rays were detected only from the settled patterns. However, in the space between the cells, there are fractions of patterns, and X-rays were partly detected. Since the range of the transmitted ion energy was set widely to cover all the cell area, some of the areas where cells were not distributed was recognized as the areas of cells and were irradiated.

Elemental concentrations in the cell derived from these scanning methods mutually coincide within statistical error. Statistical errors in the STIM-based scanning are better than those in the raster scanning in the cell regions because STIM-based scanning increases the irradiation dose in the cell area. In case of the same statistical error, the irradiation

time is reducible to 1/2.5 with the same statistical error. Consequently, the STIM-based scanning system reduces the necessary analysis time, as shown in the actual sample analysis.

Application to proton beam writing

Proton beam writing was achieved by scanning the microbeam with a corresponding scanning pattern translated from a bitmap file. The irradiation dose corresponds to the color and is changed by varying the irradiation time. Several patterns translated from bitmap files were inscribed on Mylar and polyester films to demonstrate the performance of the scanning system. The thickness of the Mylar and polyester films were 100 and 100 μm, respectively. RBS analysis was performed to monitor the irradiation dose. After the irradiation of the Mylar film, direct STIM analysis was carried out. Figure 8 shows a microphotograph, an RBS map, and direct STIM images of a Mylar film after irradiation with a scanning pattern of Chinese characters: 小山 亮平. The irradiation pattern is clearly apparent both on the microphotograph and on the direct STIM image. The RBS image also shows that irradiation was made solely on the character. The beam spot sizes of 0.7×0.9 μm^2 with a beam current of 50 pA is used in this irradiation. The total accumulated charge was 260 nC. Figure 9 shows STIM spectra for i (irradiation area), ii (space between irradiation area), and iii (non-irradiation area). In region i, the elemental loss occurred and the transmitted energy was increased. In the regions of ii and iii, no difference was found. Irradiation damage was not measurable in the space between irradiation areas; for that reason, the fast beam skip is useful for PBW. A design of a Japanese classical toy was inscribed on a polyester film of 100 μm. A micrograph and RBS map are shown in Fig. 10. The irradiation was made using a beam spot size of 1.0×1.5 μm^2 with a beam current of 300 pA. This design was inscribed with two tones and is shown in the RBS map. The lower irradiation dose was 40 pC/μm^2; the higher one was 200 pC/μm^2. Red coloration corresponding to the irradiation dose was clearly apparent. A red shift occurred in the irradiation area[1].

Conclusions

We developed a new microbeam scanning system that is suitable for microbeam analyses and PBW. The system accomplished a pattern-to-pattern spacing procedure, in which the microbeam was just scanned with a corresponding pattern of the analyzing

sample area or of the fabrication form. Between the patterns, the beam was moved with the fastest responsive scanning speed. For efficient analysis, a STIM image was translated into a scanning pattern. As the result, analyzing time was greatly reduced for the cell sample in which cells are not distributed all over. The scanning system was also applied to PBW. Where a pattern was translated from bitmap data including color scale, which was translated to the irradiation time in proportion to the irradiation dose. Several patterns were inscribed on thin polymer foils as demonstrations. The scanning system will be useful for efficient analysis and PBW.

Acknowledgements

This study was partly supported by Grants-in-Aid for Scientific Research (S) from the Ministry of Education, Culture, Sports, Science and Technology, Japan: No. 13852017, (B) No. 18360450, and (C) No. 16560731. The authors gratefully acknowledge the assistance of R. Sakamoto and M. Fujisawa for maintenance and operation of the Dynamitron accelerator. The authors would also like to thank Messrs. K. Komatsu, T. Nagaya and C. Akama for their assistance in constructing the microbeam system.

References

1) Watt F., Grime G.W., Principal and Applications of High-energy Ion Microbeams, Adam Hilger, Bristol, 1987.
2) Johansson S.A.E., Campbell J.L., Malmqvist K.G., Particle-Induced X-ray Emission Spectrometry (PIXE), John Wiley and Sons, N.Y., 1995.
3) Breese M.B.H., Jamieson D.N., King P.J.C., Materials Analysis using Nuclear Microprobe, John Wiley and Sons, N.Y., 1995.
4) Matsuyama S., Ishii K., Yamazaki H., Sakamoto R., Fujisawa M., Amartaivan Ts., Ohishi Y., M Rodriguez., Suzuki A., Kamiya T., Oikawa M., Arakawa K., Matsumoto N., Nucl. Instr. Meth., **B210** (2003) 59.
5) Matsuyama S., Ishii K., Yamazaki H., Y Barbotteau., Amartivan Ts., Izukawa D., Hotta K., Mizuma K., Abe S., Oishi Y., M Rodriguez., Suzuki A., Sakamoto R., Fujisawa M., Kamiya T., Oikawa M., Arakawa K., Imaseki H., Matsumoto N., Int. J. PIXE, **14** (2004) 1.
6) Matsuyama S., Ishii K., Yamazaki H., Kikuchi Y., Inomata K., Watanabe Y., Ishizaki A., Oyama R., Kawamura Y., Yamaguchi T., Momose G., Nagakura M., Takahashi M., Kamiya T., Nucl. Instr. Meth. **B260** (2007) 55.
7) Matsuyama S., Ishii K., Yamazaki H., Kikuchi Y., Amartivan Ts., Abe S., Inomata K., Watanabe, A.Ishizaki Y., Oyama R., Kawamura Y., Suzuki A., Momose G., Yamaguchi T., Imaseki H., Int. J. PIXE, **15** (2005) 257.
8) Matsuyama S., Ishii K., Sugimoto A., Satoh T., Gotoh K., Yamazaki H., Iwasaki S., Murozono K., Inoue J., Hamano T., Yokota S., Sakai T., Kamiya T., Tanaka R., Int. J. PIXE, **8** (1998) 203.
9) Inomata K., Ishii K., Yamazaki H., Matsuyama S., Kikuchi Y., Watanabe Y., Ishizaki A., Oyama R., Kawamura Y., Yamaguchi T., Momose G., Sakurai E., Yanai K., Kamiya T., Sakai T., Satoh T., Oikawa M., Arakawa K., Int. J. PIXE, **16** (2006) 149.
10) Matsuyama S., Ishii K., Yamazaki H., Endoh H., Yuki H., Sato T., Sugihara S., Amartaivan Ts., Tanaka A., Komori H., Orihara H., Int. J. PIXE, **11** (2001) 93.

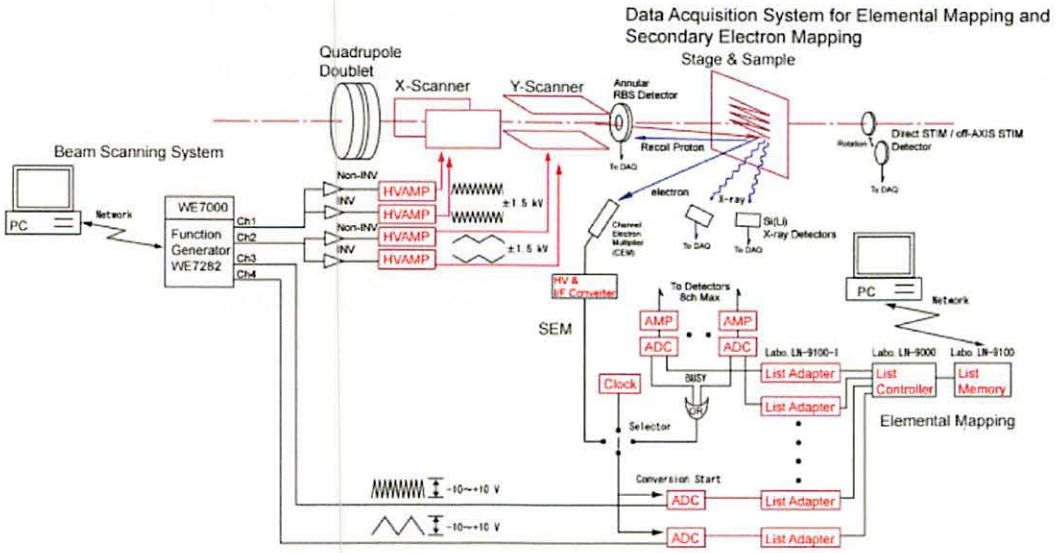

Figure 1. Schematic diagram of the beam scanning system and data acquisition system.

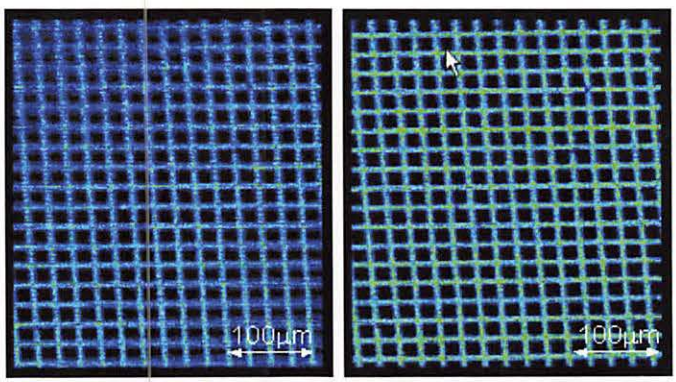

Figure 2. Elemental images of Cu mesh (1000 lines/inch) for a scanning area of 350 ×450 μm with the two HV amplifier system(left) and with the four amplifier system.

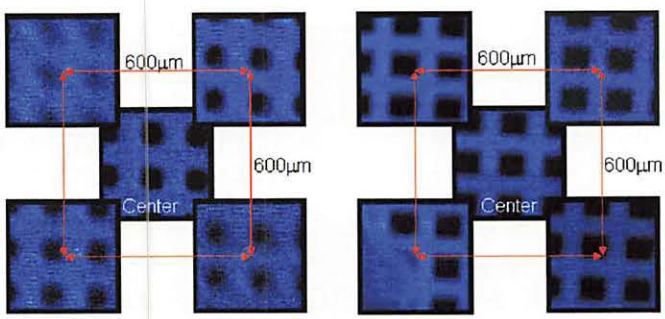

Figure 3. Elemental images of Au (left) and Ni (right) mesh (2000 lines/inch) with five scanning areas of 30×30 μm^2 at the center position, and at the four corners of the 600×600 μm square measured with the no step deflectors (left) and the stepped deflectors (right).

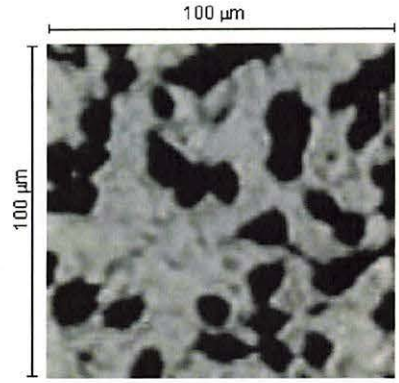

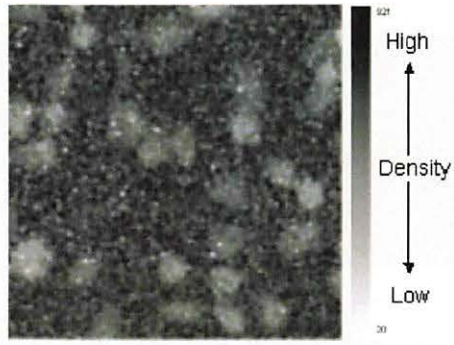

Figure 4. Microphotograph of Cultured Cells. Figure 5. STIM Map of Cultured Cells.

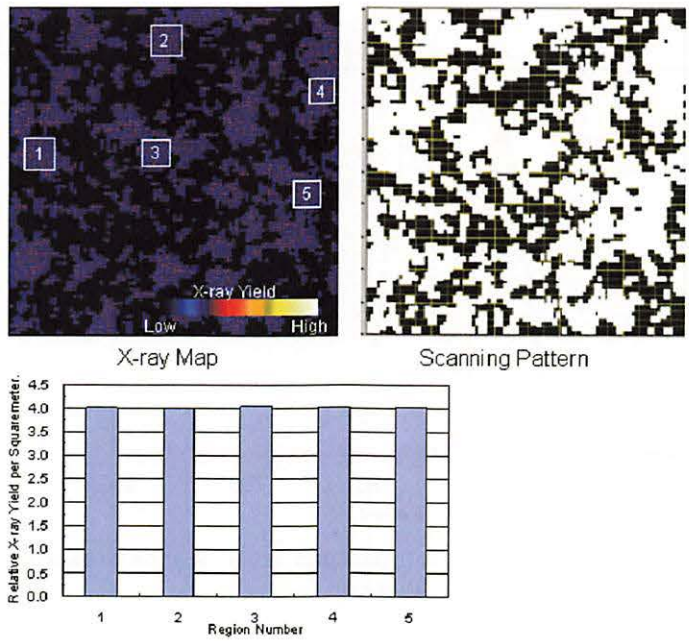

Figure 6. X-ray yield from titanium foil with STIM-based scanning, irradiation pattern and X-ray yields from the indicated areas.

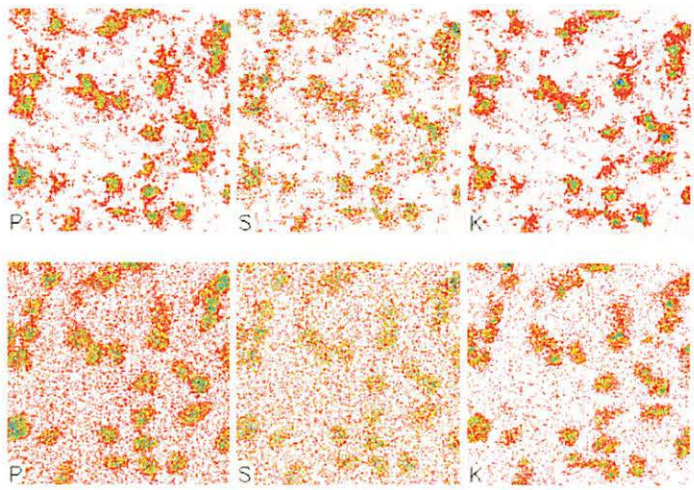

Figure 7. Elemental concentration maps of cells with the STIM-based scanning (upper) and conventional scanning (lower).

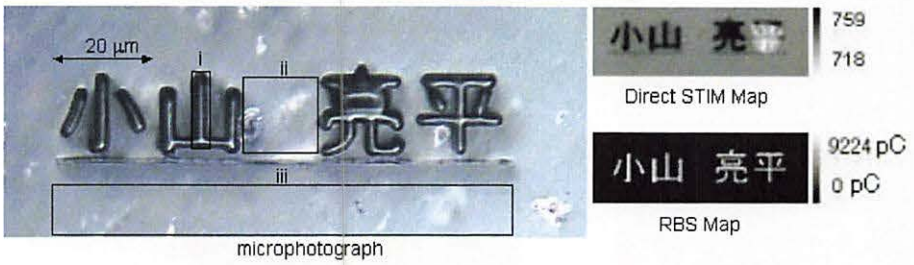

Figure 8. Microphotograph, RBS Map, and Direct STIM Images of a Mylar film after Irradiation with a Scanning Pattern of Chinese Characters: 小山 亮平.

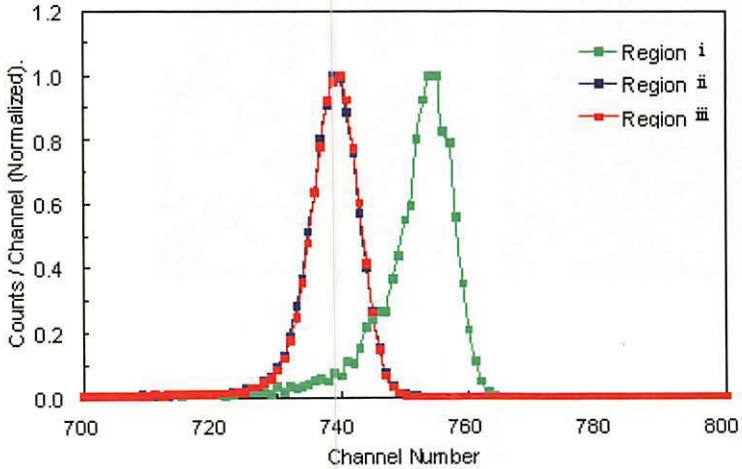

Figure 9. STIM spectra for Regions i (irradiation area), ii (space between irradiation area), and iii (non-irradiation area) in Fig. 7.

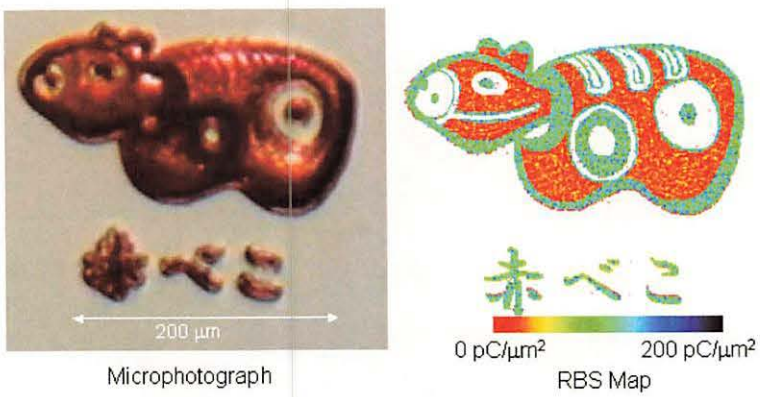

Figure 10. Design of a Japanese Classical Toy Inscribed on the Polyester Film and RBS.

V. 4. Elemental Mapping of an Arsenic Hyperaccumulator Fern Using Submilli-PIXE Camera

Yamazaki H.[1], Ishii K.[2], Matsuyama S.[2], Kikuchi Y.[2], Takahashi Y.[2], Kawamura Y.[2], Tashiro K.[3], and Inoue C.[3]

[1]Cyclotoron and Radioisotope Center, Tohoku University
[2]Graduate School of Engineering, Tohoku University
[3]Graduate School of Environmental Studies, Tohoku University

Introduction

Arsenic contamination of soils and groundwater from various sources such as mine and urban wastes, wood preservatives and pesticides is of great environmental problem. A number of technologies for remediation of soils contaminated by toxic elements have been developed. Most of these technologies, however, are expensive, and they occasionally produce secondary wastes[1]. Recently, environmentally friendly, low-input approaches such as phytoremediation have been proposed to clean up soils contaminated with heavy metals and metalloids[2]. Phytoremediation using an arsenic hyper-accumulator, *Pteris vittata* L., has generated increasing interest worldwide, for its both environmentally sound and cost effectiveness[3,4]. However, the mechanisms of arsenic uptake and accumulation by this plant are not clear at this time. To develop practical applications of this technology, it is necessary to explicate effective accumulation mechanisms for toxic elements.

The purpose of this work is to obtain fundamental information on a mechanism of arsenic accumulation in *Pteris vittata,* expected to be an arsenic hyper-acccumulator plant, in an *in-vivo* investigation by using a submilli-PIXE camera settled at Dynamitron laboratory of Tohoku University[5].

Material and methods

P. vittata L. was grown on the soil contaminated with arsenic used as a raw material of agricultural chemicals for 3 months in a growth chamber with a 16 hours light period, 25°C/20°C day/night temperature and 70% relative humidity. The concentration of arsenic was analyzed 600 mg per kg of soil dried at 105°C using a sequential extraction procedure

(following the Standard Measurement and Testing Program of the European Community), which identified the following fractions: 1) water soluble, exchangeable and carbonate bound; 2) Fe-Mn oxidize bound; 3) organic matter and sulfide bound[6,7]. A part of lamia of *P. vittata* was plucked at three different growth stages; an active growth stage, a mature stage without arsenic harm and the eldest stage with discoloration by arsenic harm. In the arsenate and arsenite uptake experiments, fern seedlings, 3 months after spore germination, were cultivated for 1 week in a hydroponic medium containing nutrient solution, and each seedling was placed in 100 ml conical beaker filled with 100 ml uptake solution. Then, arsenic in the form of either As(V) as sodium arsenate or As(III) as sodium arsenite was added to the uptake solution to be final concentration of 50 mg-As per litter of fresh nutrient solution with or without phosphate ions. The seedlings treated were incubated in the growth chamber under the same condition as above mentioned for 6-168 hours.

The submilli-PIXE camera provides spatial distribution images of elements in a region of 3×3 cm^2 with a resolution of around 0.5 mm. 3 MeV proton beam (~1 nA beam current, <0.5 mm beam diameter) from a 4.5-MV single-ended Dynamitron accelerator was extracted to open air through a thin polyimid (Kapton) film of 12.5 μm thickness (Fig. 1). The X-ray energy and the beam position were simultaneously measured in order to obtain spatial distribution of elements. The list mode data acquisition system can sort the data for a selected element / energy region and generate an elemental image even while the data are accumulated[5]. X-rays from a specimen are detected with two Si(Li) detectors; No.1 detector (7.5 μm thick Be window, 10 mm^2 active area) with a low geometric efficiency is well suited for detection of an element of low atomic number, and No.2 detector (12.5 μm thick Be window, 60 mm^2 active area) with a 300-μm Mylar absorber allows detection of X rays>4 keV and the removal of recoil protons. This resulted in a decrease of the dead time of signal processing and pile-up. Quantitative PIXE analysis was performed using the GeoPIXEII software[8].

Results and discussion

Pteris. vittata L., a kind of fern, has been found as an arsenic hyper accumulator plant. It is assumed that arsenate taken up by the roots is converted to arsenite before or after it is translocated to the fronds. It is also speculated that the phosphate transporting protein in the fern has a responsibility for the arsenic influx. However, the entry system of arsenic to this fern and the mechanism of translocation to the fronds are not studied well.

Figure 2 shows the elemental distributions in laminas of *P. vittata* at three growth stages. The numerical value in the color bar shows the maximum weight percent of a selected element in the plant of which composition is assumed to be 80% H_2O + 20% $C_4H_6O_3$. In the case of *P. vittata* at the eldest stage with arsenic harm, arsenic and essential elements of plants such as potassium and calcium are detected in a similar concentration level. However, arsenic concentrated especially to near edge of the fronds which corresponds to the discoloration part of the fronds, and arsenic occurs at a low level in the vein. Calcium is uniformly distributed in both the vein and the fronds, but potassium disappears to some extent from the withering part of the fronds with arsenic accumulation, indicating the death of a portion of frond cells. In the case of younger *P. vittata* laminas, these elements are distributed rather uniformly in a whole part of the lamina including the vein, excluding that arsenic and potassium concentrate in some degree into the tip of the fronds at the youngest stage. PIXE analysis showed the change of arsenic concentration (mg-As per kg frond (wet weight)) in the fern fronds at different growth stages: 1800-2600 mg-As per kg at the youngest stage, 460-840 mg-As per kg at a mature stage without arsenic harm, and 1500-3500 mg-As per kg at the eldest stage with arsenic withering.

These results indicate that arsenic absorbed from a contaminated soil is almost totally translocated to the fronds in youth and the concentration decreases while the fronds grow up, and in the final phase of the growth of fronds arsenic is concentrated again in the edge of fronds until withered. So, we can speculate that *P. vittata* acquires tolerance for arsenic by accumulating it in the edge of the fronds in stead of redistributing arsenic in the laminas without arsenic accumulation. For the eldest growth stage of *P. vittata*, the fronds grow thick, and the arsenic concentration is much higher than the contaminated level of 600 mg-As per kg for the soil used in cultivating the fern plants. When *P. vittata* plants are cultivated enough and then reaped together, the plants can be potentially used for cleanup of soil that is contaminated by arsenic originated from agricultural chemicals or drain of factories and smelting works.

In conclusion, the cm-scale area mapping of elements by the subumilli-PIXE camera reveals arsenic redistribution in the fronds of *P. vittata* at different growth stages. Therefore, PIXE analysis by the subumilli-PIXE camera is an effective tool for undertaking phytoremediation research to decide a reaping time and a reaped part of an arsenic hyper-accumulator plant, because it enables to detail arsenic location in a living plant without laborious pretreatments.

References

1) Lombi E., Zhao F.J., et al., New Phytologist. **156** (2003) 195.
2) McGrath S.P., Zhao F.J., Lombi E., Advances in Agronomy **75** (2002) 1.
3) Ma L.Q., Komar K.M., et al., Nature **409** (2001) 579.
4) Poynton C.Y., Huang J.W., et al., Planta **219** (2004) 1080.
5) Matsuyama S., Gotoh K., Ishii K., et al., Int. J. PIXE **8** (1998) 209.
6) Ure A.M., Quevauviller ph., et al., Int. J. Environ. Anal. Chem. **51** (1993) 135.
7) Wang Z., Shan X. Q., Zhang S., Chemosphere. **46** (2002) 1163.
8) Ryan C.G., Van Achterbergh E., et al., Nucl. Istr. Meth. **B188** (2002) 18.

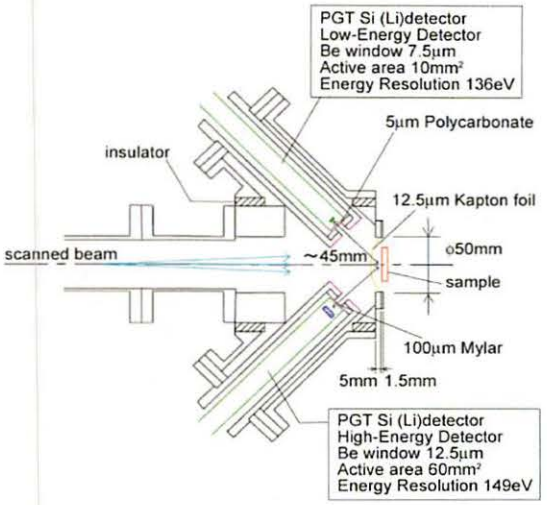

Figure 1. Cross section view of beam exit assembly.

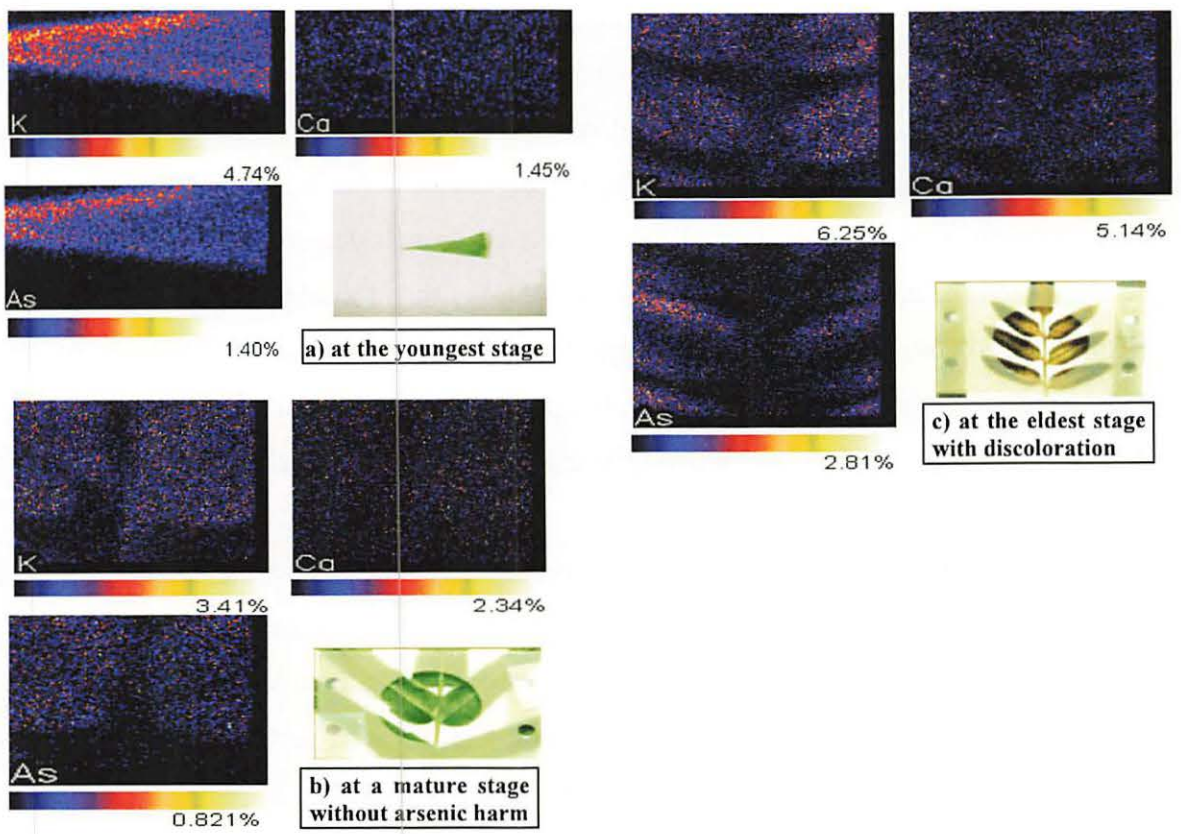

Figure 2. Photograph and elemental maps of lamias of *P. vittata* at three growth stages.

VI. RADIOCHEMISRTY AND NUCLEAR CHEMISTRY

VI. 1. Half-life Measurement of ^{7}Be in Different Chemical and Physical Environments

Ohtsuki T., Kasagi J., and Hirose K.

Laboratory of Nuclear Science, Tohoku University,

As first suggested by Segr'e et al.[1], the electron-capture (EC) decay rate depends on the density of atomic electrons within the nucleus. Environmental factors such as chemical forms and pressure etc. may alter the electron contact densities in the nucleus and thus affect the electron-capture decay rates. The nucleus of ^{7}Be is a good candidate in which to look for such variations in environmental factors because of its simple electronic structure, $1s^2 2s^2$, in the EC decay nucleus. The ^{7}Be decays directly to a $3/2^-$ ground state of ^{7}Li with a branching of 89.6%, it goes with a branching of 10.4% to a first excited state of ^{7}Li($1/2^-$ at 478 keV), which decays by γ emission to the ground state. In experiments to determine the decay rate of ^{7}Be in various environments, different chemical forms and/or host materials have been investigated by several groups. Differences found in the decay rate of ^{7}Be as a function of different chemical forms, host materials and under high pressure had been limited almost to within 0.2%. In recent studies, however, large variations have been observed as a function of different chemical forms and pressure etc[2,3]. Therefore, a precise measurement is still needed to obtain the absolute decay rate. So far, the success of the ^{7}Be endohedral C_{70}(^{7}Be@C_{70}) has allowed us to measure the half-life of ^{7}Be inside C_{60} and C_{70}[4,5]. Then, we have measured the half-life of ^{7}Be in the sample of ^{7}Be@C_{70} by using a reference method.

To produce the source of ^{7}Be, Li_2CO_3 was used in powder form. The grain size of the materials was smaller than 100 meshes (20 μm). Purified fullerene (C_{70}) was carefully mixed with each material (weight ratio=1:1) in an agate mortar, adding a few ml of carbon disulfide (CS_2). After drying up, about 100 mg of the mixture sample was wrapped in a pure aluminum foil of 10 μm in thickness for irradiation. Irradiation with 16 MeV protons was performed at the Cyclotron and Radioisotope Center, Tohoku University.

The beam current was typically 2.5 μA and the irradiation time was about 24 hours. The ^{7}Be can be produced in the ^{7}Li(p,n) reaction. The irradiated sample was dissolved in o-dichlorobenzene and filtered through a Millipore filter (pore size=0.2 μm) to remove insoluble materials. The soluble portion was injected into a HPLC device equipped with a 5PBB (Cosmosil) at a flow rate of 3 ml/min. For confirmation of fullerenes and their derivatives, a UV detector was installed with a wavelength of 290 nm. In order to measure the γ-rays emanating from ^{7}Be, eluent fractions were collected for 30 sec intervals. The ^{7}Be@C_{70} portion was checked with 478 keV γ-ray by a HPGe-detector. After confirmation of the existence of ^{7}Be@C_{70}, the sample was dried and pressed to use a measurement sample.

In order to measure the half-life at T=293K and 5K, the ^{7}Be@C_{70} sample was placed in the top of a sample holder and a He closed-cycle cryostat, respectively. Here, the two samples, ^{7}Be@C_{70} (fastened in sample holder (293K) or the cryostat (5K)) and Be metal (^{7}Be) (293K), were placed in a computer-controlled sample changer, which precisely moved the samples in front of a γ-ray detector. The measurement was started after the ^{7}Be@C_{70} sample underwent sufficient cooling at T=5K under vacuum. This arrangement allowed the decay rates of the two samples to be measured in a consistent fashion while reducing systematic errors. In the system, the internal clock time of the computer for data acquisition was constantly calibrated by a time-standard signal distributed via a long-wave radio center in Japan. The 478 keV γ-rays emanating from the EC-decay daughterof ^{7}Be (the first excited state of ^{7}Li) were measured using a HPGe detector coupled to a 4096-channel pulse-height analyzer. Here, we set the specific measurement duration to 21600 seconds (21480 seconds for the live measurement time and 120 seconds for the dead-time of the measurement system plus the sample exchange) for one data point. The amount of radioactivity associated with the decay of ^{7}Be (E_{γ}=478 keV) could be uniquely analyzed through the identification of the characteristic γ-rays. The decay curves obtained in the present measurements were fitted, by use of the MINUIT program distributed by the CERN Program Library. The reduced chi-square values of the exponential fits are between 0.9 and 1.1. The uncertainty due to the dead time was estimated to be less than 0.04%, and the systematic error in the measurements was estimated to be less than half of the statistical errors.

In this term, we have measured the decay rates and deduced the corresponding half-lives of ^{7}Be in samples of ^{7}Be@C_{70} at T=293K and 5K, and in Be metal (^{7}Be) at T=293K

with durations of almost three half-lives of ^{7}Be. All data obtained so far was plotted in Fig. 1. The closed squares indicate the half-lives obtained for the ^{7}Be@C_{60} sample at T=293K, the open circles for those obtained for the ^{7}Be@C_{60} sample at T=5K and, the closed circle for the half-life of the ^{7}Be@C_{70} at T=293K, further, the cross symbols for that of the Be metal (^{7}Be) at T=293K. It is surprising to note that the half-life of ^{7}Be in the ^{7}Be@C_{60} at T=5K and that in the the ^{7}Be@C_{70} at T=293K as well as T=5K stays in 52.44~52.47 days. These values are dramatically different from that in the Be metal (^{7}Be) at T=293K by almost 1.5%. This fact implies that the ^{7}Be atoms are located in a unique environment inside fullerenes[6-8].

References

1) E. Segr'e, Phy. Rev. **71** (1947)274.
2) L. Liu, CA. Huh, Earth and Planetary Sci. Lett. **180** (2000) 163.
3) CA. Huh, Earth Planet. Sci. Lett. **171** (1999) 325.
4) Ohtsuki T., et al., Phys. Rev. Lett. **77** (1996) 3522.
5) Ohtsuki, T., et al., Phys. Rev. Lett. **81** (1998) 967-970.
6) Ohtsuki T., et al., Phys. Rev. Lett. **93** (2004) 112501.
7) Ohtsuki T., et al., Phys. Rev. Lett. **98** (2007) 252501.
8) Morisato T. et al., Phys. Rev. **B78** (2008) 25416.

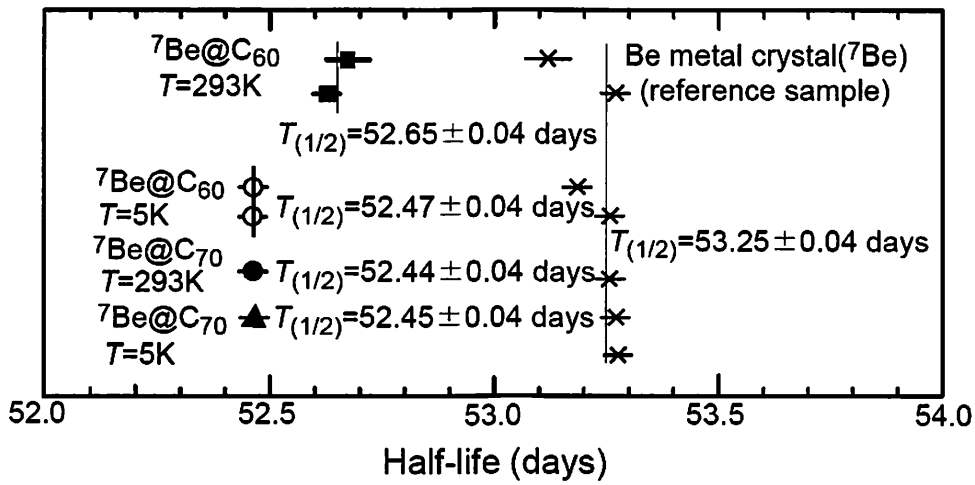

Figure 1. Half-lives are plotted: the closed squares for the ^{7}Be@C_{60} at T=293K, the open circles indicate the half-lives obtained for the ^{7}Be@C_{60} sample at T=5K, the closed circle for the ^{7}Be@C_{70} at T=293K, the cross symbols for the Be metal(^{7}Be) at T=293K. the closed triangle for the ^{7}Be@C_{70} at T=5K, the crossed symbols for Be metal(^{7}Be) at T=293K.

VII. RADIOPHARMACEUTICAL CHEMISTRY AND BIOLOGY

VII. 1. Synthesis of Iodine-124 Labeled αEGF-R Antibody and its Biological Evaluation

Horiuchi Y.[1], Funaki Y.[1], Kikuchi Y.[2], Yamazaki H.[1], and Ishii K.[1,2]

[1]*Cyclotoron and Radioisotope Center, Tohoku University*
[2]*Graduate School of Engineering, Tohoku University*

Introduction

Positron emission tomography (PET) is a very useful modality not only for visualizing different types of neurotransmissions in the human brain but also for diagnosing diseases, especially tumors. [^{18}F]FDG is widely used to PET probe for imaging tumors. However, the half-life ($T_{1/2}$) of radionuclides used for PET is short. Therefore, it is impossible for PET probes to provide biological information for diagnosis of tumors at several days after the administration.

^{124}I is a rather long-lived ($T_{1/2}$ = 4.15 days) positron-emitting nuclide. Hence, an image of high contrast could be acquired due to the washing-out effect if ^{124}I can be used as new PET probes. On the other hand, ^{124}I has a disadvantage for PET imaging. That is, its low positron abundance (only 22.9% of the disintegration), and prompt γ-rays pose the degradation of image resolution and the noise problem. In spite of those disadvantages, a good quality image was obtained for benzodiazepine receptors in the cerebral cortex of a living rat brain by using ^{124}I-iomazenil[1)]. Furthermore, the synthesis of new PET probes labeled using ^{124}I seems to be easy because the radioiodine has already been used as various SPECT probes.

To date, monoclonal antibodies (MAbs) that identify tumor-associated antigens are utilized in the cancer therapy. In the field of the diagnosis, the development of the PET probes using the character of these MAbs has already started[2,3)].

In the present study, we describe the synthesis of ^{124}I labeled antibody using the IODOGEN method, and the biological evaluation of it.

Material and methods

General

Chemicals and solvents were obtained from Aldrich and Wako Pure Chemicals. αEGF-R antibody and IODOGEN coated tube were also purchased from Wako Pure Chemicals. A431 cell line was obtained from Tohoku University, Institute of development, Aging and Cancer, Cell Resource Center for Biomedical Research.

Production of ^{124}I

Production of ^{124}I was carried out described in our previous paper[4]. Briefly, ^{124}I was produced by the $^{124}Te(p,n)^{124}I$ reaction. The target was $^{124}TeO_2$ / 6 wt% Al_2O_3 solid solution and it was bombarded with 14 MeV proton beams.

Antibody labeling

We used the IODOGEN method for labeling the antibody with radioiodine. An aliquot of αEGF-R antibody (ca. 0.1 μg, 1 μL) was added to an IODOGEN coated tube followed by addition of some activities of radioiodine (^{124}I or ^{125}I) in PBS (the total 100 μL). The solution was vortexed every 10 minutes at room temperature. After 30 min, 100 μL of 0.1% BSA-PBS was added. The labeled antibody with radioiodine was purified using gel filtration chromatography (Sephadex G25). 0.1% BSA-PBS as the eluted solution was collected (200 or 500 μL), and the radioactivity was measured by a γ-counter (AccuFLEX γ 7000, ALOKA).

Reaction with A431 cells

A431 cells were grown in D-MEM with 5% FCS in CO_2 incubator. Trypsin was added to peel off the cells from dishes. This suspensions were centrifuged at 900×*g* for 5 min and the pellets were washed and resuspended about 1×10^5 cells in 50 μL of PBS. It was reacted with 100 μL of ^{124}I-labeled antibody (^{124}I-Ab) (8 or 80 nCi) and 50 μL of PBS at 37°C for 30 min. The suspension was filtered on Whatman GF/B glass filters. The radioactivity of A431 cells on them was measured by a γ-counter. In the blocking experiment, about 1 μg of unlabeled antibody was added to the reaction.

Result and discussion

Figure 1 shows typical patterns of purifying the antibody using radioiodine. Usually, the labeled antibody was eluted at 3-5 mL, and the unreacted radioiodine was eluted at 7-11 mL (Fig. 1-A). As shown in Figs. 1-B and 1-C, the antibody labeled with ^{124}I is lower than that with ^{125}I. Actually, the labeling ratio using ^{125}I was approximately 70%, but that using ^{124}I was quite low (Table 1). Moreover, the labeling ratio decreases as the radioactivity of ^{124}I increases. ^{125}I emits only γ-rays of low energy in the EC decay. By contrast, the decay of ^{124}I produces high-energy prompt γ-rays (0.602 MeV) and high energy positron (1.5 and 2.1 MeV). If 100 μL of reacting solution has a spherical shape, its radius is 2.88 mm, so the effect of γ ray may be negligible small. On the other hand, the energy of principal β^+ emitted is 1.5 MeV and 2.1 MeV, which are generated by almost the same percentage. The ranges of each β^+ are 1.61 mm and 2.55 mm, respectively. Therefore, energy of β^+ is almost used in ionization of the reacting solution. As a result, it may be suggested that the hydrated electron that was high reductant produced in an aqueous solvent and the oxidized radioiodine was inhibited to generate. To improve this low reaction of ^{124}I, it was reported that the additions of unlabeled iodide increase the yield of radiolabeled antibody in IODOGEN method[5]. However, we did not examine this method, because it reduced the specific activity of ^{124}I-Ab.

Figure 2 shows the binding of ^{124}I-Ab to A431 cells. This binding rate was approximately 15% and it was not also changed using the ten-fold amount of ^{124}I-Ab. In the blocking study, it did not alter binding rate in spite of the addition of unlabeled antibody whose amount was 1,000-times in moles than ^{124}I-Ab. Therefore, the binding potential of ^{124}I-Ab to EGF-R might be almost nonspecific binding. As this reason, it is thought that ^{124}I may bind to antigen recognition site of αEGF-R antibody. Unfortunately, this result suggests that this ^{124}I-Ab is not available in PET imaging tracer. We will use another αEGF-R antibody and evaluate the synthesis in the same way.

References

1) Yamazaki H., Ishii K., Funaki Y., et al., the proceeding for 16th Pacific Basin Nuclear Conference 2008, to be published.
2) Kananova V., Wu A.M., Expert Opin. Drug Deliv. **3** (2006) 53.
3) Wiele C.V.D., Revets H., Mertens N., Nucl. Med. Mol. Imaging. **48** (2004) 317.
4) Yamazaki H., Funaki Y., Horiuchi Y., et al., CYRIC Annual Report (2006) 90.
5) McBride W.J., Zanzonico P., Sharkey R.M., et al., J. Nuc. Med. **47** (2006) 1678.

Table 1. Comparison of labeling rate with labeled antibody by ^{125}I and ^{124}I.

	Radioactivity	Antibody	I / antibody mol ratio	Labeling ratio
^{125}I	10 μCi	0	-	-
	300 μCi	2 μg	10	65 %
	100 μCi	1 μg	6.9	71 %
^{124}I	10 μCi	0.1 μg	0.48	31 %
	50 μCi	0.1 μg	2.4	29 %
	90 μCi	0.1 μg	4.3	15 %

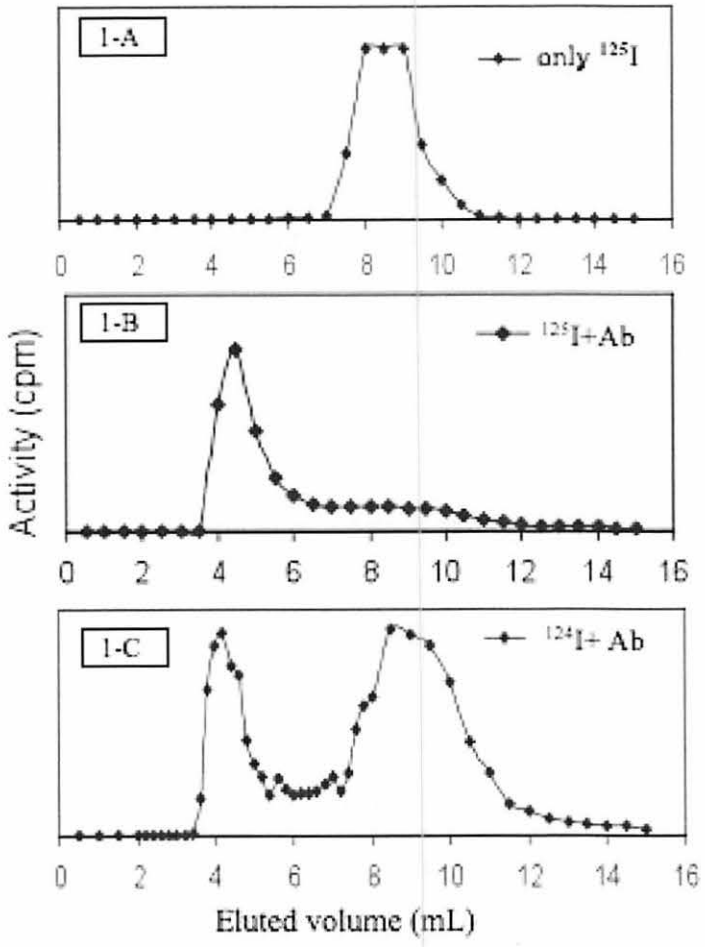

Figure 1. Gel filtration chromatogram of labeled antibody using ^{125}I or ^{124}I.

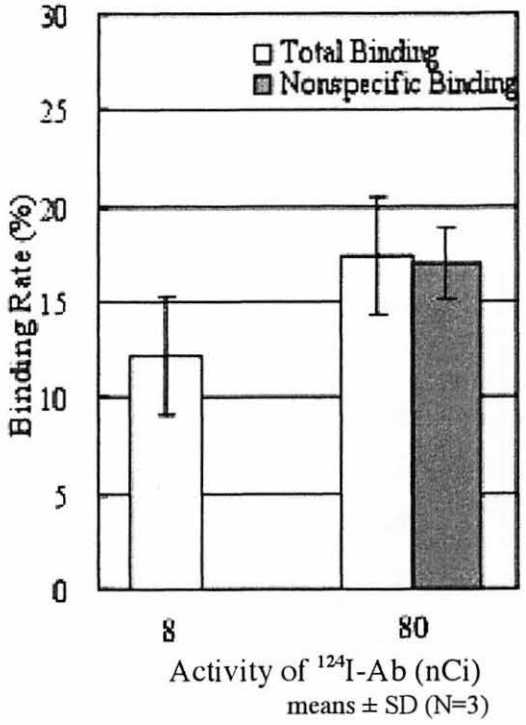

Figure 2. Binding rate of ^{124}I labeled antibody with A431 cells.

VIII. NUCLEAR MEDICINE

VIII. 1 Relationship Between Brain Histamine H_1 Receptor Occupancy, Subjective Sleepiness and Plasma Drug Concentration Following Oral Administration of Antihistamines Bepotastine and Diphenhydramine

Tashiro M.[1], Duan X.[1], Kato M.[3], Miyake M.[1], Watanuki S.[1], Ishikawa Y.[2], Funaki Y.[2], Iwata R.[2], Itoh M.[1], and Yanai K.[1,3]

[1]Divisions of Cyclotron Nuclear Medicine, Cyclotron and Radioisotope Center, Tohoku University
[2]Cyclotron and Radioisotope Center, Tohoku University
[3]Department of Pharmacology, Graduate School of Medicine Tohoku University

Introduction

Histamine H_1 receptor (H_1R) antagonists, or antihistamines, are often used for treatment of allergic diseases such as atopic dermatitis and seasonal rhinitis (also called pollinosis or hay fever). Antihistamines mainly act on these allergic sites in the peripheral tissues but can induce "sedative" side effects that result in subjective sleepiness and impaired performance. These undesirable central side effects are caused by blockade of nerve transmission in the histaminergic neuron system projecting from the tuberomammillary nucleus to almost all cortical areas[1-3]. First-generation antihistamines such as diphenhydramine and d-chlorpheniramine can easily penetrate blood-brain barrier (BBB) and tend to occupy a large proportion of post-synaptic H_1Rs[4-6]. Second-generation antihistamines, such as fexofenadine, cetirizine and olopatadine, can slightly penetrate the BBB and H1Rs are slightly occupied as having been demonstrated using positron emission tomography (PET)[4,7-9]. Variation in cerebral H_1R occupancy (H_1RO) of antihistamines results mainly from their different BBB permeability. Thus, sedative property of antihistamines can be evaluated in terms of H_1RO measured with PET and [^{11}C]doxepin, a radiopharmaceutical that specifically binds to H1Rs.

Methods

The present study was approved by the Committee on Clinical Investigation at

Tohoku University Graduate School of Medicine, Japan, and was performed in accordance with the policy of the Declaration of Helsinki. All experiments were performed at the Cyclotron and Radioisotope Centre, Tohoku University. Eight healthy male volunteers (mean age +/- s.d.: 24.4 +/- 3.3 years old) were studied after single oral administration of bepotastine 10 mg, diphenhydramine 30 mg, or placebo, using PET with [^{11}C]doxepin in a crossover study-design. The bepotastine is a novel second-generation antihistamine developed in Japan (Fig. 1), and diphenhydramine was added to the present study as an active placebo[10]. PET brain images were reconstructed with a filtered back projection algorithm. These brain images were normalized by plasma radioactivity data at 10 min post-injection and normalized by the distribution volume (DV) values in the cerebellum to yield specific binding potential ratio images[11]. Then, H_1R occupancy values were calculated using placebo data, and were compared between bepotastine and diphenhydramine. During the study, subjective sleepiness of each subject was measured in each subject at 0, 60, 120 and 180 min post-administration using the Line Analogue Rating Scale (LARS). Plasma concentrations of bepotastine and diphenhydramine were also measured at 0, 60, 120 and 180 min post-administration using liquid chromatography/ tandem mass spectrometry (LC/MS/MS). The relationship between plasma drug concentration (AUC) and H1RO was examined using Pearson's correlation test. A probability of $p<0.05$ was considered statistically significant[10].

Results

Result of mean subjective sleepiness is shown in Fig. 2. Mean subjective sleepiness of diphenhydramine peaked at 120 to 180 min post-administration and that of bepotastine peaked at 120 min post-administration. It was demonstrated that subjective sleepiness following diphenhydramine administration was significantly stronger ($p< 0.001$) than those of both bepotastine and placebo at 120 and 180 min post-administration, and that of bepotastine was not significantly different from that of placebo (Fig. 2).

Results of mean plasma concentrations of bepotastine and diphenhydramine demonstrated that the peak mean plasma concentration of bepotastine ranged from 60 to 180 min post-administration. Mean plasma concentration of diphenhydramine was maximal from 120 to 180 min post-administration[10] (data not shown here).

Brain images following oral administration of bepotastine demonstrated slightly lower binding potential ratio in comparison to those following placebo, and images

following diphenhydramine administration demonstrated significantly lower binding potential ratio in comparison to both placebo and bepotastine (Fig. 3). Overall cortical mean H_1RO of bepotastine and diphenhydramine were 14.8% and 56.8%, respectively[10].

Regarding the results of correlation analysis, mean H_1RO due to diphenhydramine tended to increase rapidly with diphenhydramine concentration when the baseline data are plotted together (Fig. 4A), while that due to bepotastine gradually increased with bepotastine concentration (Figure 4B). H_1RO following bepotastine administration did not significantly correlate to subjective sleepiness (Fig. 4D), while the H_1RO following diphenhydramine administration significantly correlated to subjective sleepiness (Figure 4C).

Discussion

To date, we have studied the mechanism of functional suppression in signal transmission through H_1Rs in the brain. In the present study, H_1RO of bepotastine, a second-generation antihistamine, was compared to that of diphenhydramine, a typical sedative antihistamine. H_1RO after a single oral administration of bepotastine 10 mg or diphenhydramine 30 mg was calculated as approximately 14.8% and 56.8%, respectively. Previous PET studies demonstrated that first-generation antihistamines occupied more than 50% of available H_1Rs and that the second-generation antihistamines would occupy around 0 to 20% of brain H_1Rs[4-6,9]. H_1RO after oral administration of bepotastine 10 mg was much lower than that of first-generation antihistamines (15% vs. 50%), and this result is in accordance with the categorization of bepotastine as a second-generation antihistamine. In addition, nowadays the second-generation antihistamines are further separated into 2 subgroups according to their BBB permeabilities[2,3]; a category that cause little sedation at low doses, but cause dose-related cognitive impairment at higher doses as seen with cetirizine and olopatadine, as well as the other category that does not cross BBB and therefore induces no sedation even at exceeded doses as seen with fexofenadine[9]. Based on the results of the present study, brain penetration of bepotastine has a certain level of dose dependency although subjective sleepiness is at a negligible level. The present results suggest that the bepotastine belongs to the category that causes little sedation at low doses but cause dose-related cognitive impairment at increased doses. The bepotastine demonstrated another cognitive study involving an active placebo is needed in order to draw a definitive conclusion. The dose dependency of H_1RO should also be examined by

PET measurements at higher doses.

References

1) Haas H., Panula P., Nat. Rev. Neurosci. **4** (2003) 121.
2) Holgate ST., Canonica G.W., Simons F.E., et al., Clin. Exp. Allergy. **33** (2003) 1305.
3) Casale T.B., Blaiss M.S., Gelfand E., et al., J. Allergy Clin. Immunol. **111** (2003) S835.
4) Yanai K., Ryu J.H., Watanabe T., et al., Br. J. Pharmacol. **116** (1995) 1649.
5) Yanai K., Ryu J.H., Watanabe T., et al., Methods Find Exp. Clin. Pharmacol. **17** Suppl C(1995) 64.
6) Yanai K., Okamura N., Tagawa M., et al., Clin. Exp. Allergy. **29** Suppl 3 (1999) 29.
7) Okamura N., Yanai K., Higuchi M., et al., Br. J. Pharmacol. **129** (2000) 115.
8) Tagawa M., Kano M., Okamura N., et al., Br. J. Clin. Pharmacol. **52** (2001) 501.
9) Tashiro M., Sakurada Y., Iwabuchi K., et al., J. Clin. Pharmacol. **44** (2004) 8900.
10) Tashiro M., Duan X., Kato M., et al., Br. J. Clin. Pharmacol. **65** (2008) 811.
11) Mochizuki H., Kimura Y., Ishii K., et al., Nucl. Med. Biol. **31** (2004) 1005.

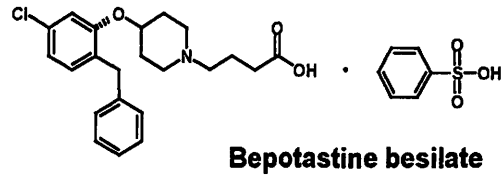

Bepotastine besilate

Figure 1. Chemical structure of bepotastine besilate.

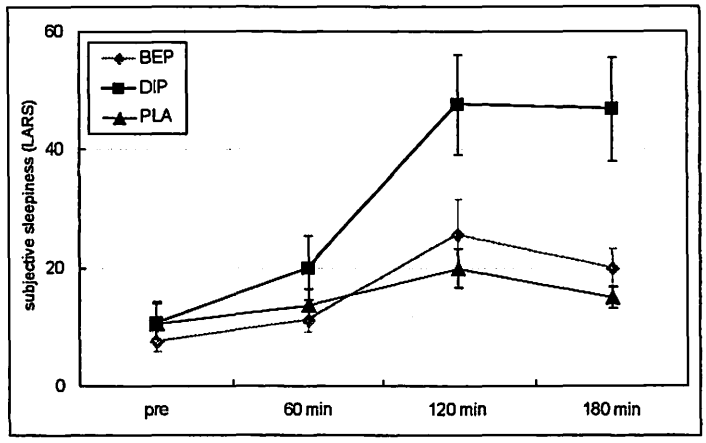

Figure 2. Subjective sleepiness evaluated using the Line Analogue Rating Scale (LARS). Eight healthy subjects were studied following oral administration of bepotastine (BEP, 10 mg), diphenhydramine (DIP, 30 mg), or placebo (PLA). *Reproduced from the reference [10] by courtesy of Blackwell Publishing Company.

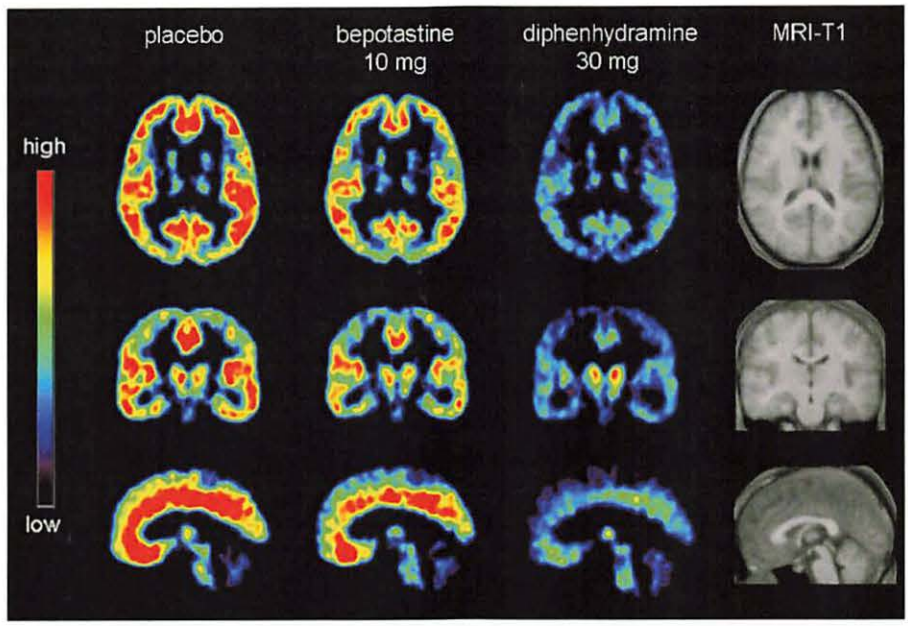

Figure 3. Binding potential ratio images of [^{11}C]doxepin in the human brain. Binding potential ratio of [^{11}C]doxepin was calculated in healthy male subjects (n=8) by PET following oral administrations of placebo (left), bepotastine (10 mg, middle) or diphenhydramine (30 mg, right) for each treatment condition were compared. White circles in the transaxial images indicate the regions of interest (ROIs). Brain image of each subject was transformed to fit stereotaxic brain space and was averaged across each drug condition to generate the mean images displayed here. *Reproduced from the reference [10] by courtesy of Blackwell Publishing Company.

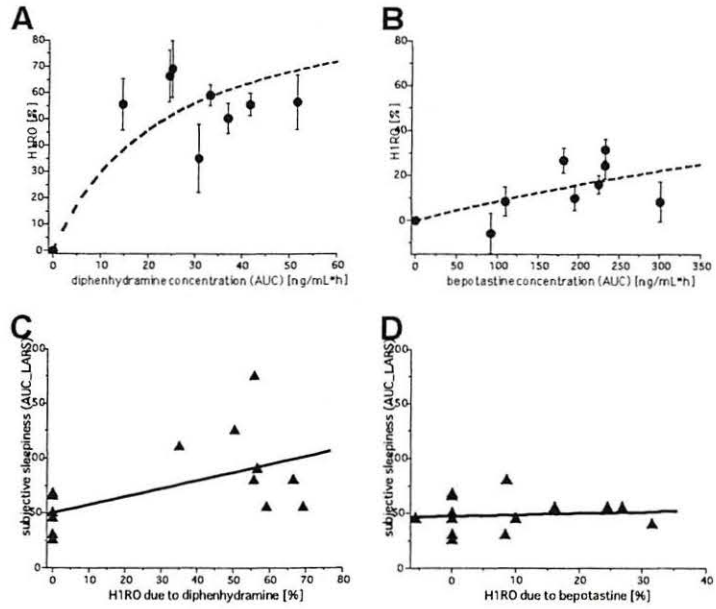

Figure 4. Relationship between mean H_1RO, plasma concentration and subjective sleepiness following administrations of bepotastine and diphenhydramine. Relationship between H_1RO and plasma concentrations was examined for diphenhydramine (A) and bepotastine (B) where the plasma concentrations of these antihistamines are presented as area under the curve (AUC). H_1RO of diphenhydramine rapidly increases with plasma concentration while H_1RO of bepotastine gradually increases with plasma concentration. Error bars represent intra-individual variability (S.D.). Subjective sleepiness (presented as AUC of line-analogue rating scale curve: AUC_LARS) demonstrates mild correlation to mean H_1RO due to diphenhydramine (C), while subjective sleepiness due to bepotastine demonstrates no correlation to mean H_1RO due to bepotastine (D). *Reproduced from the reference [10] by courtesy of Blackwell Publishing Company.

VIII. 2. Application of PET to Visualization of Daily Movements in Human Subjects

Tashiro M.[1], Fujimoto T.[2], Masud MM.[1], Miyake M.[1], Watanuki S.[1], Itoh M.[1], and Yanai K.[1,3]

[1]Divisions of Cyclotron Nuclear Medicine, Cyclotron and Radioisotope Center, Tohoku University
[2]Center for the Advancement of Higher Education, Tohoku University
[3]Department. of Pharmacology, Tohoku University Graduate School of Medicine

Introduction

Physical exercise such as running is executed through a sophisticated neural control system in the brain. Neural processing in the human brain plays crucial roles not only in the generation of motor outputs but also in the perception and integration of various sensory inputs. There are various methods as tools of functional neuroimaging, such as nuclear medicine techniques including positron emission tomography (PET) and single photon emission computed tomography (SPECT), and other imaging modalities such as functional magnetic resonance imaging (fMRI), near-infrared spectroscopy (NIRS), electroencephalography (EEG) and magnetoencephalography (MEG).

We have been utilizing PET for many years to measure the regional metabolic changes of the living human brain[1,2] and skeletal muscles during exercise[3,4]. PET has been a useful tool for measuring cerebral metabolic changes induced by exercise tasks. This is especially true for PET procedures that utilize the radio-labelled glucose analogue ([^{18}F]fluorodeoxyglucose: [^{18}F]FDG). The half-life of [^{18}F]FDG, approximately 110 min, is suitable for long observation ranging 30 to 60 min. The metabolic change is trapped, which enables the observation of the remaining metabolic "record" or "memory".

An activated regional brain activity is, in physiological condition, accompanied by increased demand for glucose and is immediately followed by dilation of brain capillaries that results in increased regional cerebral perfusion. The cerebral perfusion can be measured using and PET with radio-labelled water ([^{15}O]H_2O), although this technique is cumbersome and has some restrictions, where subjects have to exercise in the supine position during PET examinations because of the short half-life (approximately 2 min).

Then, PET with [^{18}F]FDG has a merit in observing daily human activities as they are in their natural circumstances[5]. We first applied this [^{18}F]FDG PET technique to human subjects during a running task in the upright posture[1] and during actual car-driving[6].

History of functional neuroimaging of exercise

PET has been used for measuring regional brain activity during or following exercise tasks using various radioactive pharmaceuticals such as [^{18}F]FDG and [^{15}O]H_2O. Regional cerebral metabolic changes induced by exercise have been examined in animals using autoradiography technique such as [^{14}C]deoxyglucose ([^{14}C]2-DG)[7,8]. [^{14}C]2-DG has been a useful tracer for exercise studies because it does not require the simultaneous scanning of subjects during an exercise task[9]. Using this technique, Sharp et al.[10] demonstrated an increase in glucose uptake in the cerebellar vermis of swimming rats. On the other hand, another study using free-running rats showed no selective activity in the cerebellar vermis but moderately increased glucose uptake for the entire cerebellum[11]. Thus, this autoradiography technique using [^{14}C]2-DG has been useful for exercise studies because it does not require simultaneous scanning of subjects during an exercise task[9]; The metabolic alteration is trapped, which enables the observation afterward. With this technique, data acquisition can be performed following exercise tasks. However, the [^{14}C]2-DG was not applicable to human activation studies because its very long half-life.

Later, human studies were also conducted in terms of brain perfusion. The first study on human brain activity during exercise was conducted by Herholz and coworkers[12]. In this study, subjects were examined during a riding task in the half-upright posture using the ^{133}Xe clearance method. Later, using PET with [^{15}O]H_2O, Fink and coworkers demonstrated the regional activation during and immediately after an ergometer task. They showed activation in the superomedial part of the motor cortex associated with leg and arm motion, which disappeared immediately following the cessation of the motor task[13]. In addition, they demonstrated that the lateral part of the motor cortex remained active possibly due to chest wall movement associated with post-exercise hyperventilation[13].

We first applied [^{18}F]FDG PET to healthy human subjects during a running task in the upright posture[1], and demonstrated augmented energy consumption in the parieto-occipital region during the task compared with the motor area. This was probably due to the higher energy consumption necessary for integrating multimodal sensory information. Our

results also showed that frontal activity was lower during running than during resting. In addition, our group also examined whole-body energy (glucose) redistribution and how exercise affects this distribution[14]. Based on our work[1], Kemppainen and coworkers examined absolute glucose consumption in the human brain of healthy volunteers. They demonstrated that the glucose consumption in the human brain was clearly diminished in proportion to exercise strength.

Methodological aspects

In studies using [^{18}F]FDG, subjects are instructed to run for a total of 30 to 40 min after [^{18}F]FDG injection, with 10 to 15 min of exercise before injection. The amount of injected [^{18}F]FDG is approximately 40 to 80 MBq (1 to 2 mCi per subject) if a 3D data acquisition system is used. If a 2D system is used, 200 MBq [^{18}F]FDG (approximately 5 mCi) is needed for data acquisition to compensate for the lower sensitivity of the detector system. For [^{18}F]FDG injection, a catheter is usually inserted into an antecubital forearm vein. The plasma time-activity curve (pTAC) of subjects demonstrates that the plasma [^{18}F]FDG concentration is very high for the first 10 min or so after injection, and then gradually decreases. Therefore, it is recommended that exercise tasks be conducted during the first 30 min or so. With this in mind, [^{18}F]FDG PET can be an ideal technique for studies on exercise physiology by separating "a task phase" and "data acquisition phase". This paradigm allows investigation of a totally free movement task assigned to subjects. With the [^{18}F]FDG PET technique, subjects can carry out any tasks, that is, not only running but any movement such as driving of a car or swimming[5,6]. PET scanning is initiated 40 min after [^{18}F]FDG injection since [^{18}F]FDG uptake in brain tissue reaches the plateau level at around 40 to 50 min post-injection. Our previous study suggested the presence of lateralization in muscular glucose metabolism used during upright running[1,5]. Although the temporal resolution of the [^{18}F]FDG PET technique is limited (just 30 to 60 min), it is this unique property that enables the application of this technique to observe human daily movement.

Results and discussion

Using [^{18}F]FDG PET technique, we have demonstrated the relative increase in glucose uptake in the temporo-parietal association cortex, occipital cortex, premotor cortex, primary sensorimotor cortex and the cerebellar vermis[1,5]. Relative reduction of glucose uptake was

detected in the prefrontal cortex, temporal cortex, cerebellar hemisphere, brain stem, striatum. Mean values of global brain glucose uptake was relatively lower in runners than in resting controls[1,5]. Kemppainen and coworkers replicated the study and demonstrated significant reduction of regional glucose metabolic rate in all cortical regions in correlation to exercise intensity, especially in the dorsal part of the anterior cingulate cortex[2].

Interestingly, they also pointed out that exercise training could be associated with adaptive metabolic changes in the frontal cortex[2]. Thus, global and regional brain metabolic decline was observed using [^{18}F]FDG PET especially in the limbic and frontal regions[1,2,5]. The relatively low glucose uptake detected in the cerebellar hemisphere in our study was brought about by the adaptation due to the repetition of the same motor task[15]. We speculated that the frontal and limbic hypometabolism was associated with emotional changes in runners, including the phenomenon called "runner's high", a sensation of well-being and reduced anxiety during running[5,16]. Dietrich and Sparling reported that endurance exercise tended to impair prefrontal-dependent cognitive ability in healthy young male volunteers[17]. Based on these findings, Dietrich proposed a new theory, a "transient hypofrontality theory (THT)", where the prefrontal activity is suppressed indirectly due to the limitation in energy supply to the brain in the situation where enormous amount of energy is needed for execution of endurance exercise[18]. Interestingly, this theory explains well a neural mechanism regarding the mental health benefits of exercise[17,18].

In addition, the [^{18}F]FDG PET technique can be applied to functional neuroimaging studies of other movement tasks such as car driving. So far, neural correlates of car-driving have been studied using fMRI and PET techniques and the reproducibility of the findings has been demonstrated[19-22]. However, interestingly, all these neuroimaging studies have been using simulated car-driving tasks instead of actual car-driving task[19-22].

Conclusion

PET neuroimaging of daily movement is a relatively new research topic. An advantage of [^{18}F]FDG PET method is that subjects do not have to be scanned at the same time than during the exercise. We have demonstrated the feasibility of [^{18}F]FDG PET in monitoring brain activations induced by actual running in the upright posture. This technique supplies further evidence to support the positive aspects of exercise in the fields of sports physiology and psychology.

References

1) Tashiro M., Itoh M., Fujimoto T., et al., J. Sports Med. Phys. Fitness **41** (2001) 11.
2) Kemppainen J., Aalto S., Fujimoto T., et al., J Physiol. **568** (Pt 1) (2005) 323.
3) Fujimoto T., Itoh M., Kumano H., et al., Lancet **348** (1996) 266.
4) Tashiro M., Fujimoto T., Itoh M., et al., J. Nucl. Med. **40** (1999) 70
5) Tashiro M., Itoh M., Fujimoto T., et al., Methods 45 (2008) 300.
6) Jeong M., Tashiro M., Singh L.N., et al., Ann. Nucl. Med. **20** (2006) 623.
7) Reivich M., Sokoloff L., Shapiro H., et al., Trans. Am. Neurol. Assoc. **99** (1974) 238.
8) Schwartzman R.J., Greenberg J., Revich M., et al., Exp. Neurol. **72** (1981) 153.
9) Gallagher B.M., Fowler J.S., Gutterson N.I., et al., J. Nucl. Med. **19** (1978) 1154.
10) Sharp F.R., Brain Res. **110** (1976) 127.
11) Vissing J., Andersen M., Diemer N.H., J. Cereb. Blood Flow Metab. **16** (1996) 729.
12) Herholz K., Buskies W., Rist M., J. Neurol. **234** (1987) 9.
13) Fink G.R., Adams L., Watson J.D., et al., J. Physiol. **489** (1995) 663.
14) Iemitsu M., Itoh M., Fujimoto T., et al., Med. Sci. Sports Exerc. **32** (2000) 2067.
15) Friston K.J., Frith C.D., Passingham R.E., et al., Proc. Biol. Sci. **248** (1992) 223.
16) Boecker H., Sprenger T., Spilker M.E., et al., Cereb. Cortex. **18** (2008) 2523.
17) Dietrich A., Sparling P.B., Brain Cogn. **55** (2004) 516.
18) Dietrich A., Psychiatry Res. **145** (2006) 79.
19) Calhoun V.D., Pekar J.J., McGinty V.B., et al., Hum. Brain Mapp. **16** (2002) 158.
20) Walter H., Vetter S.C., Grothe J., et al., Neuroreport. **12** (2001) 1763.
21) Uchiyama Y., Ebe K., Kozato A., et al., Neurosci. Lett. **352** (2003) 199.
22) Horikawa E., Okamura N., Tashiro M., et al., Brain Cogn. **58** (2005) 166.

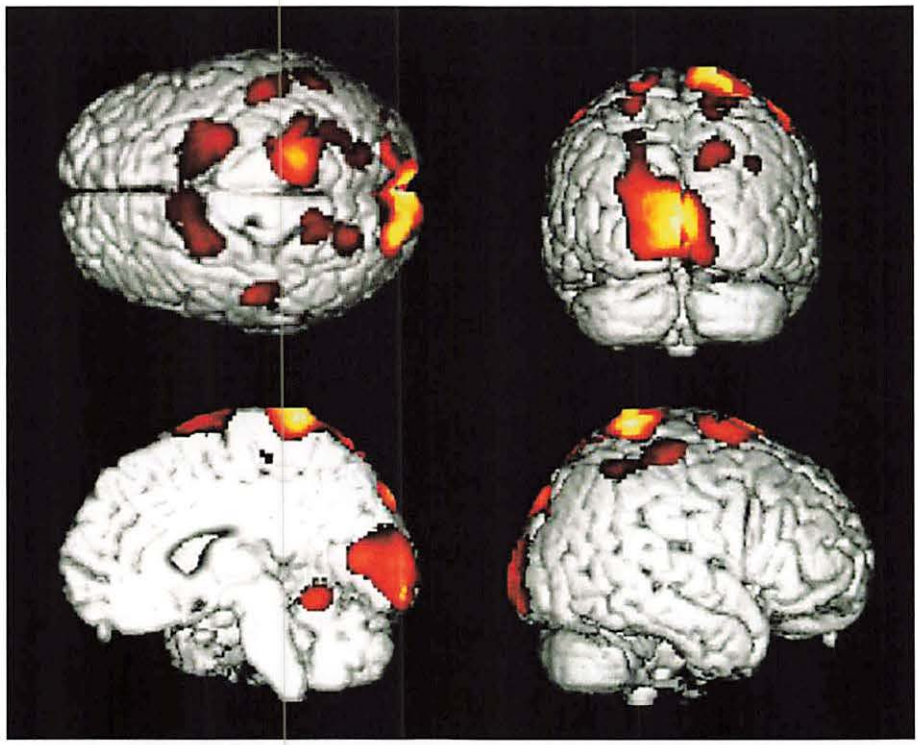

Figure 1. Results of [^{18}F]FDG PET study using a running task in the up-right posture in healthy volunteers.

VIII. 3. Regional Brain Activity at Different Exercise Intensity

Fujimoto T.[1], Itoh M.[2], Tashiro M.[2], Musud M.[2], Ishii K.[1], Targino Rodrigues dos Santos[2], and Watanuki S.[2]

[1]Department of Medicine and Science in Sports and Exercise, Tohoku University Graduate School of Medicine,
[2]Division of Nuclear Medicine, Cyclotron and Radioisotope Center, Tohoku University,

Introduction

Exercise often involves emotional changes. At higher exercise intensity, we easily get to exhaustion, but could also get refreshed at the same time. In addition we retain the sense of heavy exercise for a relatively long time. Therefore, we hypothesized that at higher exercise intensity, brain regions involving long-term memory within the limbic system as well as the motor area could be activated. The purpose of this study was to examine the regional brain metabolism induced during bicycle exercise at different intensity.

Methods

Regional brain activity was detected by positron emission tomography (PET) and glucose-tracer 18F-fluorodeoxyglucose (FDG) in 7 male volunteers (22.9 ± 1.6 year, $\dot{V}O_2max$ 46.2 ± 2.2 ml/kg·min). Each subject cycled at 3 different workloads (30%, 55% and 70% $\dot{V}O_2max$) using a bicycle ergometer on three separate days with an interval of more than two days. FDG (59 ± 11.2 MBq) was injected 5 minutes after the beginning of exercise and total exercise time was 35 minutes. PET emission scan started approximately 45 min after the termination of exercise using an SET2400W whole-body tomography system, (Shimadzu Co, Japan), with an intrinsic spatial resolution of 3.9 mm. The tomography system has 32 rings of BGO crystals separated by axial intervals of 3.15 mm covering an axial field of 20 cm. Transmission scan followed the emission scan, using a $^{68}Ge/^{68}Ga$ rotating external line source for correction of tissue attenuation. For statistical analysis, all brain images were anatomically normalized by mathematical calculation including linear and non-linear transformation to minimize inter-subject anatomical

variation using Statistical Parametric Mapping (SPM99)[1,2]. Brain images were smoothed using 16mm filter to improve signal to noise ratio. All pixel values were normalized to an arbitrary global mean value of 50 mg/100ml/min by ANCOVA, in order to exclude the effects of inter-subject variability in global cerebral glucose metabolism. A paired t-test was applied to each voxel; only voxel clusters were kept with voxels corresponding to $p<0.001$ in a single test and cluster size 10 voxel minimum, in one way (55% - 30%, 70% - 55%, 70% - 30%).

Results

As compared to exercise at 30% $\dot{V}O_2$max, exercise at 55% $\dot{V}O_2$max activated a distinct region in the thalamus (Fig. 1A). As compared to exercise at 55% $\dot{V}O_2$max, exercise at 70% $\dot{V}O_2$max activated regions in the superior frontal gyrus, the right superior temporal gyrus, the cingulate gyrus and the left brainstem (Fig. 1B). As compared to exercise at 30% $\dot{V}O_2$max, exercise at 70% $\dot{V}O_2$max activated areas in the right insula, the left caudate, the bilateral cingulate gyrus and the left cerebellum (Fig. 1C). There was no marked increase in the regional brain activity of primary motor area relative to exercise intensity.

Discussion/Conclusion

These results clearly show that the brain regions related to emotion and memory were more activated at higher exercise intensity. These areas making projections to each other may subconsciously make episode memory of the exercise experience at higher exercise intensity. Exercise of higher intensity may be beneficial for pathophysiological states in which brain activity involving emotion or memory is down regulated, such as depression or amnesia.

References

1) Friston K.J., Neuroimage 4 (1996) 97.
2) Friston K.J., Human Brain Mapp. 2 (1995) 189.

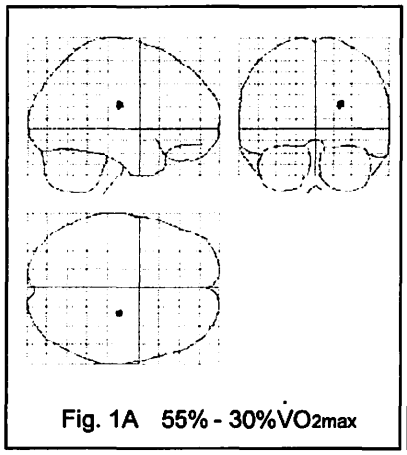

Fig. 1A 55% - 30%$\dot{V}O_{2max}$

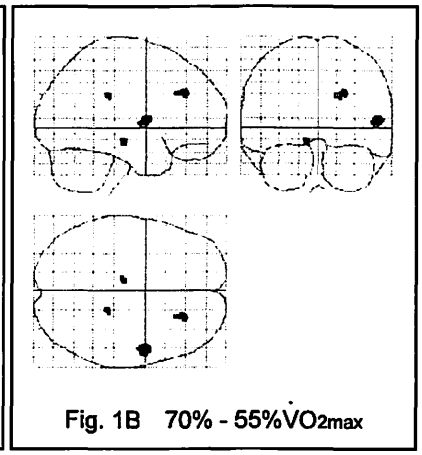

Fig. 1B 70% - 55%$\dot{V}O_{2max}$

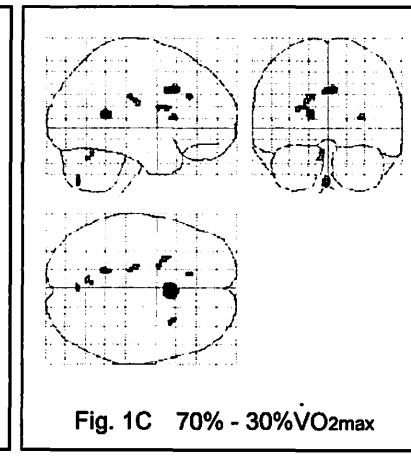

Fig. 1C 70% - 30%$\dot{V}O_{2max}$

Figure 1A shows brain activity between 55% $\dot{V}O_2$max - 30% $\dot{V}O_2$max exercise.
Figure 1B shows brain activity between 70% $\dot{V}O_2$max – 55% $\dot{V}O_2$max exercise.
Figure 1C shows brain activity between 70% $\dot{V}O_2$max – 30% $\dot{V}O_2$max exercise.

VIII. 4. FFA and Glucose Uptake of Skeletal Muscle and Myocardium at Different Exercise Intensity

Fujimoto T.[1], Tashiro M.[2], Kemppainen J.[3], Kitda K.[1], Kubota K.[4], Ishii K.[1], Knuuti J.[3], and Itoh M.[2]

[1] Department of Medicine and Science in Sports and Exercise, Tohoku University,
[2] Cyclotron and Radioisotope Center, Tohoku University,
[3] Turku PET Centre and Department of Medicine, University of Turku
[4] Divison of Nuclear Medicine, Department of Radiology, International Medical Center of Japan

Introduction

Efficiency of energy substrate supply form blood is one of the main factors of exercise performance. We previously reported the relationship between glucose uptake of skeletal muscle and myocardium, and exercise intensity[1,2]. Glucose uptake of skeletal muscle and myocardium didn't increase according to increment of exercise intensity in untrained men. The purpose of this study was to investigate the relationship between exercise intensity and FFA and glucose uptake of skeletal muscle and myocardium with single photon emission tomography (SPECT) and Positron Emission tomography (PET), respectively.

Methods

Measurement of glucose uptake.

Four-teen healthy subjects (30.4±6.2 years, mean±S.E.) participated this glucose study. Maximal aerobic power ($\dot{V}O_2max$) was 49.6±9.7 ml/Kg/min. Each subject was studied on three separate days with time interval of more than two days. Bicycle ergometer at three different workloads was used, 30, 55and 75 % $\dot{V}O_2max$. ^{18}F-FDG was injected 10 minutes after the beginning of exercise and total exercise time was 35 minutes. PET imaging started immediately after the exercise. PET studies were performed using an eight ring ECAT 931/08 –tomograph. Plasma radioactivity, glucose and lactate acid values were obtained during studies. Quantification of glucose uptake was based on the method developed by Sokoloff et al[3]. Glucose uptake was measured in the quadriceps

femoris muscle (QF) and in the myocardium.

Measurement of FFA uptake.

Six untrained subjects (20.2 ± 1.2 years) participated FFA study. $\dot{V}$O2max was 52.5±2.1 ml/Kg/min. Study design was almost same as the glucose study. ^{123}I-labeled 15-(p-iodophenyl)-3-(R,S)-methyl-pentadecanoic acid (^{123}I-BMIPP) that is tracer of FFA was injected intravenously 5 minutes after the subjects started exercise. Single photon emission tomography (SPECT) measurements were started immediately after the exercise. Tomographic images were obtained from regions of the QF and myocardium. ^{123}I-BMIPP counts per minute indicate the extent of ^{123}I-BMIPP uptake in tissue and were corrected in terms of total whole body count (FU; regional mean count / whole body count; optional unit) in each experiment.

Results

QF glucose uptake increased significantly from 30% $\dot{V}O_{2max}$ to 55% $\dot{V}O_{2max}$ intensity ($P < 0.05$), but not further during 75% $\dot{V}O_{2max}$ intensity (Fig. 1A). QF ^{123}I-BMIPP uptakes at 40% and 55%$\dot{V}O_{2max}$ intensity were significantly higher than that of 75%$\dot{V}$O2max (Fig. 1B). Myocardial glucose uptake did not increase in a linear manner with increasing exercise intensity. At the highest exercise intensity glucose uptake decreased significantly as compared to both 30 and 55% intensity levels ($p<0.05$) (Fig. 1C). There were no differences in ^{123}I-BMIPP uptake at each experiment in the myocardium (Fig. 1D). Plasma lactate concentration was strikingly increased according to the exercise intensity.

Discussion/Conclusion

These results suggested that blood glucose and FFA were not the main energy source of skeletal muscle and myocardium to increase the exercise intensity in untrained subjects. At higher exercise intensity, intramuscular substrates, most likely glycogen would be the main energy source of the increment of exercise intensity. The increased myocardial energy that is needed during high intensity exercise is supplied by substrates other than glucose, like as lactate.

References

1) Kemppainen J., Fujimoto T., et al., J. Physiol. **542** (2002) 403.

2) Fujimoto T., Kemppainen J., et al., Med. Sci. Sports Exerc. **35** (2003) 777.
3) Sokoloff L., et al., J. Neurochem. **28** (1977) 897.

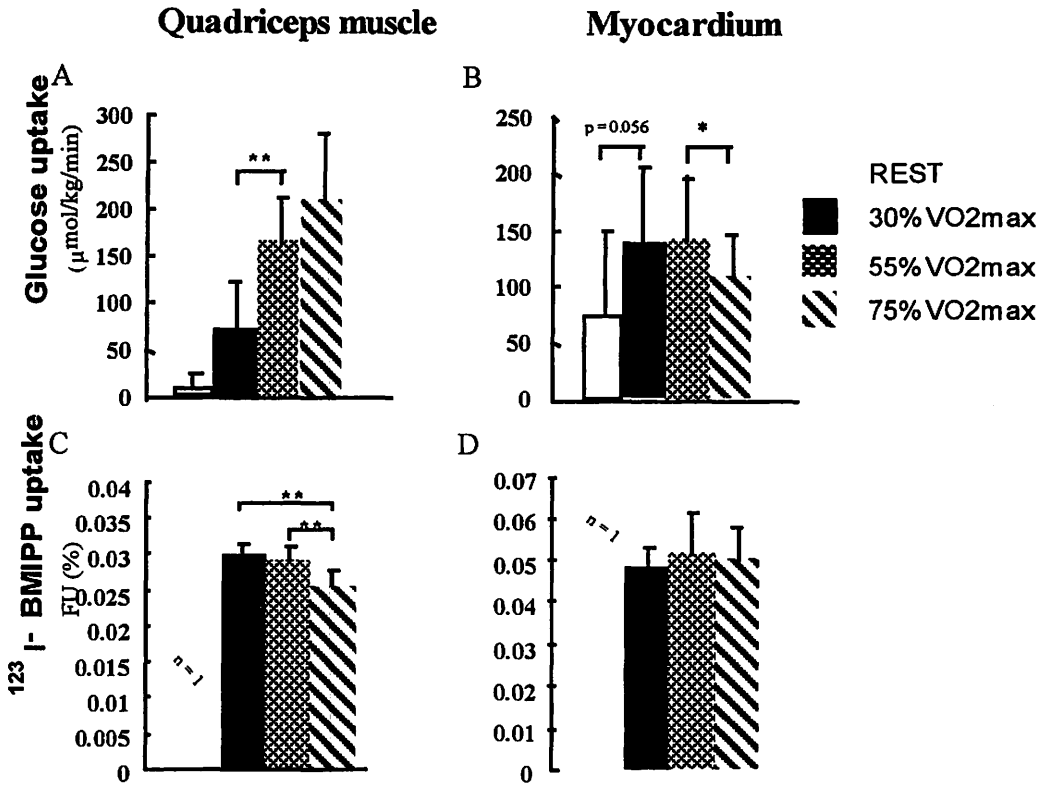

Figure 1. A shows the relationship between the glucose uptake of the quadriceps femoris and the exercise intensity. Figure 1B shows the relationship between the glucose uptake of myocardium and the exercise intensity. Figure 1C shows the relationship between the ^{123}I- BMIPP uptake of the quadriceps femoris and the exercise intensity. Figure 1D shows ^{123}I- BMIPP uptake in the myocardium and the exercise intensity.

VIII. 5. Human Study Regarding the Brain Responses to Respiratory Resistance

Targino Rodrigues dos Santos.[1,2], Kikuchi Y.[3], Hida W.[5], Tashiro M.[1], Hatazawa J.[4], Miyake M.[1], Watanuki S.[1], Yamaguchi K.[1], and Itoh M.[1]

[1]Division of Nuclear Medicine, Cyclotron Radioisotope Center, Tohoku University,
[2]CMI, Inc
[3]Respiratory Division, Sendai National Hospital,
[4]Department of Tracer Kinetics, Osaka University Medical School
[5]Department of Informatics on Pathophysiology, graduate School of Information Sciences, Tohoku University,

The main role of respiration is to exchange oxygen and carbon dioxide through the lungs. It is controlled involuntarily by the respiratory center in the pons and voluntarily through the motor cortex. Dyspnea, shortness of breath or a subjective discomfort of breathing, usually associated with cardio-pulmonary diseases, occurs even in normal conditions during intense physical exertions, such as exercise or loaded breathing, or at high altitude. Respiration has an intimate relation to emotions. When angry, excited, fearful, or depressed, breathing takes a different pattern. The aim of this study was to localize anatomical sites of the brain of healthy subjects that were functionally altered by resistive inspiratory loaded breathing lasting for 30 minutes by using a brain imaging technique, PET and statistical parametric mapping[1]. Twenty-eight male normal volunteers with mean age of 30.2 years (SD 8.6) were included in this study. Respiratory resistance was made using an apparatus consisting of a semi-closed ventilation circuit with a unidirectional Hans-Rudolph valve[2]. Respiratory overloads were introduced by applying inspiratory resistance to the inspiratory port of the valve while subjects breathed through the valve. Thirteen subjects were studied during 30 *cm H_2O/L/sec* inspiratory resistive loading (moderate task group), five subjects were studied during 70 *cm H_2O/L/sec* inspiratory resistance (severe task group), and the other ten subjects were studied during resting breathing without resistance (control group). After breathing for one minute the restricted respiration task was performed during 30 minutes at each level of resistance, just after this the subjects rated the sensation of difficulty in breathing (dyspnea) using a modified Borg Scale[3], ranking the magnitude of difficulty in breathing, from 0 (none) to 10 (maximal). Relative regional

cerebral glucose metabolism was measured with positron emission tomography (PET; PT931 (CTI, Tennessee)) by using fluorine 18 (^{18}F)-labeled fluorodeoxyglucose (FDG). PET studies were carried out by injecting average 191.51 MBq (SD 69.42) of FDG at one minute after applying the inspiratory resistance or during resting breathing. Scanning was started at 30 minutes after injection of FDG. The posture was kept supine throughout the examination run.

Image processing and statistical analyses were carried out using SPM99. This procedure included anatomical standardization of a subject's brain images to mach a standard PET template (template of SPM99). The spatially transformed images were smoothed using a 13×13×12 mm at full width half maximum (FWHM) 3D-Gaussian Kernel. The group comparisons were made using ANOVA and Student's t-test adopting the threshold of significance at $p < 0.001$, uncorrected for multiple comparisons. Group comparisons showed extensive activations and deactivations. Inspiratory loads, both mild and moderate, induced brain activations in the rectal gyrus, precentral gyrus and postcentral gyrus (Figs. 1 and 2). Dyspnea induced activations in the bilateral rectal gyrus (Brodmann area 11, Fig. 1) and the right temporal pole. Increases in glucose metabolism in the rectal gyrus as well as in the amygdala (not activated in this study) have been reported in panic disorder[4,5]. The right temporal pole has been associated with respiratory rhythm[6]. Activations of this area found in this study supported this hypothesis. Most of these areas responded linearly with the level of respiratory resistance except the superior, temporal gyrus, inferior frontal gyrus and middle temporal gyrus; these areas responded all or nothing. Extensive metabolic reduction was found in the parietal–occipital brain areas with the highest reduction in the right cingulate gyrus (Brodmann area 23, Fig. 2).

In conclusion respiratory distress activated the motor area, frontal lobe and temporal pole bilaterally. These areas could be related to respiratory controls and emotion. Extensive reduction in brain metabolism was found in the posterior part of the brain including the parietal lobe

References

1) Friston K.J., Holmes A.P., Worsley K.J., Poline J.P., Frith C.D., Frackowiak R.S., Human Brain Mapping **2** (1995) 189
2) .Taguchi O., Kikuchi Y., Hida W., Iwase N., Satoh M., Chonan T., Takishima T., J. Appl. Physiol. **71** (1991) 2183.
3) El-Manshawi A., Killian K.J., Summers E.,Jones N.L., J. Appl. Physiol. **61** (1986) 896.
4) Reiman E.M., Raichle M.E., Butler F.K., Herscovich P., Robins E., Nature **310** (1984) 683.

5) Nordahl T.E., Semple W.E., Gross M., Mellman T.A., Stein M.B., Goyer P., King A.C., Uhde T.W., Coh en R.M., Neuropsychopharmacology **3** (1990) 261.
6) Masaoka Y., Homma I., Respiration Physiology **128** (2001) 171.

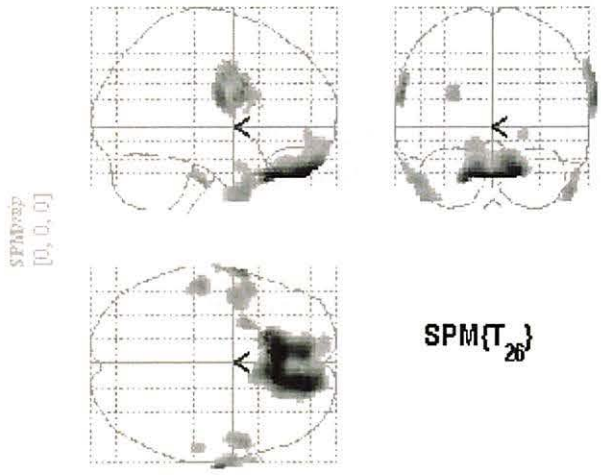

Figure 1. brain activation by respiratory distress, comparison between group 30 minus control..

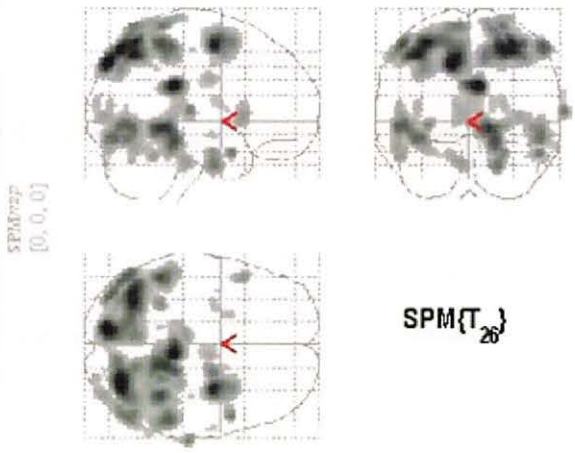

Figure 2. brain deactivation by respiratory distress, a comparison between control minus group 30.

VIII. 6. Correlation between Car-driving Performance and Regional Brain Activity after Oral Administration of a Sedative Antihistamine

Shibuya K.[1,3], Sakurada Y.[1], Tashiro M.[3], Mochizuki H.[1], Horikawa E.[4], Maruyama M.[2], Okamura N.[1], Arai H.[2], and Yanai K.[1]

[1]Department of Pharmacology, Graduate School of Medicine, Tohoku University,
[2]Departments of Gerontology, Institute of Development, Aging, Cancer, Tohoku University,
[3]Division of Cyclotron Nuclear Medicine, Cyclotron and Radioisotope Center,
[4]Center for Comprehensive and Community Medicine, Faculty of Medicine, Saga University,

Introduction

Histamine H_1 receptor antagonists (antihistamines) are widely used for treatment of allergic disorders, and are well-known for their central side effects such as drowsiness and impaired psychomotor performance[1]. Car-driving is closely connected with our everyday life. There are so many reports about the effects of antihistamines on car-driving performance but its mechanism has not been demonstrated yet. Recently, some functional MRI (fMRI) studies have been published on regional brain activities during simulated car-driving[2-4]. Previously, we reported the rCBF changes during simulated car-driving after oral administration of d-chlorpheniramine, a sedative antihistamine, using positron emission tomography (PET) with $[^{15}O]H_2O$[5,6]. In this report, we demonstrate additional results of correlation analysis between car-driving performances and the regional brain activity, such as car-driving.

Materials and Methods

Subjects

Fourteen healthy male volunteers, ranging 20-25 years old (mean +/- SD :22.5 +/- 1.8), participated in the present study. All subjects were evaluated as right-handed based on the Edinburgh inventory and Chapman test. This study protocol was approved by the ethics committee of Tohoku University Graduate School of Medicine. Written informed consent was obtained from each subject and the study was performed in compliance with

the relevant laws and institutional guidelines[5,6].

Study design

The present study was conducted as a single-blind crossover study. The subject was given one of a d-chlorpheniramine 6 mg repetab or a placebo before PET examination. The PET investigation started approximately 2 hours after oral administration of d-chlorpheniramine 6 mg and so did it for placebo. PET scans were performed for the following three conditions such as 1) resting, 2) active driving, and 3) passive driving as reported previously[5,6].

Driving simulation

A commercially-available software (Gekisoh 99, Twilight Express Co., Tokyo, Japan) was used for simulated car-driving task. The subjects were positioned in a PET scanner, wearing a head mount display (HMD: Glasstron PLM-A35, SONY, Tokyo, Japan). Subjects were instructed to drive according to video instructions projected onto the HMD. Afterward, driving performance was evaluated for the following five assessment items: 1) time, 2) number of crashes, 3) number of over-steering, 4) number of stop due to crashes, and 5) subjective sleepiness[5].

PET measurements and data analysis

The brain perfusion images were obtained using a 3D-acquisition PET scanner (SET 2400W, Shimadzu Co. Ltd., Japan). These images obtained were realigned, normalized and smoothed by Statistical Parametric Mapping (SPM) software. And then, the correlation analysis was performed between the regional brain activity and driving performance indices as well as sleepiness index in order to find the regions with positive and negative correlations in placebo and d-chlorpheniramine conditions, respectively (Not corrected for multiple comparisons: $p< 0.001$).

Results

All 14 subjects completed the entire investigation. In driving performance evaluation, "over-steering" showed significant difference between the placebo and d-chlorpheniramine conditions ($p< 0.05$), but the difference of other items were not significant. Especially, there was no difference between placebo and d-chlorpheniramine on subjective

sleepiness[5].

The regions with significant negative correlation to the number of over-steering in placebo condition was found in the somatic sensory association (Brodmann's area 7: BA7) and the cingulate cortices (BA23, 30, 31 and 37), whereas in d-chlorpheniramine condition, significant negative correlation was observed in the primary motor cortex (BA4), frontal eye field (BA8), the visual association cortex (BA18 and 19) and the cingulate cortex (BA23) (Fig. 1). And the regions with significant positive correlation with "subjective sleepiness" in placebo condition was found in the premotor (BA6), the somatic sensory association (BA7), the prefrontal (BA9), the primary and secondary visual cortex (BA17, 18 and 19) and the cingulate cortices (BA30), whereas in d-chlorpheniramine condition, significant positive correlation was observed in the premotor (BA6), the somatic sensory association (BA7), the includes frontal eye field (BA8), the visual association cortex (BA19) and the cingulate cortex (BA24).

Discussion

The aim of the current study was to perform correlation analysis between car-driving performance and regional brain activity. When drivers operate the steering wheel, they might recognize the road alignments through their eyes and perform steering. Significant negative correlation was observed in a placebo condition between the cingulate gyrus activity and the number of over-steering. This finding may suggest the involvement of the cingulate gyrus in visuospatial cognition. The results in a d-chlorpheniramine condition demonstrated a less-significant correlation. This result suggest that suppression of the cingulate gyrus activity due to d-chlorpheniramine was associated with the performance impairment in over-steering. The posterior cingulate gyrus might be playing an important role in visuospatial cognition.

In summary, our study shows that the oral administration of d-chlorpheniramine may affect the function of the cingulate gyrus. But, its mechanism can't explain by only their results. Thus, we will need to investigate on their mechanism.

References

1) Adelsberg B.R., Arch. Int. Med. **157** (1997) 494.
2) Walter H., Vetter S.C., Wunderlich A.P., Hahn S., Spitzer M., Neuroreport **12** (2001) 1763.
3) Calhoun V.D., Pekar J.J., McGinty V.B., Adali T., Watson T.D., Pearlson G.D., Hum Brain Mapp. **16** (2002) 158.

4) Uchiyama Y., Ebe K., Kazato A., Okada T., Sadato N., Neurosci. Lett. **352** (2003) 199.
5) Tashiro M., Sakurada Y., Mochizuki H., Horikawa E., Maruyama M., Okamura N., Watanuki S., Arai H., Itoh M., Yanai K., Hum. Psychopharmacol. **23** (2008) 139.
6) Horikawa E., Okamura N., Tashiro M., Sakurada Y., Maruyama M., Arai H., Yamaguchi K., Sasaki H., Yanai K., Itoh M., Brain Cogn. **58** (2005) 166.

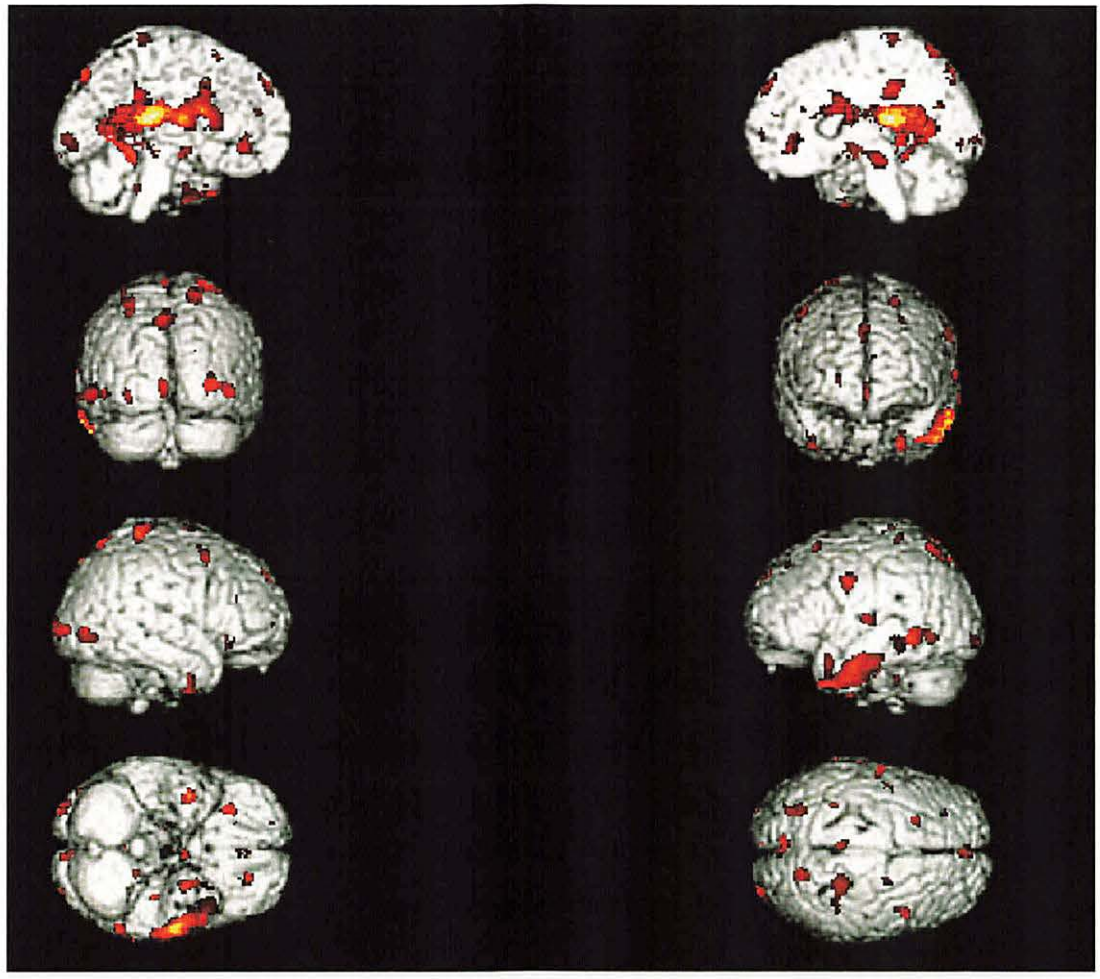

Figure 1. The regions with significant negative correlation with "over-steering" following placebo administration.

VIII. 7. [^{18}F]FDG-PET Measurement of Glucose Metabolism during Exercise Using Two Analytical Approaches

Mehedi M.[1], Fujimoto T.[2], Miyake M.[1], Watanuki S.[1], Itoh M.[1], and Tashiro M.[1]

[1]Divisoin of Nuclear medicine, Cyclotron and Radioisotope Center, Tohoku University,
[2]Center for the Advancement of Higher Education, Tohoku University,

Background

Our previous reports[1,2] employed the semiquantification method (standardized uptake values: SUV) to assess organ glucose metabolism after exercise with ^{18}F-2-fluoro-2-deoxyglucose and three-dimensional positron emission tomography technique ([^{18}F]FDG and 3D-PET). Recently, Kemppainen J. and co-workers assessed glucose metabolism of lower limb muscles and myocardium using absolute quantification method (rMRGlc)[3]. However, no reports have evaluated glucose metabolic changes at whole-body level after exercise task with 3D-PET technique, comparing semiquantitative and quantitative analytical methods. We tried to elucidate the workloads-induced organ glucose metabolism using two analytical methods (semiquantitative and quantitative), as to establish relationship between two PET quantification approaches.

Methods

Eleven healthy male volunteers collaborated with this investigation. All subjects abstained from eating and drinking for at least 5 hours before the experiment. They were asked not to perform any kind of physical exercise from one day before investigation. 5 subjects served as exercise group whose ages ranged from 21 to 23 y (21.80 ± 0.84 y; mean ±S.D.). Another 6 subjects, aged mean 24 ± 5.34 y (range; 19 ~ 33 y) were studied as resting control maintaining the same study protocol without exercise. [^{18}F]FDG dose for control was in average 42.48 ± 6.63 MBq (mean ± S.D.). A written fully informed consent was obtained from each subject before the study. This study protocol was approved by the Clinical Committee for Radioisotope Studies of Tohoku University.

Ergometer bicycle exercise was arranged at 40% and 70% $\dot{V}O_{2max}$ workloads. $\dot{V}O_{2max}$ was measured by intermittent exercise on an ergometer bicycle (Monark 818E, Sweden), and oxygen consumption rate was determined by an automated metabolic unit machine (AE280-S, Minato Co. Ltd. Osaka, Japan). Before the experiment, subjects rested for 20 minutes in a dim lit quiet room. One teflon catheter was inserted to their antecubital veins of the left hand for blood sampling to measure plasma glucose, lactate and insulin. Another teflon catheter was inserted to opposite antecubital veins for [^{18}F]FDG administration. Then, they started ergometer bicycle riding at the speed of 60 revolution/min (Monark 818E, Sweden) at both workloads (40% and 70% $\dot{V}O_{2max}$). [^{18}F]FDG was injected through a catheter at 10 min later following exercise task. The radioactivity dose for the exercise group was 38.37 ± 2.15 MBq (mean ± S.D.). After injection, subjects continued to pedal the bicycle for another 30 min, completing a total of 40 min task. Immediately after intravenous administration of [^{18}F]FDG, heated arterialized venous blood was sampled from cubital vein opposite to the injection site. Plasma [^{18}F]FDG concentrations were measured both during exercise and PET scan for 24 times. Plasma metabolite concentrations (i.e., Glucose, lactate and insulin) were measured at two points such as pre and post exercise states.

Subjects lay down in supine position on PET table with eyes open following exercise task. The PET room was kept dimmed and quiet. The scan protocol was as follows: a 3 dimensional (3D) whole-body emission scan (3 min × 9F) was performed from knee to the vertex followed by transmission scan (3 min × 9F) using a PET apparatus (SET2400W, Shimadzu, Kyoto, Japan). The transmission scan (post-injection mode) was performed with a ^{68}Ge/^{68}Ga external rotating line source (370 MBq at purchase).

Regions of interest (ROIs) were set on the skeletal muscles of thigh, lumbar/gluteal regions, and visceral organs such as liver, heart and brain etc. (Figure 1). To evaluate the rate of glucose utilization, an autoradiographic method[4] was applied using the following equation:

$$rMRGlc = \frac{Cp}{LC}\left[\frac{K^*_1 k^*_3}{k^*_2 + k^*_3}\right]\left[\frac{C^*i(T) - C^*e(T)}{C^*m(T)}\right]$$

In another, semiquantitative analysis (Standard uptake value; SUV) was done by using the following equation:

$$\frac{Mean\ ROIcts\ (cps/pxls) \times Body\ weight(g)}{Injected\ dose\ (\mu Ci) \times Calibration\ factor\ (cps/\mu Ci)}$$

Group comparisons were done by using one-way analysis of variance (ANOVA) and Tukey's test (post-hoc) analysis. The significant differences were set at $p<0.05$. Correlation was calculated using Pearson's correlation coefficient analysis.

Results

[^{18}F]FDG uptake was only remarkable in the brain, heart and urinary bladder in the resting subject, while high uptake was visualized in skeletal muscles at exercise state (Fig. 1). Glucose metabolism (SUV and rMRGlc) was increased in the skeletal muscles of thigh and lumbar/gluteal regions ($p<0.05$), and was decreased in the brain ($p<0.05$) after exercise task (40% and 70% $\dot{V}O_{2max}$ workloads). A correlation between SUV and rMRGlc was found among organs (i.e., Thigh, liver, heart and brain), except in the lumbar/gluteal muscles. Figure 2 clearly depicted a good correlation between SUV and rMRGlc in the brain (a) and heart (b); however, a non-suggestive correlation was found in the lumbar/gluteal skeletal muscle (c). The changes in plasma metabolites were as follows: stable plasma glucose concentrations, an increase ($p<0.05$) plasma lactate concentration at post-exercise condition of 70% $\dot{V}O_{2max}$ (5.3 ± 2.4 mmol/liter) to compare with pre-exercise condition (0.9 ± 0.2 mmol/liter). The plasma insulin concentration was decreased ($p<0.05$) only at post-exercise workload of 70% $\dot{V}O_{2max}$ (2.0±0.7 _U/mol) than pre-exercise condition (4.6±1.5 _U/mol).

Conclusion

Organ glucose uptake either increased or decreased almost linearly with exercise loads up to moderate workload (70% $\dot{V}O_{2max}$). In spite of complexity of energy metabolic controls such as glucose-fatty acid metabolic interaction, aerobic-anaerobic interaction, and involvement of glycogenolysis[5], exercise-induced organ glucose metabolism were successfully assessed with [^{18}F]FDG-3D-PET technique and two analytical approaches. Organ glucose uptake either increased or decreased almost linearly with exercise loads up to moderate workload (70% $\dot{V}O_{2max}$), suggesting of homeostatic metabolic control. Semiquantitative method without blood samplings was found useful to estimate a rough trend of glucose consumptions. However, one organ failed to have good correlations between SUV and rMRGlc, the lumbar and gluteal muscles for example, which demonstrates that semiquantitative approach needs a great care when metabolic rate of glucose utilization changes at whole-body level.

References

1) Fujimoto T., Itoh M., Kumano H., et al., Lancet **348** (1996) 266.
2) Tashiro M., Fujimoto T., Itoh M., et al., J. Nucl. Med. **40** (1999)70.
3) Kemppainen J., Fujimoto T., Kari K.K., et al., J. Physiol. **542** (2002)403.
4) Phelps M.E., Huang S.C., Hoffman E.J., et al., Ann. Neurol. **6** (2005)371.
5) Kjaer M., Howlett K., Langfort J., et al., J. Physiol. **528** (2000)371.

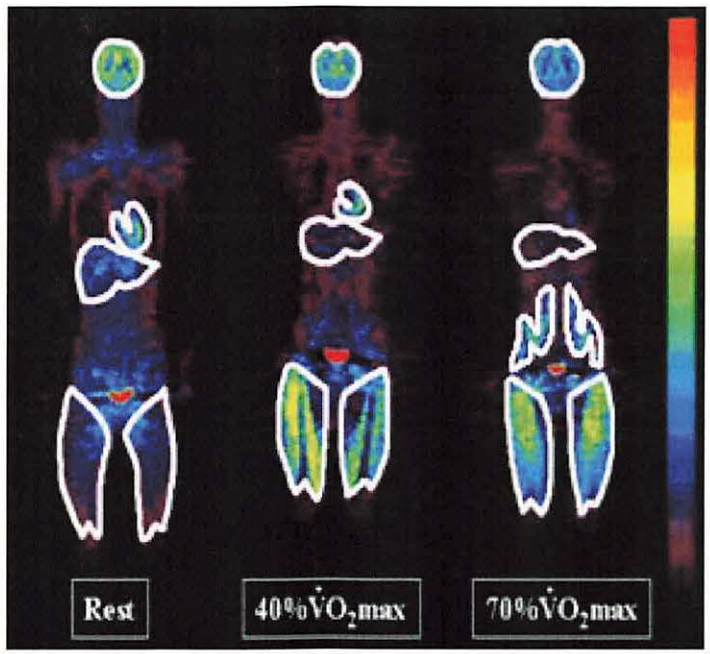

Figure 1. ROIs procedure and [^{18}F]FDG uptake of individual organs at rest (left) and exercise loads ; 40% and 70% VO_{2max} (right).

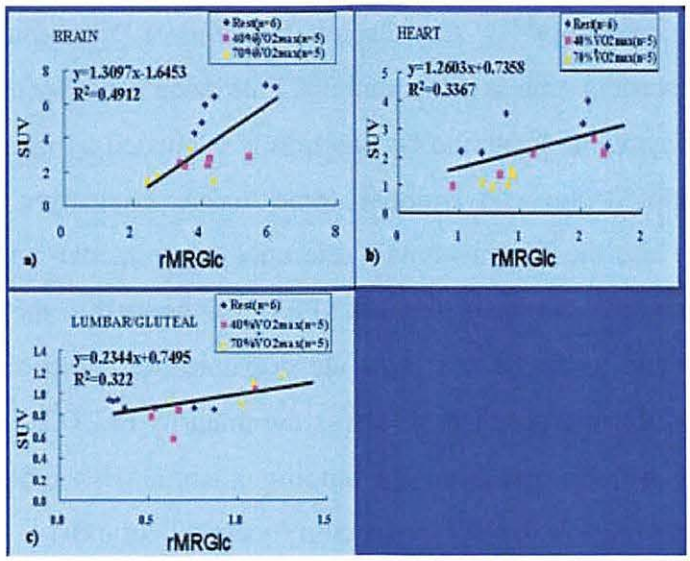

Figure 2. Correlation between SUV and rMRGlc in the viscera (a, b) and skeletal muscle (c), showing good correlation in the brain (a) and heart (b), and non-suggestive correlation in the lumbar/gluteal muscle (c).

VIII. 8. Imaging Quantification of Dopamine D_2 Function Using Positron Emission Tomography: a Methodological Approach

Mehedi M., Miyake M., Watanuki S., Itoh M., and Tashiro M.

Divisoin of Nuclear medicine, Cyclotron and Radioisotope Center, Tohoku University,

Background

PET with certain radioligands, is a sophisticated imaging technique that measures the *in vivo* receptor function in the brain. Dopamine D_2 neuroreceptor is synthesized from an amino acid, tyrosine in the presynaptic terminal, and stored in a vesicle. This neurotransmitter is released after depolarization in certain tasks. Dopamine (DA) function is the characteristic of synthesis, storage, release, reuptake and interactions with receptors. The radioligand ^{11}C-YM-09251-2 (Nemonapride) has been used as a tracer in this investigation. However, the distribution and kinetics of receptor-ligand interaction in the *in vivo* brain are quantified by certain kinetic assumptions. Dopamine is correlated with human behavior and personality[1,2]. Any discrete locations of D_2 receptors in the brain can cause neurological disorders such as schizophrenia, Parkinson's disease etc.

Assay of post-synaptic dopamine D_2 function is evaluated by measuring kinetic rate constants. We adopted the conventional three tissue compartment model method (predicted as 2TCM) and the Lammerstma's reference tissue model method (RTM) (3) to evaluate D_2 function. ^{11}C-Nemonapride (YM)-PET was applied to the normal volunteers and Parkinson's patients to assess post-synaptic dopamine D_2 function from the ligand-receptor association. Our purpose was to assess the integrity of 2TCM and RTM methods for the tracer, nemonapride by measuring the binding potential (BP) and tracer delivery (R_0) of cortical gray matters relative to reference region (occipital cortex).

Materials & methods

Two groups of human volunteers were assigned to this investigation. 7 male normal subjects, aged 47.4 ± 25.7 y (mean ± S.D.), were studied as resting control. They had no

previous history of dementia. In another, 5 Parkinson's patients (male/female; 2/3), aged 58 ± 10.2 y (mean ± S.D.), were assigned to the disease group. The study protocol was approved by the Human Ethics Review Committee of Tohoku University. The volunteers were requested abstaining from eating and/or drinking for at least 3 hours before experiment. They were free from mental anxieties and tensions. The radioligand, ^{11}C-YM 09151-2 (Nemonapride) with radioactivity dose of 251 ± 150 MBq (mean±S.D.) and 267 ± 57 MBq (mean ± S.D.) were administered to each group subjects, respectively. A dynamic 3D PET scan consisting transmission followed by emission scan, was started to cover the whole brain 5 min after the injection of radiotracer using the scanners, SET-2400W; Shimadzu Co. Japan and/or PT931-04 ECAT CTI, Knoxville, U.S.A. The transmission scan for tissue attenuation correction lasted 10 min for 1 scan, whether the emission scan continued 90 min performing 23 scans (i.e, 1 min/6 scan, 3 min/8 scan, 5 min/6 scan, and 10 min/3 scan). Arterial blood samplings were taken after tracer injection for 23 times (1 ml/18 times, and 3 ml/5 times for plasma metabolites) until dynamic emission scan was finished. The plasma radioactivity was measured, and the plasma metabolite for ^{11}C-Nemonapride (YM) tracer was measured by the high performance liquid chromatography analysis (HPLC).

In the control group, ROIs were drawn manually on the target structures including corpus striatum, frontal and temporal cortices and occipital cortex as reference region (Fig. 1). The ROIs data of the occipital cortex was used for the reference region in the reference tissue model (RTM) analysis. The kinetic parameters (K_1, k_2, k_3, and k_4) of target structures, and the tracer delivery (R_0) in the target region relative to the occipital region, were assessed by kinetic least square minimization analysis in the 2TCM and RTM methods. Binding potential (BP) of receptor-radioligand interactions, were also evaluated by applying conventional 2TCM and RTM methods. The tracer uptake ratio between target and reference regions was calculated.

On the other hand, the statistical parametric mapping analysis (SPM-99), was applied on R_0 images to test the significance in the difference of BPs between normal subjects and Parkinson's patients. The SPM analysis was performed to define the parameters of anatomical normalization.

Results

In the control group, BP and R_0 values of striatum, and cortical regions (frontal and temporal) were calculated by 2 different methods. For the striatum, the calculated BP,

measured by the RTM method, were significantly less than by the 2TCM, and the relative tracer delivery (R_0) was almost same for both methods. The BP values of frontal and temporal cortices were lower than those of the striatum (Fig. 2). In another, BP in the striatum was almost similar between normal volunteers and Parkinson's patients, whether it was reduced in the cortices of the patients' group (Fig. 2). The average tracer delivery of the normal volunteers and Parkinson's patients were almost similar (Fig. 2). The volume rendered brain images, developed by the statistical parametric mapping analysis (SPM-99), suggested the significantly reduced BP in the cortices of the Parkinson's disease patients (Fig. 3).

Discussions & conclusion

Cortical imaging was the choice to explore the feasibility of RTM method. Our investigation showed the robust cortical BP changes rather than subcortical structures in the parametric images of Parkinson's brain data. RTM method may be appropriate to assess the ligand-receptor interaction of cortices. It can be argued the rapid clearance of nemonapride from the reference region to the receptor rich cortices. Previous investigators found this criteria for another tracer where cerebellum was used as a reference region (4). We compared different data analysis strategies of post-synaptic dopamine D_2 receptor function of living human brain from the ligand-receptor interactions. We also adopted two different kinetic analytical approaches as to determine its integrity. ^{11}C-Nemonapride was used to assess the post-synaptic DA function. 2 tissue compartment model (2TCM) and reference tissue model (RTM) methods were applied on the normal volunteers and Parkinson's patients data to evaluate post-synaptic D_2 function. Reference tissue model (RTM) may be applied for our ligand, ^{11}C-Nemonapride. RTM is attractive for ^{11}C-Nomenapride kinetic analysis, because both binding potential and tracer-delivery are evaluated by pixel-basis. It is argued that RTM method is more reliable than 2TCM for the tracer, ^{11}C-Nemonapride (YM). The cortical changes of BP measured by RTM method, may be a target for future analysis of neurodegenerative diseases such as Parkinson's and schizophrenia. To assess DA function without taking any input function, would have the advent for RTM method. It is to be said that further investigations are needed to evaluate the feasibility and integrity of this imaging analysis using ^{11}C-Nemonapride (YM).

References

1) Farde L., Gusavsson J.P., Jonsson E., Nature **385** (1997) 590.
2) Alan B., Lisa K., Caleb A., et al., Am. J. Psychiatry **155** (1998) 1440.
3) Lammertsma A.A., Hume P.S., Neuroimage **4** (1996) 153.
4) Gunn R.N., Sargent P.A., Bench C.J., et al., Neuroimage **8** (1998) 426.

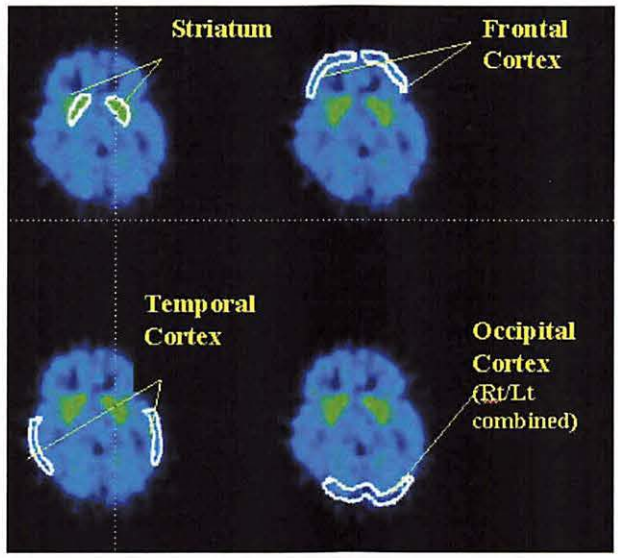

Figure 1. Procedure of ROIs analysis on the target (striatum, frontal and temporal cortices) and reference regions (occipital cortices).

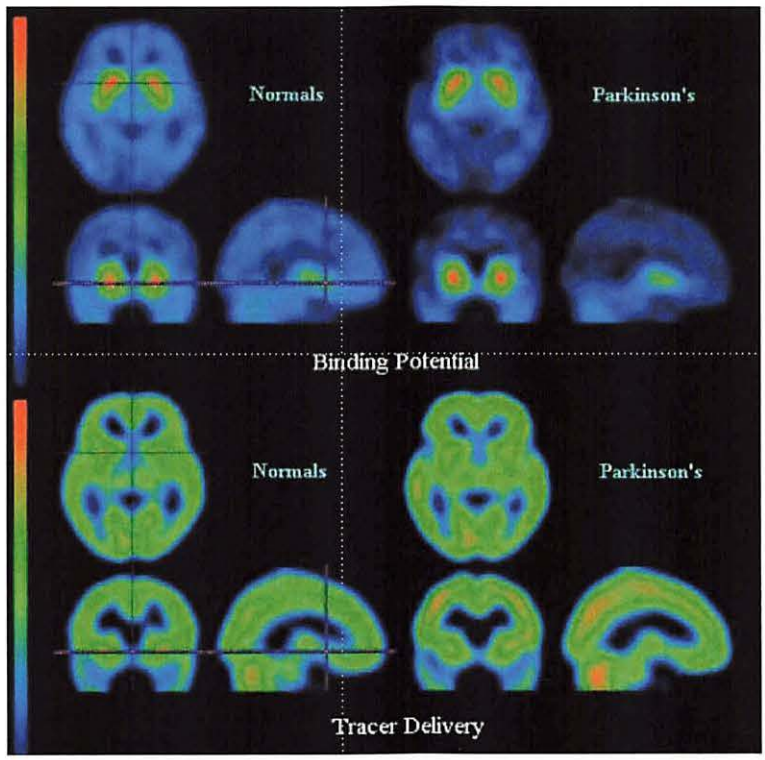

Figure. 2. Kinetic images of BP and R_0 showing the binding potential and tracer delivery of dopamine D_2. The images are shown from the normal volunteers and Parkinson's patients.

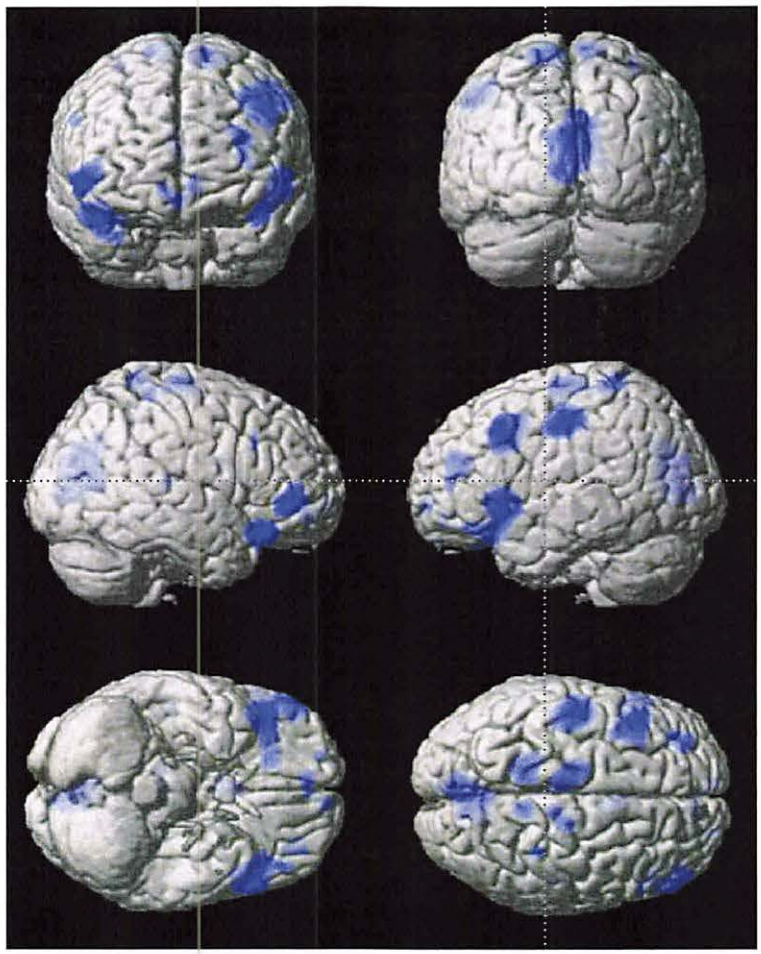

Figure 3. Volume rendered images analyzed by the statistical parametric mapping (SPM-99) showing the D_2 binding potential of ^{11}C-nemonapride (YM) between normal volunteers and Parkinson's patients. The D_2 binding potential reduction in the Parkinson's patients are visualized.

VIII. 9. Static Progression of Pediatric Malignant Brain Tumors with Metastases

Sakata H., Kanamori M., Tashiro M., Saito R., Nagamatsu K., Yamashita Y., Sonoda Y., Kumabe T., and Tominaga T.

Department of Neurosurgery, Tohoku University Graduate School of Medicine

Introduction

Metastasis and dissemination are the major causes of tumor related deaths. It is reported that both non-proliferating tumor cells and non-angiogenic micrometastases can remain dormant and occult for months or years, called dormancy in metastasis[1,2]. However, once these dormant micrometastases turn to macrometastases and show progressive growth, they shortly become lethal. There are few reports that clinically apparent macrometastases can remain static for a long period in pediatric malignant brain tumors.

In this article, we report three cases of pediatric malignant brain tumors which have macrometastases. In all cases, these metastatic lesions remain static for a long period after the initial treatments. We also attempt to use ^{11}C-methionine-positron emission tomography (MET-PET) to elucidate the metabolic activities in these clinically static metastatic lesions.

Case descriptions

Case 1

A 1-year-old boy was admitted to our department with an enlarged head circumference in August 1998. Magnetic resonance (MR) images demonstrated a mass lesion in the cerebellar vermis (Fig. 1a). The lesion was completely removed via a cerebellomedullary fissure approach, and the tumor was histologically diagnosed as desmoplastic medulloblastoma. Postoperatively, he received three cycles of combination chemotherapy using cisplatin and etoposide (PE chemotherapy). Although he had showed no neurological deterioration, T1-weighted MR imaging with gadolinium-diethylenetriaminepenta-acetic acid (Gd-DTPA), obtained in February 1999, revealed

multiple enhanced lesions in the bilateral cerebellar hemisphere, vermis, bilateral cerebral hemisphere, and spinal cord at the level of Th1 (Fig. 1b). These lesions were diagnosed as disseminated recurrence, and he received six additional cycles of PE chemotherapy. MR imaging in October 1999 demonstrated the new disseminated lesions in the medulla oblongata, left temporal lobe, left cerebellar hemisphere, and spinal cord at the level of C2 and C5, although other disseminated lesions showed no remarkable changes. He received irradiation consisting of 24 Gy to the whole brain and spinal cord, and 30 Gy to the posterior fossa, followed by four courses of chemotherapy using ifosfamide, cisplatin, and etoposide (ICE chemotherapy). Serial MR imaging had showed no obvious changes in the enhanced lesions for six years. However, MET-PET in June 2007 indicated that the enhanced lesion in the cerebellar vermis had elevated uptake of ^{11}C-methionine in which the maximum standardized uptake value (SUV_{max}) was 3.0 (Fig. 2a). MR imaging obtained in August 2007 demonstrated slight enlargement of the lesions. His current modified Rankin scare score is 5 after he received seven cycles of temozolomide chemotherapy.

Case 2

A 4-year old boy was admitted to our department presenting with headache. T1-weighted MR images with Gd-DTPA of the brain and spinal cord demonstrated a heterogeneously enhanced mass lesion in the cerebellar vermis (Fig. 1c) and nonenhanced intramedullary hypointensity lesion from C5 to Th1. The lesion in the cerebellar vermis was completely removed via a cerebellomedullary fissure approach, and the tumor was histologically diagnosed as medulloblastoma. Postoperatively, he received three courses of PE chemotherapy followed by irradiation consisting of 24 Gy to the whole brain and spinal cord, and 30 Gy to the posterior fossa. Three more courses of PE chemotherapy were given subsequently. The tumor in the cervical spinal cord slowly expanded during the four years. Serial MET-PET indicated progressive elevated uptake in the spinal cord lesion, in which the mean of SUV (SUV_{mean}) was 1.62 in July 2003 (Fig. 2b), and SUV_{mean} was 2.16 and SUV_{max} was 3.29 in December 2003 (Fig. 2c). In addition, MR imaging showed progressive spinal cord swelling (Fig. 1d). From these findings, open biopsy of the cervical spinal lesion was performed. Histopathological examination of the surgical specimen revealed disseminated medulloblastoma. He received ICE chemotherapy, but MR imaging demonstrated progressive disease. He died of tumor dissemination in June 2005.

Case 3

A 3-year-old boy was admitted to our department presenting with a respiratory disorder in June 2002. T1-weighted MR images with Gd-DTPA demonstrated a heterogeneously enhanced mass lesion in the fourth ventricle and the cisterna magna (Fig. 1e). The lesion was completely removed, and the tumor was histologically diagnosed as choroid plexus carcinoma. Postoperatively, he received irradiation consisting of 24 Gy to the whole brain and spinal cord, and 26 Gy to the posterior fossa. The patient had no sign of recurrence during the three years. MR imaging, however, demonstrated that newly disseminated enhanced lesion in the posterior wall of the third ventricle in August 2005 and in the fourth ventricle and right lateral ventricle in April 2006 (Fig. 1f), respectively. He received ICE chemotherapy from June 2006 to September 2006. MET-PET in March 2007 indicated elevated uptake in the fourth ventricle lesion in which SUV_{max} was 1.5 (Fig. 2d). These disseminated lesions gradually expanded the last two years, and he is currently receiving gamma-knife surgery for the recurrent tumors.

Discussion

Despite impressive improvements in therapy of medulloblastoma, the median survival time following tumor recurrence is 1.8 years[3]. The prognosis of choroid plexus carcinoma with metastases is also grave[4]. Considering the dismal prognosis of the patients with malignant brain tumors associated with metastases, recurrent tumors described in this article exhibited surprisingly static courses. In case 1, disseminated lesions showed almost no changes for six years without any additional treatments. In case 2, spinal intramedullary metastasis at initial diagnosis showed extremely slow progression for four years. However, it suddenly demonstrated rapid progression afterward and resulted in death. In case 3, disseminated lesions emerged three years after the initial treatments, and slowly expanded during the two years. There are few reports that clinically apparent metastases and disseminations can remain static for a long period in pediatric malignant brain tumors.

The role of MET-PET is recently well-established in the estimation of malignancy of glioma and differential diagnosis between radiation induced necrosis and tumor recurrence[5,6]. The mechanism of accumulation of MET in tissues are thought to present disruption of blood brain barrier, abundant vessels, and active carrier-mediated transport across the cell membrane[7]. Therefore, its accumulation is thought to increase protein

synthesis by neoplastic tissue proliferation, and a significant uptake in MET-PET is considered to reflect the existent of viable tumor cells. Sonoda et al. reported that the ratio of tumor tissue to contralateral gray matter on MET-PET of recurrent glioma was significantly higher than that of radiation necrosis[8]. Tsuyuguchi et al. also reported that MET-PET was useful in differentiating recurrent metastatic brain tumor from radiation necrosis[9]. Considering the advantage of MET-PET in visualizing the metabolism of the tumor, we attempted to use MET-PET in the present three cases to elucidate the metabolic activities in the clinically static metastatic lesions.

Although metastatic and disseminated lesions in the present three cases remained stable for a long period, MET-PET studies revealed increased uptake of these lesions. Therefore, they were thought to be metabolically active and still have proliferative potential despite their static behaviors. This fact raises the possibility that metastatses and disseminations in a static course may suddenly show lethal progression. Indeed, the recurrent tumor of the spinal cord in case 2 expanding very slowly for four years showed striking growth and became lethal after MET-PET revealed increased uptake[6]. This case indicates that MET-PET may be useful in the prediction of the drastic progression of the clinically static metastases. Careful follow-up of MET-PET is needed even if the recurrent tumor shows a static course.

References

1) Naumov G.N., Akslen L.A., Folkman J., Cell Cycle **5** (2006) 1779.
2) Naumov G.N., Bender E., Zurakowski D., Kang S.Y., Sampson D., Flynn E., Watnick R.S., Straume O., Akslen L.A., Folkman J., Almog N., J. Natl. Cancer Inst. **98** (2006) 316.
3) Bowers D.C., Gargan L., Weprin B.E., Mulne A.F., Elterman R.D., Munoz L., Giller C.A., Winick N.J., J. Neurosurg. **107** (2007) 5.
4) Gopal P., Parker J.R., Debski R., Parker J.C Jr., Arch. Pathol. Lab. Med. **132** (2008) 1350.
5) Jacobs A.H., Dittmar C., Winkeler A., Garlip G., Heiss W.D., Mol. Imag. **1** (2002) 309.
6) Inoue T., Kumabe T., Takahashi T., Nakajima T., Watanabe M., Tominaga T., Childs Nerv. Syst. **23** (2007) 113.
7) Kubota K., Matsuzawa T., Fujiwara T., Abe Y., Hatazawa J., Kawabe H., Miyazawa H., Sato T., Ido T., Ishiwata K., Kaku Igaku **22** (1985) 1327.
8) Sonoda Y., Kumabe T., Takahashi T., Shirane R., Yoshimoto T., Neurol. Med. Chir. (Tokyo). **38** (1998) 342.
9) Tsuyuguchi N., Sunada I., Iwai Y., Yamanaka K., Tanaka K., Takami T., Otsuka Y., Sakamoto S., Ohata K., Goto T., Hara M., J. Neurosurg. **98** (2003) 1056.

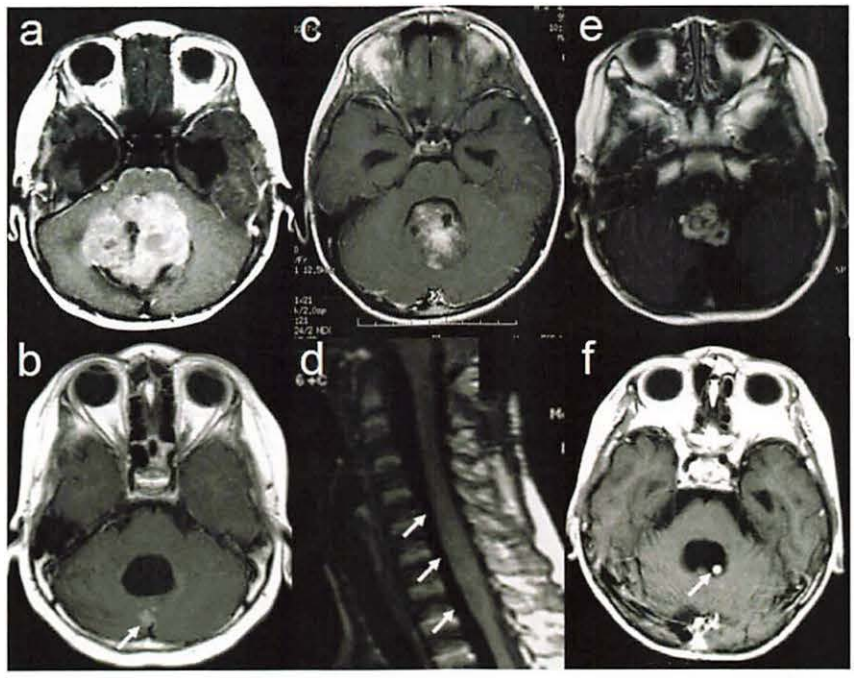

Figure 1. (Case 1) a, Preoperative T1-weighed magnetic resonance (MR) imaging with gadolinium-diethylenetriaminepenta-acetic acid (Gd-DTPA) demonstrating a mass lesion in the cerebellar vermis. b, Follow-up MR imaging, obtained in February 1999, revealing a enhanced recurrent tumor in the cerebellar vermis (arrow). (Case 2) c, Preoperative T1-weighed MR imaging with Gd-DTPA showing a mass lesion in the cerebellar vermis. d, T1-weighted MR imaging with Gd-DTPA of the spine demonstrating spinal cord swelling from C5 toTh1 in July 2003 (arrow). (Case 3) e, Preoprative T1-weighted MR imaging with Gd-DTPA revealing a heterogeneously enhanced mass lesion in the fourth ventricle and the cisterna magna. f, Follow-up MR imaging, obtained in April 2006, showing a enhanced recurrent tumor in the fourth ventricle (arrow).

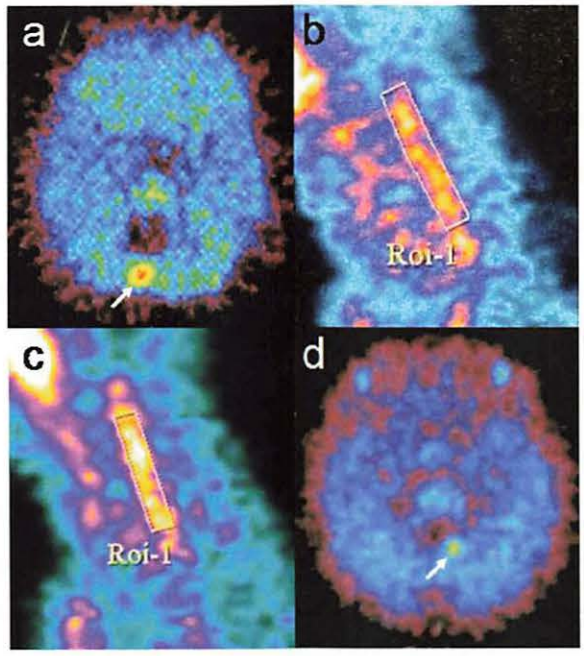

Figure 2. (Case 1) a, ^{11}C-methionine-positron emission tomography (MET-PET) in June 2007 indicating that the enhanced lesion in the cerebellar vermis has elevated uptake of ^{11}C-methionine (arrow). (Case 2) b, c, Serial MET-PET indicating progressive elevated uptake in the spinal cord lesion. (Case 3) d, MET-PET in March 2007 indicating elevated uptake in the fourth ventricle lesion (arrow).

VIII. 10. Increased Brain Histamine H_1 Receptor Binding in Patients with Anorexia Nervosa

Yoshizawa M.[1,2], Tashiro M.[3], Fukudo S.[1,4], Yanai K.[5], Utsumi A.[1], Kano M.[1,4], Karahasi M.[1], Endo Y.[1], Morisita J.[1], Sato Y.[1], Adachi M.[1], Itoh M.[3], and Hongo M.[1,6]

[1]*Department of Psychosomatic Medicine, Tohoku University School of Medicine*
[2]*SS30 Health Care Center*
[3]*Cyclotron and Radioisotope Center, Tohoku University*
[4]*Department of Behavioral Medicine, Tohoku University School of Medicine*
[5]*Department of Pharmacology, Tohoku University School of Medicine*
[6]*Department of Comprehensive Medicine, Tohoku University School of Medicine*

Introduction

Anorexia nervosa (AN) is a behavioral disorder characterized by fear of becoming obese, refusal to maintain a minimally normal body weight, disturbance of body image, and denial of the seriousness of the current low body weight[1]. AN occurs mainly in adolescent or young adult females[1]. AN patients start a self-imposed diet with chronic starvation featuring continuous strengthening symptoms and AN signs. The cause and progression of AN may involve biological vulnerability with dysfunction in the central neuron system being one of the most important causation factors.

The central histaminergic neuron system modulates various physiological functions such as wakefulness, sleep-awake cycle, fluid balance, body temperature, cardiovascular control, appetite control, stress-related hormone release, learning, memory, aggressive behavior, and emotion[2]. Central histaminergic activity is increased by food intake after starvation[3]. Also, dehydration has been reported to increase the synthesis and release of histamine in the hypothalamus[4]. Moreover, H_1R concentration has been shown to be inversely correlated with food intake, particularly low protein diets[5]. In addition, the central histaminergic neuron system is affected by various stressors[6-9]. These findings suggest the alteration of central histaminergic activity in AN patients. However, there has been no report on AN.

We tested the following hypotheses in this study: females have higher H_1R density in the limbic system than males, and the density of central H_1R is increased in AN patients.

Methods and materials

Twelve female AN patients (BMI=14.1±1.7), 11 healthy age-matched male volunteers (BMI=20.4±1.3), and 12 healthy age-matched female volunteers (BMI=20.3±1.1) were enrolled in this study. All subjects gave a written informed consent.

Doxepin, a tricyclic antidepressant, was C-11 labeled and used as a PET tracer. The injected dose and cold mass of [^{11}C]doxepin were 117.0 ± 23.0 MBq (3.16 ± 0.62 mCi) and 1.86 ± 1.64 nmol, respectively.

The scanner collected 63 simultaneous transverse slices with a spatial resolution of 4 mm (transaxial) and 4.5 mm (axial) full-width at half-maximum in the center of the field of view. The sensitivity for a 20-cm cylindrical phantom was 48.6 kcps $kBq^{-1}mL^{-1}$ (1.8 Mcps $\mu Ci^{-1}mL^{-1}$) in the three-dimensional mode[10]. Dynamic PET images were obtained for 90 min (22 sequential scans; 6 scans×90s, 7 scans×180s, 6 scans x 300s and 3 scans×600s) after [^{11}C]doxepin injection.

PET dynamic images, after being corrected for tissue attenuation, were reconstructed using a filtered back projection algorithm. The reconstructed PET images were co-registered to the identical stereotaxic brain coordinate system using its own MRI-T1 image as a reference. Regions of interest (ROIs) were first placed on the cerebellum. Information from the ROIs was automatically copied onto the co-registered PET images to obtain time activity curves (TACs). Cerebellar TAC was used as input function to calculate parametric brain images of the binding potential (BP) of [^{11}C]doxepin based on the graphical analysis method introduced by Logan and colleagues[11]. The applicability of this method to a human study with [^{11}C]doxepin has been confirmed[12]. Finally, brain BP images were created.

Results (Figs. 1-a, 1-b)

BP of [^{11}C]doxepin in control females was significantly higher than that in control males in the left (L)-Medial prefrontal cortex, right (R)-Orbitofrontal cortex, L-Orbitofrontal cortex, R-Temporal cortex, R-Amygdala, L-Amygdala, R-Hippocampas, and L-Hippocampas. On the other hand, there was no area where BP of [^{11}C]doxepin was significantly lower in control females than in males.

BP of [^{11}C]doxepin in AN patients was significantly higher than that in control females in L-Lentiform nucleus, and R-Amygdala. On the other hand, there was no area

where BP of [^{11}C]doxepin was significantly lower in AN patients than in control females .

Discussion

The first point that can be drawn from our results is that the histaminergic neuron system in the human brain is different between males and females. In support of this finding, a human CSF study has shown that females have higher levels of histamine metabolites than males[13]. In addition, animal studies have also shown sex differences in the central histaminergic neuron system. These differences include H_1R densities (male<female)[14], suppressive effect of histidine on food intake (male<female)[15], stress related hypothalamic histamine release[16] in rat. These findings suggest that central histaminergic activity is higher in females than in males in both animals and humans. Thus, females may adapt better to starvation through the central histaminergic neuron system than males. The risk of developing AN may be increased by not only the social background that women want to be thin because people tend to admire a thin figure, but also biological vulnerability associated with central histaminergic activity.

The second point is that AN patients showed significantly higher BP of [^{11}C]doxepin in the amygdala and lentiform nucleus than healthy females. In our previous study, chronic food-deprivation-induced stress in rats, which can be an AN model, reduces central H_1R density[9]. In addition, a human PET study in patients with depressive disorder, which is one of the representative stress-related disorders, has shown lower BP of [^{11}C]doxepin in several brain areas in these patients than in healthy controls[17]. The decreased H_1R density and BP of [^{11}C]doxepin in these studies have been explained by the sustained release of endogenous histamine and the down-regulation of H_1R as a consequence of endogenous ligands. However, the present results show the opposite. If the increased BP of [^{11}C]doxepin in the amygdala is the cause of AN, females with higher H_1R in the amygdala may be more susceptible to AN. The increased BP of [^{11}C]doxepin in the amygdala of AN patients may also be a result of AN. Central histaminergic activity is increased by food intake after starvation (3) and H_1R concentration is increased by feeding low-protein diets (5). Starvation and feeding in AN patients may facilitate the increase in H_1R concentration in the amygdala.

BP of [^{11}C]doxepin in the orbitofrontal cortex, amygdala and hippocampus was higher in females and AN patients than in males. These brain areas may play important roles in the central modulation of eating behavior because they are parts of the limbic

system controlling emotion, cognition, and decision making[18]. These are very interesting results associated with the characteristics observed in AN patients, such as distorted cognition and emotional changes to food and body image. Therefore, the central histaminergic neuron system may play a role in AN, not only through stimulation of the satiety center, but also through activation of advanced psychological systems.

In conclusion, the present study demonstrates that females have higher BP of [^{11}C]doxepin in the limbic system than males, and that AN patients have higher BP of [^{11}C]doxepin in the amygdala and lentiform nucleus than normal females. These findings suggest that the central histaminergic neuron system may play an important role in the pathophysiology of AN.

References

1) American Psychiatric Association: Diagnostic and Statistical Manual for Mental Disorders, Fourth Edition, Text Revision. Washington, DC: American Psychiatric Press (2000).
2) Brown RE., Stevens D.R., Hass H.L., Prog. Neurobiol. **63** (2001) 637.
3) Itoh Y., Oishi R., Saeki K., Neurosci. Lett. **125** (1991) 235.
4) Kjaer A., Larsen P.J., Knigge U., et al., Endocrinology **136** (1995) 2189.
5) Haq A.U., Bundrant H.M., Mercer L.P., J. Nutr. **126** (1996) 3083.
6) Taylor K.M., Snyder S.H., Science **172** (1971) 1037.
7) Yoshitomi I., Itoh Y., Oishi R., et al., Brain Res. **362** (1986) 195.
8) Ito C., Shen H., Toyota H., et al., Neurosci. Lett. **262** (1999) 143.
9) Endou M., Yanai K., Sakurai E., et al., Brain Res. **891** (2001) 32.
10) Fujiwara T., Watanuki S., Yamamoto S., et al., Ann. Nucl. Med. **11** (1997) 307.
11) Logan J., Fowler J.S., Volkow N.D., et al., J. Cereb. Blood Flow Metab. **16** (1996) 834.
12) Suzuki A., Tashiro M., Kimura Y., et al., Ann. Nucl. Med. **19** (2005) 425.
13) Prell G.D., Khandelwal J.K., Burns R.S., et al., Arch. Gerontol .Geriatr. **12** (1991) 1.
14) Ghi P., Orsetti M., Gamalero S.R., et al., Pharmacol. Biochem. Behav. **64** (1999) 761.
15) Kasaoka S., Kawahara Y., Inoue S., et al., Nutrition **21** (2005) 855.
16) Ferretti C., Blengio M., Ghi P., et al., Pharmacol. Biochem. Behav. **59** (1998) 255.
17) Kano M., Fukudo S., Tashiro A., et al., Eur. J. Neuroscience **20** (2004) 803.
18) Bechara A., Damasio H., Damasio A.R., Cereb. Cortex **10** (2000) 295.

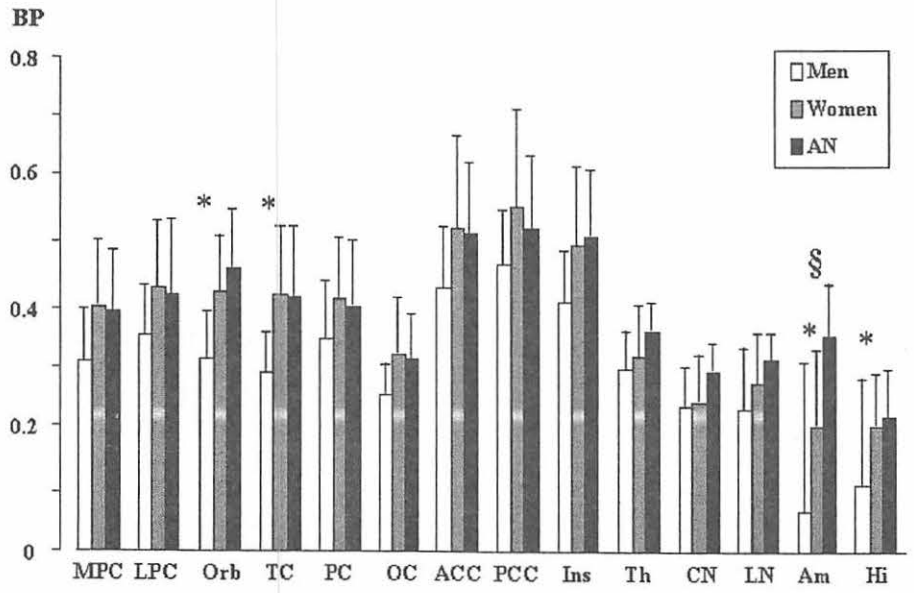

Figure 1 (a) ROI-based comparisons of BP of [^{11}C]doxepin in the right cerebral hemisphere MPC, medial prefrontal cortex; LPC, lateral prefrontal cortex; Orb, orbitofrontal cortex; TC, temporal cortex; PC, parietal cortex; OC, occipital cortex; ACC, anterior cingulate cortex; PCC, posterior cingulate cortex; Ins, insula; Th, thalamus; CN, caudate nucleus; LN, lentiform nucleus; Am, amygdala; Hi, hippocampus.
* Men vs. Women ($p<0.05$), § Women vs. AN ($p<0.05$).

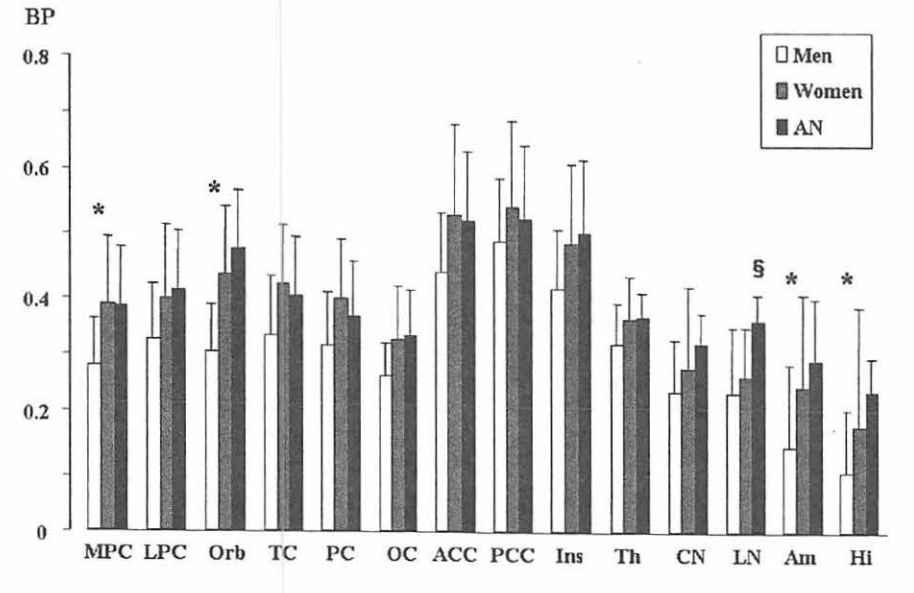

Figure 1. (b) ROI-based comparisons of BP of [^{11}C]doxepin in the left cerebral hemisphere.

VIII. 11. Decreased Binding of [^{11}C]Donepezil as Shown by PET Correlated with the Clinical Effect of Donepezil Administration in Alzheimer's Disease: The Osaki-Tajiri Project

Kasuya M.[1], Ishikawa H.[1], Okamura N.[2], Kato M.[2], Sasaki Y.[2], Nakata E.[1], Ishikawa Y.[3], Funaki Y.[3], Tanaka N.[1], Iwata R.[3], Yanai K.[2], and Meguro K.[1]

[1]*Departments of Geriatric Behavioral Neurology, Tohoku University*
[2]*Department of Pharmacology, Tohoku University*
[3]*Cyclotron and Radioisotope Center, Tohoku University*

Introduction

Alzheimer's disease (AD) is the most common form of dementia in the elderly, characterized by degeneration of basal forebrain cholinergic neurons innervating the cortex, amygdale, and hippocampus[1,2]. Reduced choline acetyltransferase (ChAT) activity, one of the markers of cholinergic deficits in AD, is correlated with severity of senile plaques[3]. ChAT activity is also associated with profound cognitive impairments, such as loss of memory, learning and attention in AD[3,4]. Relationship between cholinergic deficits and cognitive function is now directly shown by neuroimaging studies using positron emission tomography (PET)[5,6].

Several compounds such as (S)-[^{11}C]methyl nicotine (^{11}C-nicotine)[7], N-[^{11}C]methyl-4-piperidyl acetate (^{11}C-MP4A)[8], N-[^{11}C]methyl-piperidin-4-yl propionate(PMP) (^{11}C-PMP)[9], [5-^{11}C-methoxy]donepezil (^{11}C-donepezil)[10] were developed as PET ligands for visualizing the central cholinergic activity, and applied in clinical studies on AD. ^{11}C-Nicotine is only an indicator of nicotinic receptors. Because ^{11}C-MP4A and ^{11}C-PMP are substrate of acetylcholine esterase (AChE) and rapidly converted to the hydrolyzed product especially in regions of high AChE activity, their concentrations strongly depend on flow. On the other hand, ^{11}C-donepezil can be an indicator of total cholinergic terminals, and is a relatively stable radiotracer. The metabolite of ^{11}C-donepezil counted for only 5% of the total radioactivity present in the brain at 60 min after injection of ^{11}C-donepezil[11]. Our previous study using this ligand[10] showed that AD patients exhibited reduction of donepezil binding in the brain even in the early stage, and that longitudinal evaluation by ^{11}C-

donepezil enabled determination of AChE binding occupancy of oral administered donepezil.

There is abundant evidence that the basal forebrain cholinergic system plays a major role in cognitive function, especially in the domain of attention. Cholinergic fibers from the nucleus basalis of Meynert (nbM) to the cerebral cortex are associated with visual attention while fibers to the hippocampi are involved in working memory[12]. Stimulation of cholinergic pathways by nicotine enhances cognition, especially attention both in healthy adults[13] and AD patients[14]. A previous study on AD treated with donepezil showed that visual selective attention tasks could be sensitive markers to detect treatment response[15]. Kadir et al. revealed that ^{11}C-nicotine binding in the right frontal lobe and bilateral parietal lobe significantly associated with attention in AD patients[6]. Bohnen et al. showed that temporal AChE activity measured by ^{11}C-PMP was significantly correlated with attention in AD[16]. While agreement of these PET studies reported AChE activity was correlated with attention, there remains a controversy in the brain regions. We investigated relationship between regional ^{11}C-donepezil binding and cognitive functions including attention in mild to moderate AD patients. We here present a representative case with PET data of ^{11}C-donepezil that was responded by donepezil treatment.

Methods

Subjects : Subjects in this study were AD Patients who diagnosed by NINCDS-ADRDA criteria[17]. The patients who already were administered donepezil were excluded at initial visit the Osaki-Tajiri clinic.

PET : After bolus injection of 134~378 MBq of [^{11}C]donepezil, a dynamic 3D scan was performed for 60 min. Arterialized venous blood samples were obtained from a medial cubital vein for assessing blood RI activity.

Analyses: Regions of interest (ROIs) were drawn on striatum, thalamus, frontal, temporal, parietal, occipital, anterior and posterior cingulate, and hippocampus. The ratio of the concentration in tissue to that in plasma at equilibrium was calculated as distribution volume (DV) by Logan's graphical analysis. We also used average value of regional DVs as a representing value of donepezil binding in whole brain.

Clinical effects: In this study, we used Mini-Mental State Examination (MMSE) as global cognitive function[18], Clinical Global Impression scale (CGI) (3 grades evaluation: 0 pint ~2 point) as clinician's impression, Digit Symbol (DigSm) from WAIS-R as psychomotor speed[19], Trail Making Test A (TMTA) as executive function, the subcategories of Cognitive Abilities Screening Instruments (CASI) as cognitive domains[20,21].

Procedures: The subjects received first PET and above the neuropsychological tests before orally, then the subjects orally took donepezil (5 mg/day) for 6 months. After that, they examine the second PET and the same neuropsychological tests as the 6 months ago.

Results

The result was shown in Table 1 and Table 2. The DV which shows binding the donepezil in the brain decreased 200.1 from the first PET to the second PET. The DV were declined the range from 122.2 to 245.8 between the first PET and the second PET in each ROIs (Table 1). There was no change in MMSE score (Table 2). The neuropsychological tests were improved 2 point in DigSm, 5 second in TMTA, and 2 point in Abstraction and Judgement. Some tests decline the scores, 2 point in Remote Memory, 2 point in Manipulation and Concentration, 1 point in List-generating fluency. The impression of medical doctor improved 1point in CGI.

Comment

In this study, TMTA and DigSm were improved, so it supports the results of Kadir et al[6]. Kadir et al. used the nicotin-tracer, however, we used the donepezil-tracer. Although one subject case report, we directly indicated the effect of donepezil, especially about attention.

References

1) Coyle J.T., Price D.L., DeLong M.R., Science **219** (1983) 1184.
2) Aubert I., Araujo D.M., Cecyre D., Robitaille Y., Gauthier S., J. Neurochem. **58** (1992) 529.
3) Perry E.K., Tomlinson B.E., Blessed G., Bergmann K., Gibson P.H., Perry R.H., Br. Med. J. **2** (1978) 1457.
4) Everitt B.J., Robbins T.W., Ann. Rev. Psychol. **48** (1997) 649.
5) Shinotoh H., Namba H., Fukushi K., Nagatsuka S., Tanaka N., Aotsuka A., Ota T., Tanada S., Irie T., Ann. Neurol. **48** (2000) 194.
6) Kadir A., Almkvist O., Wall A., Långström B., Nordberg A., Psychopharmacology **188** (2006) 509.
7) Nordberg A., Hartvig P., Lilja A., Viitanen M., Amberla K., Lundqvist H., Andersson Y., Ulin J., Winblad B., Långström B., J. Neural Transm. Park. Dis. Dement. Sect. **2** (1990) 215.
8) Iyo M., Namba H., Fukushi K., Shinotoh H., Nagatsuka S., Suhara T., Sudo Y., Suzuki K., Irie T.,

Lancet **349** (1997) 1805.
9) Bohnen N.I., Kaufer D.I., Hendrickson R., Ivanco L.S., Lopresti B.J., Koeppe R.A., Meltzer C.C., Constantine G., Davis J.G., Mathis C.A., Dekosky S.T., Moore R.Y., J. Neurol. Neurosurg. Psychiatry **76** (2005) 315.
10) Okamura N., Funaki Y., Tashiro M., Kato M., Ishikawa Y., Maruyama M., Ishikawa H., Meguro K., Iwata R., Yanai K., Br. J. Clin. Pharmacol. **65** (2008) 472.
11) De Vos F., Santens P., Vermeirsch H., Dewolf I., Dumont F., Slegers G., Dierckx R.A., De Reuck J., Nucl. Med. Biol. **27** (2000) 745.
12) Everitt B.J., Robbins T.W., Central cholinergic systems and cognition. Ann. Rev. Psychol. **48** (1997) 649-84.
13) Warburton D.M., Prog. Neuropsychopharmacol. Biol. Psychiatry **16** (1992) 181.
14) Newhouse P.A., Sunderland T., Tariot P.N., Blumhardt C.L., Weingartner H., Mellow A., Murphy D.L., Psychopharmacology (Berl). **95** (1988) 171.
15) Foldi N.S., White R.E., Schaefer L.A., Int. J. Geriatr. Psychiatry **20** (2005) 485.
16) Bohnen N.I., Kaufer D.I., Hendrickson R., Ivanco L.S., Lopresti B., Davis J.G., Constantine G., Mathis C.A., Moore R.Y., DeKosky S.T., Neurosci. Lett. **380** (2005) 127.
17) McKhann G., Drachman D., Folstein M., Katzman R., Price D., Stadlan E.M., Neurology **34** (1984) 939.
18) Folstein M.F., Folstein S.E., McHugh P.R., J. Psychiatr. Res. **12** (1975) 189.
19) Wechsler D., Wechsler Adult Intelligence Scale Manual. New York, Elsevier (1981).
20) Teng E.L., Hasegawa K., Homma A., Imai Y., Larson E., Graves A., Sugimoto K., Yamaguchi T., Sasaki H., Chiu D., et al., Int. Psychogeriatr. **6** (1994) 45.
21) Guy W., Clinical Global Impression. ECDEU Assessment Manual for Psychopharmacology, revised National Institute of Mental Health, Rockville, MD. (1976).

Table 1. Distribution volume on first PET and second PET.

	First PET	Second PET
Striatum	17.5	12.1
Thalamus	16.5	9.8
Frontal lobe	14.0	8.7
Temporal lobe	14.2	9.7
Parietal lobe	14.7	8.8
Occipital lobe	14.1	7.9
Anterior cingulate	13.6	8.3
Posterior cingulate	14.2	9.4
Hippocampus	13.0	9.7
Average of DV	14.7	9.3

Table 2. Neuropsychological tests score on the first PET and second PET.

	First PET	Second PET
MMSE	15	15
DigSm	23	25
TMTA (sec)	150	145
CASI		
C1 remote memory	10	8
C2 recent memory	4	5
C3 attention	2	6
C4 manipulation and concentration	6	4
C5 orientation	13	13
C6 visual construction	10	10
C7 abstraction and fluency	3	5
C8 list-generating fluency	4	3
C9 language abilities	9	9

MMSE = Mini Mental State Examination
TMTA = Trail making test A
CASI = Cognitive abilities Screening Insturument
C1~ C9 = Cognitive domains of CASI

IX. RADIATION PROTECTION AND TRAINING OF SAFETY HANDLING

IX. 1. Beginners Training for Safe Handling of Radiation and Radioisotopes in Tohoku University

Baba M., Yamazaki H., Miyata T., and Iwata R.

Cyclotron and Radioisotope Center, Tohoku University

During 2007, the beginners training for safe handling of radiation and radioisotopes in Tohoku University was conducted in three courses as usual:

1) Radiation and Isotopes, 2) X-ray Machines and Electron Microscope, and 3) Synchrotron Radiation (SOR). The training was held twice a year, May and November, under the help for lectures and practice from various departments and research institutes of the university.

Lectures in English which were started in November of 2002 were continued for students and/or researchers who are not so familiar with Japanese language, by using PC projector and text of copies of view graphs (English class). The membership of the English class is almost constant as shown later.

The training for "Radiation and Radioisotopes" is for persons who use unshielded radioisotopes and accelerators, and has been conducted from 1977. The contents of lectures and practices are shown in Table 1. The order and content of the lecture was slightly modified from 2005 aiming at better understanding by trainees: the lecture on "the effect of radiation on human" was moved to the second to give stronger motivation for the training course and the following lectures. Along with the change, a new introductory lecture of "Introduction to radiation" was newly prepared as the first lecture to provide knowledge required to understand the lecture of "the effect of radiation on human". In the fiscal year of 2007, the training was performed for 499 persons (17 persons in the English class). The departments or institutes to which they belong are given in Table 2.

The training for "X-ray machines and electron microscopes" started at the end of 1983. The training is scheduled twice a year at the same time as that for "Radiation and Radioisotopes". In this course, only lectures are given with no practice. The contents of

the lectures and the distributions of trainees are shown in Table 3 and Table 4, respectively. The number of trainees was 395 (37 in the English class).

The training for the "Synchrotron Radiation" began at the end of 1995. The contents of the lectures are the same as those of the radiation and radioisotopes but no practice. In 2007, the number of trainees of the SOR course was 94 (11 in the English class).

Table 1. Contents of the lectures and practices for safe handling of radiation and radioisotopes in 2007.

Lectures (one day)	Hours
Introduction to radiation	0.5
Effects of radiation on human	1.0
Radiation physics and measurements	1.0
Chemistry of radioisotopes	1.0
Radiological protection ordinance including video	1.5
Safe handling of radioisotopes	1.5

Practices (one day)	Hours
Treatment of unsealed radioactive solution	4.0
Measurement of surface contamination and decontamination	1.0
Measurement of gamma-rays and beta-rays	2.0

Table 2. Distribution of trainees for "Radiation and Radioisotopes" in 2007.

Department	Staff	Student	Total	English class
CYRIC	1	6	7	0
Medicine	11	61	72	3
Dentistry	2	22	24	0
Pharmacy	0	45	45	1
Science	3	66	69	2
Engineering	5	87	92	3
Agriculture	1	63	64	0
Research Institutes	19	99	118	8
The others	4	4	8	0
Total	46	453	499	17

Table 3. Contents of the lectures for "X-ray machines and Electron microscopes" in 2007.
(same for both Japanese and English class)

Lectures (one day)	Hours
Safe handling of X-ray machines	1.5
Radiological protection ordinance	0.5
Video for safe handling of radiation and radioisotopes	0.5

Table 4. Distribution of trainees for "X-ray machines and Electron microscopes" in 2007.

Department	Staff	Student	Total	English class
Medicine	1	2	3	0
Dentistry	1	0	1	0
Pharmacy	1	13	14	0
Science	2	22	24	3
Engineering	15	164	179	15
Research Institutes	28	141	169	19
The others	0	5	5	0
Total	48	347	394	37

Table 5. Distribution of trainees for "Synchrotron radiation" in 2007.

Department	Staff	Student	Total	English Class
Science	0	5	5	0
Engineering	7	22	29	4
Research Institutes	14	46	60	7
Total	21	73	94	11

IX. 2. Radiation Protection and Management

Miyata T.[1], Yuki H.[1], Yamazaki H.[1], Baba M.[1], and Nakae H.[2]

[1]Cyclotron and Radioisotope Center, Tohoku University
[2]Japan Radiation Protection Co., Ltd.

(1) Overview

During the fiscal year of 2007, research and education in the center were conducted as active as usual.

In May 2007, we received the inspection by "Monbu-kagakusho" (the Ministry of Education and Culture, Sports, Science and Technology), and the application for increase of maximum amount of 124I for use in CYRIC was accepted.

The measurement of radioactivity concentration which was started along with the reorganization of national university in 2004 is continued periodically but the observed level was low enough generally. Devices and gas counters with automatic sample changer for radioactivity concentration measurement (samplers, a.ß automatic counters) were routinely used without serious problems by several radiation facilities in Tohoku University.

(2) Unsealed radio nuclides used in CYRIC

The species and amounts of unsealed radio nuclides handled in CYRIC during the fiscal year of 2007 are summarized in Table 1. The table includes the isotopes produced by the cyclotron as well as those purchased from the Japan Radio Isotope Association or taken over from other radioisotope institutes.

(3) Radiation exposure dose of individual worker

The exposure doses of the workers in CYRIC during 2007 are given in Table 2. The doses were sufficiently lower than the legal dose limits.

(4) Radiation monitoring of the workplace

Radiation dose rates inside and outside of the controlled areas in CYRIC were monitored periodically and occasionally when needed. They were generally below the legal dose limits although there are several "hot spots" in mSv/hr range like slits or beam stopper of the 930 cyclotron and so on. Surface contamination levels of the floors inside the controlled areas were also measured with a smear method and a survey meter method. They were under the legal regulation levels.

(5) Wastes management

The radioactive wastes were delivered to the Japan Radio Isotope Association twice in the fiscal year of 2007.

The concentration of radioisotopes in the air released from the stack after filtration was monitored with stack gas monitors. The values of concentration were well below the legal regulation levels. The radioactive water was stocked in the tanks at least for 3 days and then released to the sewerage after confirming that the concentration was lower than the legal regulation levels.

Radioactive organic scintillator waste was treated periodically by incinerator provided by Fuji-kogyo Co.Ltd. The incinerator was overhauled last year.

Table 1. Unsealed radioisotopes used in each building of CYRIC during the fiscal year of 2007.

(a) Cyclotron Building (kBq)

Group 2		Group 3		Group4	
^{95m}Tc	1,758.700	^{11}C	428,178,800.000	^{18}F	734,848,120.000
Total	1,758.700	Total	428,178,800.000	Total	734,848,120.000

(b) Radio-isotope Building (kBq)

Group 2		Group 3		Group4	
^{68}Ge	235,323.300	^{11}C	3,478,000.000	^{3}H	47,689.450
^{125}I	116,887.091	^{32}P	1,037,145.076	^{14}C	740.000
^{22}Na	52,594.000	^{99m}Tc	3,260,166.643	^{18}F	57,202,000.000
		^{124}I	2,237,714.370		
Total	455,872.901	Total	10,015,279.829	Total	57,250,429.450

(c) Research Building (kBq)

Group1,2		Group 3		Group 4	
		^{15}O	9,065,000.000	^{18}F	3,256,000.000
Total	0	Total	9,065,000.000	Total	3,256,000.000

Table 2. Occupational radiation exposures at CYRIC during the fiscal year of 2007.

Dose range (mSv)	Number of individuals
No measurable exposure	39
0.0 - 1.0	11
1.0 - 2.0	2
2.0 - 3.0	1
3.0 -	0
Total number of persons monitored	53

X. PUBLICATIONS

X. PUBLICATIONS

[696] Deceiving Others: Distinct Neural Responses of the Prefrontal Cortex and Amygdala in Simple Fabrication and Deception with Social Interactions.
Nobuhito Abe, Maki Suzuki, Etsuro Mori, Masatoshi Itoh, Toshikatsu Fujii.
J. Cognitive Neurosci., **19** (2007) 287-295.

[697] The physiological and pathophysiological roles of neuronal histamine: An insight from human positron emission tomography studies.
Kazuhiko Yanai, Manabu Tashiro.
Pharmacology & Therapeutics, **113** (2007) 1-15.

[698] Reactivation of medial temporal lobe and occipital lobe during the retrieval of color information: A positron emission tomography study.
Aya Ueno, Nobuhito Abe, Maki Suzuki, Kazumi Hirayama, Etsuro Mori, Manabu Tashiro, Masatoshi Itoh, Toshikatsu Fujii.
NeuroImage, **34** (2007) 1292-1298.

[699] Evaluation of the binding characteristics of [^{18}F]fluoroproxyfan in the rat brain for in vivo visualization of histamine H_3 receptor.
Yoshihito Funaki, Kimihiko Sato, Motohisa Kato, Yoichi Ishikawa, Ren Iwata, Kazuhiko Yanai.
Nucl. Med. Biol., **34** (2007) 981-987.

[700] First achievement of less than 1 mm FWHM resolution in practical semiconductor animal PET scanner.
K. Ishii, Y. Kikuchi, S. Matsuyama, Y. Kanai, K. Kotani, T. Itoh, H. Yamazaki, Y. Funaki, R. Iwata, M. Itoh, K. Yanai, J. Hatazawa, N. Itoh, N. Tanizaki, D. Amano, M. Yamada, T. Yamaguchi.
Nucl. Instr. Meth. Phys. Res., **A 576** (2007) 435-440.

[701] In vivo visualization of donepezil binding in the brain of patients with Alzheimer's disease.
Nobuyuki Okamura, Yoshihito Funaki, Manabu Tashiro, Motohisa Kato, Yoichi Ishikawa, Masahiro Maruyama, Hiroyasu Ishikawa, Kenichi Meguro, Ren Iwata, Kazuhiko Yanai.
Brit. J. Clin. Pharmacol., **26** (2007) 1-8.

[702] Binding and safety profile of novel benzoxazole derivative for in vivo imaging of amyloid deposits in Alzheimer's disease.
Nobuyuki Okamura, Shozo Furumoto, Yoshihito Funaki, Takahiro Suemoto, Motohisa Kato, Yoichi Ishikawa, Satoshi Ito, Hiroyasu Akatsu, Takayuki Yamamoto, Tohru Sawada, Hiroyuki Arai, Yukitsuka Kudo, Kazuhiko Yanai.
Geriatr. Gerontol. Int., **7** (2007) 393-400.

[703] Initial evaluation of dynamic human imaging using ^{18}F-FRP-170 as a new PET tracer for imaging hypoxia.
Tomohiro Kaneta, Yoshihiro Takai, Ren Iwata, Takashi Hakamatsuza, Hiroyasu Yasuda, Katsutoshi Nakayama, Yoichi Ishikawa, Shoichi Watanuki, Shozo Furumoto, Yoshihito Funaki, Eiko Nakata, Keiichi Jingu, Michiko Tsujitani, Masatoshi Ito, Hiroshi Fukuda, Shoki Takahashi, Shogo Yamada.
Ann. Nucl. Med., **21** (2007) 101-107.

[704] 2-(2-[2-Dimethylaminothiazol-5-yl]ethenyl)-6-(2-[fluoro]ethoxy)benzoxazole: a novel PET agent for in vivo detection of dense amyloid plaques in Alzheimer's disease patients.
Yukitsukasa Kudo, Nobuyuki Okamura, Shozo Furumoto, Manabu Tashiro, Katsutoshi Furukawa, Masahiro Maruyama, Masatoshi Itoh, Ren Iwata, Kazuhiko Yanai, Hiroyuki Arai.
J. Nucl. Med., **48** (2007) 553-561.

[705] Neural correlates of perceptual difference between itching and pain: A human fMRI study.
Mochizuki H., Sadato N., Saito D.N., Toyoda H., Tashiro M., Okamura N., Yanai K.
Neuroimage, **36** (2007) 706-717.

[706] Autonomic Nervous Function and Localization of Cerebral Activity during Lavender Aromatic Immersion.
Duan X., Tashiro M., Yambe T., Wang Q., Sasaki T., Kumagai K., Luo Y., Nitta S., Itoh M.
Technol. Health Care, **15** (2007) 69-78.

[707] Brain activity associated with the dual task management differ depending on the combinations of response modalities.
Mochizuki H., Tashiro M., Gyoba J., Suzuki M., Okamura N., Itoh M., Yanai K.
Brain Res., **1172** (2007) 82-92.

[708] 3D-imaging using micro-PIXE.
K. Ishii, S. Matsuyama, Y. Watanabe, Y. Kawamura, T. Yamaguchi, R. Oyama, G. Momose, A. Ishizaki, H. Yamazaki and Y. Kikuchi.
Nucl. Instrum. Meth. Phys. Res., A**571** (2007) 64-68.

[709] Progress and application of the Tohoku microbeam system.
S. Matsuyama, K. Ishii, H. Yamazaki, Y. Kikuchi, K. Inomata, Y. Watanabe, A. Ishizaki, R. Oyama, Y. Kawamura, T. Yamaguchi, G.Momose, M.Nagakura, M.Takahashi, T.Kamiya
Nucl. Instrum. Meth. Phys. Res., B**260** (2007) 55-64.

[710] Development of microbeam scanning system.
R.Oyama, S.Matsuyama, K.Ishii, H.Yamazaki, Y.Kikuchi, K.Inomata, Y.Watanabe, A.Ishizaki, Y.Kawamura, T.Yamaguchi, G..Momose.
Int. J. PIXE, **17** (2007) 23-31.

[711] Improvement of radiosensitive liquid-core microcapsules by yttrium polymerization.
S. Harada, S. Ehara, K. Ishii, H. Yamazaki, S. Matsuyama, T. Kamiya, T. Sakai, K. Arakawa, T. Sato, S. Oikawa.

Int. J. PIXE, **17** (2007) 33-40.

[**712**] *In-vivo* elemental analysis by PIXE-_-CT.
Y. Kawamura, K. Ishii, H. Yamazaki, S. Matsuyama, K. Kikuchi, T. Yamaguchi, Y. Watanabe, R. Oyama, G. Momose, A. Ishizaki, S. Tsuboi, K. Yamanaka, M. Watanabe
Int. J. PIXE, **17** (2007) 41-46.

[**713**] Analysis of lacquerware using in-air submilli-PIXE camera.
S. Matsuyama, K. Ishii, H. Yamazaki, Y. Kikuchi, R. Oyama, Y. Kawamura, A. Ishizaki, G.. Momose, A. Fujisawa and K. Kyono
Int. J. PIXE, **17** (2007) 77-84.

[**714**] Status report of Sasaki Taro memorial PIXE Center.
A. Terakawa, T. Sasaki, K. Ishii, Y. Kawamura, K. Sera, and H. Sasaki.
Proc. XI Int. Conf. PIXE and its Anal.l Appl., Puebla, Mexico, (May 25-29, 2007) PII-3-1~4.

[**715**] Precise measurement of first Townsend coefficient, using parallel plate avalanche chamber.
Mohammad Nakhostin, Mamoru Baba, Toshiro Itoga , Takuji Oishi, Tsutomu Ohtsuki.
Nucl. Instrum. Meth. Phys. Res., A**572** (2007) 999-1003.

[**716**] Experimental determination of deuteron-induced activation cross sections of yttrium.
M.S.Uddin, M. Baba , M.Hagiwara , F.Tarkanyi and F.Ditroi.
Radioch. Acta, **95** (2007) 187-192.

[**717**] Comment on "On spectrometric properties of transmission avalanche counters at moderate specific ionization".
Mohammad Nakhostin, Mamoru Baba.
Nucl. Instrum. Meth. Phys. Res., A**578** (2007) 453-454.

[**718**] Influence of Neutron Source Spectrum and Thermal Neutron Scattering Law Data on MCNPX Simulation of a Cyclotron-based Boron Neutron Capture Therapy.
Shunsuke Yonai, Mamoru Baba, Toshiro Itoga, Takashi Nakamura, Hitoshi Ypkobori, Yoshihisa Tahara
J. Nucl. Sci. Technol., **44** (2007) 1361-2007.

[**719**] Development of the RF-IGISOL at CYRIC.
Tetsu Sonoda, Masahiro Fujita, Akiyoshi Yamazaki, Takuya Endo, Tsutomu Shinozuka, Yuji Miyashita, Nozomi Sato, Atsushi Goto, Eiji Tanaka, Tomokazu Suzuki, et al.
Nucl. Instrum. Meth. Phys. Res., B**245** (2007) 295.

[**720**] Target preparation by the precipitation method for nuclear reactions.
K. Takamiya, T. Ohtsuki, H. Yuki, T. Mitsugashira, N. Sato, T. Suzuki, M. Fujita, T. Shinozuka, Y. Kasamatsu, H. Kinunaga, A. Shinohara, S.Shibata, T. Nakanishi.
Appl.Radiat. Isot., **65** (2007) 32-35.

[**721**] Hyperfine anomalies of Sc isotopes.
S. Ohya, T. Otsubo, T. Izumikawa, K. Nishimura, S. Muto, T. Shinozuka.
Hyperfine Interaction, **180** (2007) 55-60.

[722] High-Spin States in ^{93}Nb.
Yasuo Wakabayashi, Tomonori Fukuchi, Yasuyuki Gono, Atsuko, Odahara, Shuichi Tanaka, Masaki Inoue, Takafumi Sasaki, Michiya Kibe, Naho Hokoiwa, Tsutomu Shinozuka, Masahiro Fujita, Akiyoshi Yamazaki, Tetsu Sonoda, Chun Sik Lee, Young Kwan Kwon, Jun Young Moon, Ju Hahn Lee.
J. Phys. Soc. Jpn., **76** (2007) 114202

XI. MEMBERS OF COMMITTEE

XI. MEMBERS OF COMMITTEE (as of Jan. 1, 2008)

General

(Chairperson)	Keizo	Ishii	(Graduate School of Engineering)
	Makoto	Watanabe	(Executive Vice President)
	Kazushige	Maeda	(Graduate School of Science)
	Kazuaki	Iwasa	(Graduate School of Science)
	Tetsuya	Ono	(Graduate School of Medicine)
	Keiichi	Sasaki	(Graduate School of Dentistry)
	Norimichi	Nakahata	(Graduate School of Pharmaceutical Sciences)
	Akira	Hasegawa	(Graduate School of Engineering)
	Minoru	Sato	(Graduate School of Agricultural Science)
	Kazuhiko	Sogawa	(Graduate School of Life Science)
	Atuki	Terakawa	(Graduate School of Biomedical Engineering)
	Isamu	Sato	(Institute for Materials Research)
	Hiroshi	Fukuda	(Institute for Development, Aging and Cancer)
	Tanetoshi	Koyama	(Institute of Multidisciplinary Research for Advanced Materials)
	Syoki	Takahashi	(University Hospital)
	Jirohta	Kasagi	(Laboratory of Nuclear Science)
	Mamoru	Baba	(CYRIC)
	Ren	Iwata	(CYRIC)
	Hiromichi	Yamazaki	(CYRIC)
	Yasuhiro	Sakemi	(CYRIC)
	Etusyu	Kuraoka	(CYRIC)
	Tsutomu	Shinozuka	(CYRIC)
	Manabu	Tashiro	(CYRIC)
	Hirokazu	Tamura	(Graduate School of Science)

	Kazuhiko	Yanai	(Graduate School of Medicine)
	Tetsuya	Ono	(Radiation Safety Committee, Research Promotion Council)
(Observer)	Seiko	Sato	(Head of Administration Office, Graduate School of Information Science)

Cyclotron

(Chairperson)	Yasuhiro	Sakemi	(CYRIC)
	Toshio	Kobayashi	(Graduate School of Science)
	Hideya	Onodera	(Graduate School of Science)
	Hirokazu	Tamura	(Graduate School of Science)
	Kazushige	Maeda	(Graduate School of Science)
	Yasushi	Kino	(Graduate School of Science)
	Keizo	Ishii	(Graduate School of Engineering)
	Akira	Hasegawa	(Graduate School of Engineering)
	Atuki	Terakawa	(Graduate School of Engineering)
	Isamu	Sato	(Institute for Materials Research)
	Anpo	Sai	(Institute of Multidisciplinary Research for Advanced Materials)
	Tsutomu	Otsuki	(Laboratory of Nuclear Science)
	Ren	Iwata	(CYRIC)
	Hiromichi	Yamazaki	(CYRIC)
	Etusyu	Kuraoka	(CYRIC)
	Tsutomu	Shinozuka	(CYRIC)
	Manabu	Tashito	(CYRIC)

Radiation Protection and Training of Safe Handling

(Chairperson)	Hiromichi	Yamazaki	(CYRIC)
	Kazuaki	Iwasa	(Graduate School of Science)
	Yoshihiko	Uehara	(Graduate School of Medicine)
	Tetuya	Terasaki	(Graduate School of Pharmaceutical Sciences)
	Keizo	Ishii	(Graduate School of Engineering)

	Michio	Komai	(Graduate School of Agricultural Science)
	Kazuhiro	Sogawa	(Graduate School of Life Science)
	Tatuo	Shikama	(Institute for Materials Research)
	Katuyoshi	Hori	(Institute for Development, Aging and Cancer)
	Tomohiro	Kaneta	(University Hospital)
	Ren	Iwata	(CYRIC)
	Tsutomu	Shinozuka	(CYRIC)
	Etusyu	Kuraoka	(CYRIC)

Life Science

(Chairperson)	Ren	Iwata	(CYRIC)
	Noriaki	Ohuchi	(Graduate School of Medicine)
	Shogo	Yamada	(Graduate School of Medicine)
	Syoki	Takahashi	(Graduate School of Medicine)
	Teiji	Tominaga	(Graduate School of Medicine)
	Masahiko	Yamamoto	(Graduate School of Medicine)
	Yukitsuka	Kudo	(Biomedical Engineering Research Organization)
	Keiichi	Sasaki	(Graduate School of Dentistry)
	Masayuki	Seki	(Graduate School of Pharmaceutical Sciences)
	Keizo	Ishii	(Graduate School of Engineering)
	Kazuhiko	Nishitani	(Graduate School of Life Science)
	Hiroshi	Fukuda	(Institute for Development, Aging and Cancer)
	Nariyasu	Mano	(University Hospital)
	Yoshihiro	Takai	(Graduate School of Medicine)
	Hiromichi	Yamazaki	(CYRIC)
	Manabu	Tashiro	(CYRIC)
	Yoshihito	Funaki	(CYRIC)

Prevention of Radiation Hazards

(Chairperson)	Hiromichi	Yamazaki	(CYRIC)
	Naohito	Iwasa	(Graduate School of Science)
	Yasushi	Kino	(Graduate School of Science)
	Keizo	Ishii	(Graduate School of Engineering)
	Ren	Iwata	(CYRIC)
	Yasuhiro	Sakemi	(CYRIC)
	Tsutomu	Shinozuka	(CYRIC)
	Etusyu	Kuraoka	(CYRIC)
	Manabu	Tashiro	(CYRIC)
	Takamoto	Miyata	(CYRIC)
	Tomoya	Yonezawa	(CYRIC)

Research Program

(Chairperosn)	Hiromichi	Yanazaki	(CYRIC)
	Osamu	Hashimoto	(CYRIC)
	Toshio	Kobayashi	(Graduate School of Science)
	Hirokazu	Tamura	(Graduate School of Science)
	Kazushige	Maeda	(Graduate School of Science)
	Kazuhiko	Yanai	(Graduate School of Medicine)
	Akira	Takahashi	(Graduate School of Medicine)
	Akira	Hasegawa	(Graduate School of Engineering)
	Atuki	Terakawa	(Graduate School of Engineering)
	Isamu	Sato	(Institute for Materials Research)
	Hiroshi	Fukuda	(Institute for Development, Aging and Cancer)
	Syoki	Takahashi	(University Hospital)
	Jirohta	Kasagi	(Laboratory of Nuclear Science)
	Tsutomu	Otsuki	(Laboratory of Nuclear Science)
	Tsutomu	Sekine	(Center for the Advancement of Higher Education)

	Ren	Iwata	(CYRIC)
	Yasuhiro	Sakemi	(CYRIC)
	Etusyu	Kuraoka	(CYRIC)
	Tsutomu	Shinozuka	(CYRIC)
	Manabu	Tashiro	(CYRIC)
(Observer)	Masatoshi	Itoh	(CYRIC)
(Observer)	Takashi	Wakui	(CYRIC)

XII. STAFF

XII. STAFF (as of Jan. 1, 2008)

Director Keizo Ishii

Division of Accelerator

Osamu	Hashimoto[1)]
Tsutomu	Shinozuka
Takashi	Wakui
Kenji	Shimada
Shizuo	Chiba[7)]
Yasuaki	Ohmiya[7)]
Naoto	Takahashi[7)]
Shigenaga	Yokokawa[7)]

Division of Instrumentations

Sakemi	Yasuhiro
Hirokazu	Tanura[1)]
Hikonojo	Orihara[5)]
Hiroyuki	Okamura[5)]
Atuki	Terakawa[3)]
Masatoshi	Itoh
Sho-ichi	Watanuki
Hidetomo	Yoshida

Division of Radiopharmaceutical Chemistry

Ren	Iwata
Yukitsuka	Kudo[4)]
Yoshihito	Funaki
Yohichi	Ishikawa
Shozo	Furumoto[4)]

Division of Cyclotron Nuclear Medicine

Kazuhiko	Yanai[2)]
Masatoshi	Itoh[6)]
Keiichiro	Yamaguchi[5)]
Kohichiro	Kawashima[5)]
Manabu	Tashiro
Masayasu	Miyake
Maki	Suzuki
Mehedi	Masud
Kazuaki	Kumagai
Takehisa	Sasaki
Targino Rodrigues Dos Santos	
Takeshi	Ogura

Division of Radiation Protection and Safety Control

Mamoru	Baba
Hiromichi	Yamazaki
Etusyu	Kuraoka
Hideyuki	Yuki
Takashi	Nakamura[5)]
Takamoto	Miyata
Tomoyoshi	Yamazaki
Hirokazu	Nakae[8)]

Graduate Student and Researcher

Yu-ji	Miyashita	(Graduate School of Science)
Nozomi	Sato	(Graduate School of Science)
Naoya	Sugimoto	(Graduate School of Science)
Ryo	Matsuo	(Graduate School of Science)
Miki	Tateoka	(Graduate School of Science)
Tetuya	Nagano	(Graduate School of Science)
Sayo	Hoshino	(Graduate School of Science)
Yoshitaka	Aono	(Graduate School Pharmaceutical Sciences)
Eita	Sakai	(Graduate School Pharmaceutical Sciences)

Akihiro	Sugawara	(Graduate School, Division of Medicine)
Margaretha	Sulistyoningsih	(Graduate School, Division of Medicine)
Takuji	Ohishi	(Graduate School of Engineering)
Mohammad	Nakhostin	(Graduate School of Engineering)
Akram	Mohammadi	(Graduate School of Engineering)
Toshio	Okuchi	(Graduate School of Engineering)
Yoichi	Yamaguchi	(Graduate School of Engineering)
Yasunori	Horiuchi	(Graduate School of Engineering)

Office Staff

Seiko	Sato
Tomoya	Yonezawa
Yoshiaki	Kawamura
Yu-ko	Yamashita
Kyoko	Fujisawa
Fumiko	Mayama
Masakatsu	Itoh
Kietu	Takahashi
Kimiko	Abe
Asami	Sawada
Ai	Endo
Shurikeiko	Fujimoto

1) Graduate School of Science
2) Graduate School of Medicine
3) Graduate School of Engineering
4) TUBERO
5) Visiting Professor
6) Specially-approved visiting professor
7) SUMI-JU Accelerator Service Ltd.
8) Japan Radiation Protection Co., Ltd.